Viability of Determining Ion Charge and Velocity Utilizing a Single Silicon Timepix Detector

A Dissertation presented to

the Faculty of the Department of Physics

University of Houston

In partial fulfillment of the requirements for the degree

Doctor of Philosophy

By Nicholas Neal Stoffle

May 2014

Viability of Determining Ion Charge and Velocity Utilizing a Single Silicon Timepix Detector

Nicholas Neal Stoffle

Approved:

Prof. Lawrence Pinsky, Chairman

Prof. Kevin Bassler

Prof. Alex Ignatiev

Prof. Kwong Lau

Prof. Ricardo Vilalta

Dean, College of Natural Sciences and Mathematics

Acknowledgments

The completion of this dissertation would not have been possible without the support of my amazing wife April, and wonderful children Nate, Finn, Eli, and Isaac, whom I thank for their unwavering confidence and love. I also would like to thank my father, my mother, and my brother for their constant faith in me and my abilities.

My heartfelt thanks go to my advisor, Prof. Lawrence Pinsky, for his knowledge, guidance, and patience throughout this endeavor and to Prof. Alex Ignatiev, for his support and encouragement when it was most needed. And of course I would be remiss in failing to recognize the flexibility and support provided by the Space Radiation Analysis Group during the course of this effort.

This work is part of a larger effort to utilize the Timepix devices in the space environment, and several people have contributed substantially and were instrumental in making progress toward this goal. Dr. Martin Kroupa has provided expertise in hardware interface, detector setting optimization, and calibration of the Timepix units. Dr. Son Hoang built and implemented much of the pattern recognition framework needed to isolate and analyze pixel clusters within the data, including the algorithms used to identify incidence angles. Dr. John Idarraga has supplied his expertise in the Timepix hardware and provided support along this vein at CERN, and Dr. Ryan Rios has lent his extensive knowledge of ROOT and programming to the efforts herein.

In addition, there are many who have helped, guided, and prodded me along the way to whom I am sincerely grateful. To my friends and colleagues for their support and encouragement over these many years, to my teachers and

instructors throughout my academic career for the guidance and opportunities they have provided, and to everyone else that has been a part of my life during this extended bout of insanity:

Thank you all.

Dedicated to my father, Thomas Neal Stoffle.
He showed me the joy of learning,
the beauty of knowledge,
the satisfaction of creating,
and the power of being true to oneself.

Viability of Determining Ion Charge and Velocity Utilizing a Single Silicon Timepix Detector

An Abstract of a Dissertation presented to
the Faculty of the Department of Physics
University of Houston

In partial fulfillment of the requirements for the degree
Doctor of Philosophy

By Nicholas Neal Stoffle
May 2014

Abstract

The emergence of the Timepix technology, a class of hybrid pixel readout Application-Specific Integrated Circuits (ASIC), has provided an opportunity for the evolution of small, low-power, active radiation detectors which have unprecedented capability. The application of this technology to measurements in the space radiation environment and to radiation monitoring for manned spaceflight is an ongoing effort, and the space exploration application imposes the need to minimize the mass and power draw of the hardware. To those ends, an evaluation of the capability of a single Timepix detector to accomplish the identification of the incident radiation field in terms of ion charge and velocity is critical to providing a characterization of the radiation environment that is independent of dosimetric endpoint. The goal of this work is to present the progress made toward individual ion identification using a single silicon Timepix detector along with an evaluation of the proposed methods and algorithms used to achieve this aim.

Contents

List of Figures

List of Tables

Chapter 1

Ionizing Radiation In Space

1.1 Hazards of the Final Frontier

Astronaut crews routinely operate within a hostile environment where a minor coolant leak can lead to drowning and even a small flame poses an immediate danger to survival, but hazards such as these are readily perceived by the human senses. Ionizing radiation has no taste, no smell, and in low doses, is nearly undetectable within the bounds of human sensory perception, but it is one of the few hazards of space travel that causes long-term effects to human physiology. [1–3] In addition, beyond the geomagnetic shielding provided in Low Earth Orbit, phenomena such as energetic solar particle events become a serious threat to astronaut health and even to survival. [4, 5]

At larger doses, ionizing radiation can cause an array of short term, or acute, effects such as changes to blood chemistry, erythema, nausea, and in

extreme cases, organ failure and death. [1, 3, 4, 6] However, even at low doses, ionizing radiation affects organs and the component cells in ways that can have long term impacts. Damage to the cellular structure resulting from the ionization process as a particle transits through matter can lead to defects in cell function and cell reproduction, which have the potential to lead to cell mutation, which in turn can lead to an increased risk for cancer, degenerative tissue diseases such as latent cardiovascular or cataracts, and in the case of heavy ions, even central nervous system effects. [1, 6, 7]

1.2 Ionizing and Non-Ionizing Radiation

The spectrum of what is known collectively as radiation is quite vast and includes both electromagnetic waves and nuclear particles. Infrared radiation, visible light, and even radiant heat are all classified as a part of the electromagnetic spectrum. [8] Radiation detectors are designed using materials and technology chosen for their response to the component of the spectrum that is of interest. [9, 10]

Different portions of the radiation spectrum have noticeably different effects on matter. Radiation in the visible spectrum has little impact on cellular structure, while radiant heat in sufficient quantities can significantly disrupt the physical processes necessary for cells to remain viable. The definition of 'ionizing radiation' is those quanta of the radiation spectrum that have sufficient energy to remove electrons from their bound states within a material.

[6, 11, 12]

While ultraviolet wavelengths do not result in ionization, such wavelengths do cause cellular damage as a result of chemical dissociation of critical components of the cellular structure. In mammalian cells, this is thought to occur due to the efficiency in absorption of ultraviolet wavelengths by the cellular DNA. [13, 14]

Within this work, we focus on ionizing radiation, with the primary goal of identifying nuclear particles based on ion charge and ion velocity. Neutrons and other neutral particles, as well as the ionizing EM components, are included in the discussion since such particles have the ability to interact with matter via kinematic and electromagnetic processes and cause ionization. [15]

1.3 Ionizing Radiation in the Near Earth Environment

Over the last several decades, since humans first ventured into space, our understanding of the ionizing radiation environment near Earth and within the solar system has expanded, but this understanding is far from complete. Several models for the radiation spectra at Earth have been developed based on data gathered both from terrestrial measurements and from satellites in orbit around the planet. [16–18] [1]

[1] Portions of this chapter have been incorporated into a book chapter accepted for publication [19], and the relevant paragraphs have been marked here accordingly.

1. Ionizing Radiation In Space

The Earth's magnetic field and atmosphere provide a robust shield for terrestrial life from cosmic and solar radiation, though relatively small amounts of energy from these types of radiation do reach sea level. For example, neutron cascades which are produced through atmospheric interactions with space radiation, as well as muons resulting from the decay of atmospheric interaction products, are measurable along with a range of other particle types at ground level observation stations. As altitude increases, the amount of matter for particles to interact with decreases. Hence, the dose from ionizing radiation increases with altitude, and the background radiation dose at sea level is lower than the background measured at higher elevations. [20] [1]

The Earth's magnetic field can be thought of as a dipole field which is tilted and offset relative to the Earth's spin axis. Charged particles become trapped in the geomagnetic field within regions known as the Van Allen Belts. The offset and tilt of the geomagnetic field give rise a region known as the South Atlantic Anomaly, where the inner Van Allen Belt, containing primarily trapped protons, is nearest the surface of the earth. [21, 22] [1]

At Low Earth Orbit (LEO) altitudes, the radiation field has a distinct separation in components based on geographic location. Trapped electrons populate high latitude regions over North America and above the Indian Ocean, as well as in regions near the magnetic poles. These are regions where the trapped electrons can reach LEO altitudes as they bounce between north-south magnetic mirror points. These regions are also populated by those galactic cosmic rays with sufficient rigidity to penetrate the magnetic field. Closer to the

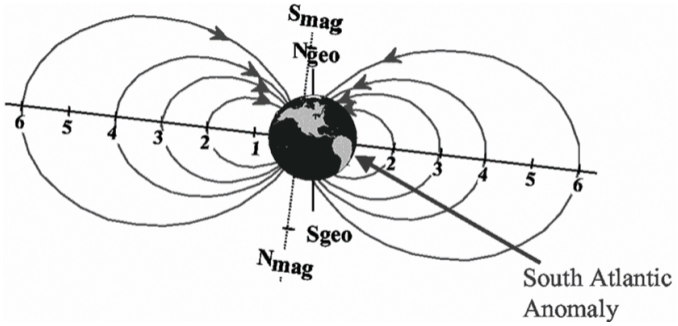

Figure 1.1: The approximation of the geomagnetic field as a dipole field is shown. [21] The magnetic axis is offset and tilted with respect to the Earth's spin axis, giving rise to a region known as the South Atlantic Anomaly (SAA).

planet's equator, the magnetic field is stronger at similar altitudes, resulting in only the higher energy cosmic rays being able to penetrate to LEO altitudes. In addition, geomagnetic cusp regions are regions at higher latitudes where geomagnetic field lines have been opened to the interplanetary magnetic field through interaction with the solar wind. These cusp regions allow access of solar particles to LEO altitudes. [23, 24] [1]

Solar phenomena, such as Coronal Mass Ejections, or CMEs, and solar particle events, also have an impact on radiation components in LEO. CMEs are shock fronts in the interplanetary medium composed of plasma swept up following a solar eruption. When such a shock passes the Earth, it can cause disturbances in the geomagnetic field which have the ability to cause variations in the radiation belt location and composition. The result is a widening of the areas of effect associated with the magnetic field, and in some cases, the formation of temporary belts of trapped particles. [21] [1]

Solar Particle Events, or SPEs, are also a concern at Low Earth Orbit. High energy protons and other solar products are accelerated toward Earth as a result of disturbances or eruptions in the sun's corona. [5,25] The high energy protons arrive at Earth within minutes to hours and can cause a dramatic increase in both the energy spectrum and in the overall proton flux. [26] If a vehicle is not well shielded by the geomagnetic field, SPEs can result in greatly increased radiation exposure relative to quiescent periods. [5, 27] [1]

Another source of ionizing radiation in the Near Earth Environment are the so called Anomalous Cosmic Rays, or ACR. These are heavy ions, predominantly protons, helium, nitrogen, oxygen, and neon, with carbon notably absent, which have been accelerated as a result of various solar phenomena. The ACR manifest as a flux enhancement in the lower energy portion of the GCR spectra for the associated ions. [28, 29]

Rounding out this short survey of ionizing radiation sources, Galactic Cosmic Rays, often referred to as GCR, comprise a fully ionized background in the space radiation field with a component that extends well into relativistic energies and a nuclear composition that ranges from electrons through iron and beyond. Thought to consist of supernova remnants and other interstellar media accelerated through various processes during propagation to our solar system, these relativistic, or very nearly so, ions are the most difficult portion of the space radiation field to shield against. [5, 30] [1]

While GCR are a relatively small portion of the particle flux in LEO, they present a large fraction of the biologically significant radiation exposure

to spacefarers. This, combined with the difficulty in shielding against GCR, presents a unique problem as humans transition into manned interplanetary exploration. [5, 31]

1.4 Ionizing Radiation Beyond Earth

Utilizing current propulsion technology, times on the order of Earth-months are required for astronauts to traverse the interplanetary space to Mars. During the interplanetary trip, spacecraft will leave the relative safety of the Earth's magnetic shield. [31]

Without the protection of the geomagnetic field, cosmic rays and solar particle events become more hazardous. Exposure to cosmic rays increase since there is no magnetic shielding to filter out the low to medium energy component of the GCR. Similarly, proton events pose a much greater threat in interplanetary space. For example, in LEO, the geomagnetic field provides protection over much of a vehicle's orbit such that nearly all radiation exposure from an SPE is eliminated, leaving only short time periods of exposure as the vehicle traverses high latitude regions where the geomagnetic field allows SPE particles access to LEO altitudes. Conversely, without the geomagnetic field, SPEs pose a continual elevated exposure over the entire event duration, which can last several Earth-days. [5]

Solar cycle also plays a role in the makeup of the space radiation environment. As solar activity increases over the sun's eleven year activity cycle, the

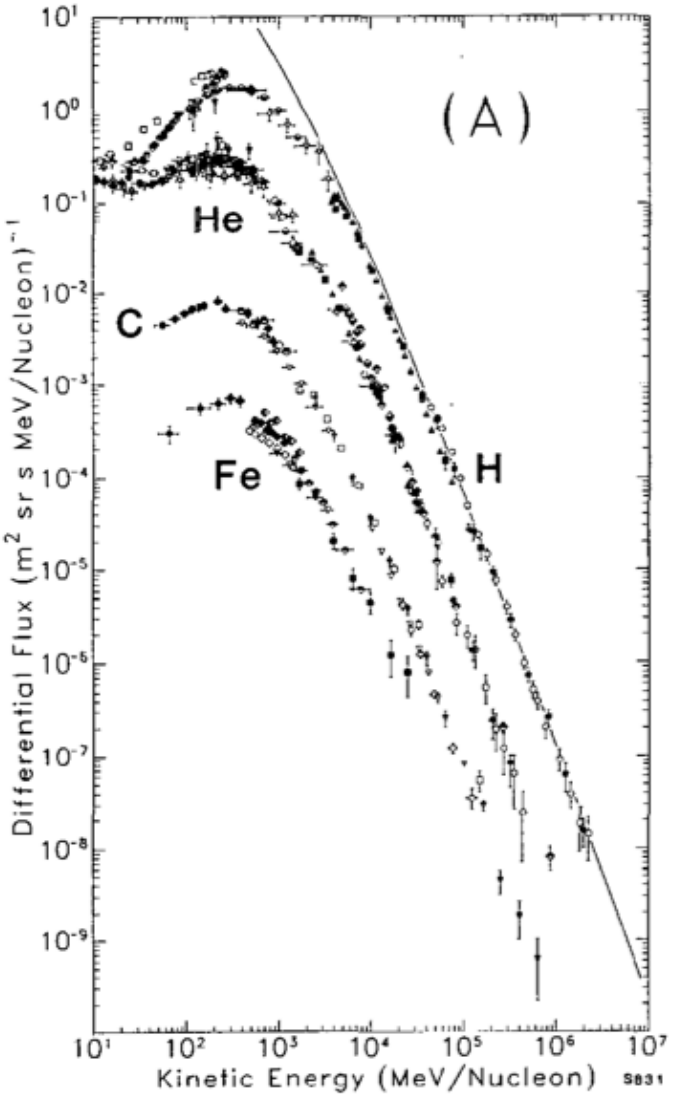

Figure 1.2: Plot showing Galactic Cosmic Ray flux for various components as measured at Earth. The solid black line is an extrapolation of Hydrogen flux to interstellar space by Simpson. [30]

increases in the solar wind provide an increase in the overall amount of charged matter with which Galactic Cosmic Rays can interact as they traverse the interplanetary space. Such interactions modulate the GCR component inversely with solar activity. [16, 21, 26, 28, 32]

1.5 Identification of Ionizing Radiation

A major obstacle in managing space radiation exposure for astronaut crews is the inherent uncertainty involved in any predictions of future solar event occurrences. The timescales involved in the space radiation environment range from minutes for high energy solar particles to reach Low Earth Orbit to years for the modulation of the Galactic Cosmic Ray components near earth and within interplanetary space. [17, 20, 26]

In order to quantify the hazards to humans posed by ionizing radiation, the local radiation field relative to the vehicle and astronaut crews must be known within some degree of confidence. [2, 7] There are multiple possible endpoints to use in the determination of the long term risks associated with ionizing radiation exposure. Until recently, the National Aeronautics and Space Administration (NASA) used a combination of endpoints including absorbed dose and Linear Energy Transfer, along with physiological attributes to determine the cancer risk faced by individual astronauts. [2] Within the last several years, however, the endpoints of interest for risk calculations have shifted to particle energy and ionic charge. [4, 7]

The goal of this thesis is to present the progress made in individual ion identification using the Timepix detector, with the end product being the generation of a local ion spectrum in velocity and charge along with an evaluation of methods and algorithms proposed to achieve this aim. This work focuses on using a single sensor layer in order to minimize power draw and computation requirements for the hardware, and the task is further complicated by the need to assess tracks individually. The chapters that follow provide the necessary background on the hardware, software, and physical processes involved in the transfer of energy from ion to matter, along with the description of the processes used to separate individual ion tracks into charge and velocity bins.

We begin in chapter two with a brief review of the theory of energy deposition in materials and the interaction of ionizing radiation and matter, focusing on the response of silicon since this is the sensor material of choice for this work. In chapter 3, we move to a review of the Timepix radiation detection hardware used as the basis for the analysis in this dissertation. Chapter four is a discussion of the silicon sensor and related concepts used in the detection system. From there we move to a review of current particle identification techniques in chapter five. Chapter six touches upon the data framework constructed to provide a unified analysis basis for several aspects of the identification work as well as describing the sources of data used in the ensuing analysis effort.

Chapter seven contains the core work of this dissertation and is where we discuss the identification methods tested and the results and effectiveness of using a single silicon Timepix detector to characterize a mixed ionizing radi-

ation field. We round out the discussion in chapter eight, where we discuss impacts of expected hardware upgrades on this research area as well as outlining future work and additional applications of our research.

Chapter 2

Energy Deposition in Silicon

2.1 Interactions of Charged Particles with Matter

As a charged particle passes through matter, several process can contribute to energy loss of the particle. Coulomb interactions with atomic electrons dominate for charged particles, though nuclear interactions also contribute to energy loss. At very high energies, radiative effects dominate over ionization losses for charged particles. [15]

While the goal of this work is to characterize charged particles passing through the silicon detector assembly, photons, as well as neutrons, introduce a non-zero signal that must be acknowledged and assessed. Photons traversing through silicon undergo photoelectric capture, Compton or Rayleigh scatter-

ing, photo-nuclear absorption, or pair production processes depending upon photon energy and produce an electron signal in the detector. [15] Neutrons, being uncharged, interact primarily through collisions with atomic nuclei and result in secondary charged particle production. [11]

2.1.1 Scattering Interactions

Coulomb Interactions

Coulomb interactions occur through the Coulomb force between charges, which can be repulsive or attractive. [33] Under the assumption that the system consists of incident and target particles, in the repulsive case with similar charges interacting, the result is a hyperbolic scattering of the incident particle in the laboratory frame of reference. In the attractive case, the trajectory is dependent on the energy of the incident particle, and can lead to capture or radial scattering of the incident particle in the lab frame.

Charged particles are generally nuclei stripped of electrons in the space environment and so have a positive net charge. The ions most often interact with electrons within a target material. [11, 15] In such an interaction, the possible outcomes are scattering or capture of the target electron by the incident ion. Electron capture plays a role in the concept of effective charge (see section 2.2.4 and complicates the calculation of stopping power, especially at low energies for incident ions. [34]

Collisions

In addition to the Coulomb interactions, collisions between incident particles and atomic nuclei in the sensor also occur, though with less frequency than Coulomb interactions. [11] Such collisions can be elastic or inelastic, depending on the energies involved. In the elastic case, a significant portion of the incident ion energy can be transferred to the target and result in a change in energy deposition in the detector as well as a change in trajectory relative to the incident ion trajectory. In the inelastic case, multiple fragments are possible, again with an abrupt impact on the incident ion trajectory. In both cases, the overall effect is to complicate the ion identification task. This is because a track must be reconstructed in order to obtain the information required for identification of the incident ion's charge and energy. Such track reconstruction requires fragment tracking and correlation of the fragments with the incident ion which adds to the computational complexity for the overall system.

Knock-on Electrons

Electrons which have been ejected from the target atom with sufficient energy to be differentiated from the primary ion track are referred to as δ-rays or knock-on electrons. Knock-on electrons have energies ranging from just beyond that sufficient to free them from their bound states, to a maximum energy defined by the kinematic interaction between the incident ion and the target electron. [15, 35]

The kinematic limit for momentum transfer from an incident ion to an electron is described by the quantity T_{max} in equation 2.2. In the frame of a free electron at rest, an incident ion with mass M transfers momentum to the electron with mass m_e, with the electron moving at an angle θ relative to the incident ion trajectory following the interaction. Conservation of momentum and energy yield the following equation for the resultant electron energy, T_e. [35]

$$T_e = \frac{2m_e c^2 p^4 \cos\theta}{m_e c^2 + M\gamma c^2 - p^2 c^2 \cos^2\theta} \tag{2.1}$$

$$T_{max} = \frac{2m_e c^2 \beta^2 \gamma^2}{1 + 2\gamma m_e/M + (m_e/M)^2} \tag{2.2}$$

When the angle θ is zero, T_e is at the maximum value, T_{max}. This maximum value is also used in the Bethe-Bloch formulation for stopping power in equation 2.3 to define the upper limit of the energy transferred to an individual electron during an interaction. [15, 35]

2.1.2 Photon Interaction

Photons traversing matter interact through several mechanisms, with the photon energy and material composition determining the likelihood of the specific interaction process. Presented below is a brief review of the possible interaction mechanisms resulting in energy transfer to a material.

The photoelectric effect dominates at lower photon energies, and is the

process by which a photon is fully absorbed by a bound atomic electron, causing excitation and ejection of the electron from the atom. Such electrons are ejected with an energy equal to the incident photon energy minus the binding energy for the shell from which the electron was ejected. [36, 37]

A related effect occurs when the electron shell vacancy created by an ejected electron is filled within the atom, or, stated more generally, when an excited atom releases energy and drops to a lower shell. This fluorescence effect occurs when an electron within the atom de-excites, releasing a photon with an energy equal to the difference in energy levels between the two electron states. Auger electrons may also be produced by a similar process where the energy produced in de-excitation is transferred instead to an electron which escapes the atom. [15, 36, 37]

Several scattering processes for electrons exist: Rayleigh, Thompson, and Compton. Compton scattering, however, is the only one of these three scattering processes resulting in significant energy transfer. In this process the incident photon transfers a portion of its energy to the scattered electron. Compton scattering becomes the dominant process for photon energies around 60 KeV in silicon. [15, 36–39]

At higher photon energies, above the combined rest energy of an electron and a positron (1.022 MeV), pair production is possible. In this process, the photon energy is converted into an electron/positron pair in the vicinity of a charged particle. Pair production begins to dominate in silicon for photon energies above 15 MeV. [15, 37, 39]

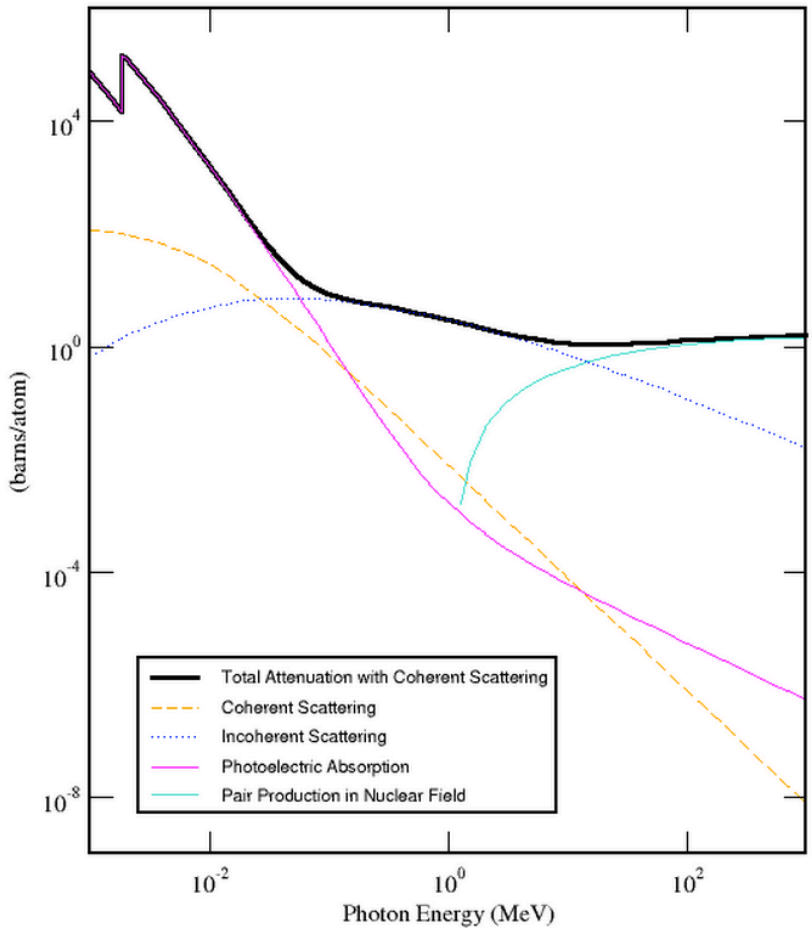

Figure 2.1: Cross sections in silicon for photon energies between 1 KeV and 1 GeV. Rayleigh (coherent) and Compton (incoherent) scattering are shown along with pair production and photoelectric effect cross sections as compared to the sum total of these photon attenuation effects. Note the photoelectric absorption K-edge at 1.8 KeV. This figure was generated using the NIST XCOM database. [39]

2.2 Stopping Power

2.2.1 Bethe-Bloch Theory

The Bethe Bloch Equation describes the dependence of the average energy loss, $\langle \frac{dE}{dx} \rangle$, due to ionization of a material by an incident particle as a function of the charge and velocity of the incident particle. Additional parameters are included to account for phenomena such as the Relativistic Rise and the Fermi Plateau. The equation is valid for a large range of energies, however, modifications must be made for stopping powers below a certain limit (Ziegler-Anderson-Barkas effects). In addition, radiative losses dominate the Bethe Bloch mechanisms at very high energies.

The Particle Data Group Reviews cast the Bethe-Bloch equation in the following manner [15]:

$$-\left\langle \frac{dE}{dx} \right\rangle = Kz^2 \frac{Z}{A} \frac{1}{\beta^2} \left[\frac{1}{2} \ln \frac{2m_e c^2 \beta^2 \gamma^2 T_{max}}{I^2} - \beta^2 - \frac{\delta(\beta\gamma)}{2} \right] \tag{2.3}$$

where T_{max} is the maximum possible energy imparted to an electron as discussed in section 2.1.1.

The Bethe Bloch equation incorporates properties not only of the incident particle, but also of the stopping medium. Since the majority of interactions are coulombic in nature for transmittal of energy from the charged incident atom to the stopping medium, the stopping power is also a function of the electron density of the material.

2. Energy Deposition in Silicon

On the low energy end of the spectrum, the Bethe-Bloch theory begins to break down since the assumption that the incident particle velocity is much larger than the velocity of the electrons in the outer shell of the target material is no longer valid. For particles in this energy regime, the stopping power decreases as the incident ion begins to retain more electrons than it loses during interactions with the target material, changing the particle's effective charge. As the incident ion moves toward a neutral charge state, the coulombic interactions lessen, resulting in a decrease in energy loss. [40] This is often referred to as the Ziegler-Andersen-Barkas region. [15, 34, 41]

For energies above the Ziegler-Andersen-Barkas region, the stopping power decreases to a minimum as ion charge squared over β squared. As the ion velocity increases, the time spent in the vicinity of a given electron lessens. This leads to a reduction in the impulse imparted to/from the ion depending on charge state. [6, 33]

The relativistic rise seen after the minimum ionization point occurs because as β approaches unity, Lorentz contraction results in widening of the interaction cross section seen by the electrons in the stopping material. After a certain point, however, the widening of the packet is dominated by the coulomb shielding effects in the material and the stopping power reaches a maximum known as the Fermi Plateau until radiative effects begin to dominate, at which point the stopping power increases dramatically. [15, 35, 42]

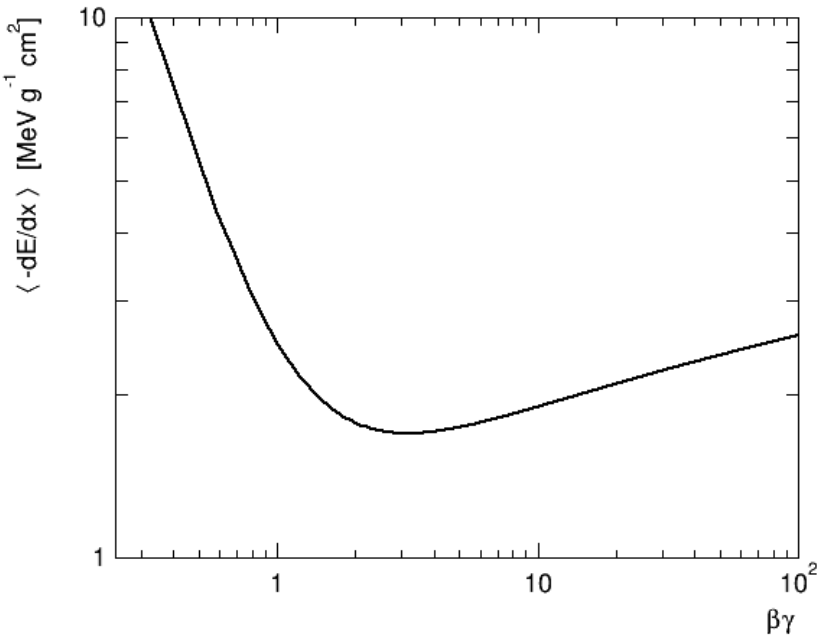

Figure 2.2: Bethe Bloch stopping power curve for protons in silicon

2.2.2 Most Probable Energy Loss

While the Bethe-Bloch Theory provides a way to calculate the average ionization energy loss, the concept of most probable energy loss is important especially for thin detectors. The distribution of energy lost per interaction is described by the Landau-Vavilov distribution. [43, 44] The average of the energy loss distribution is skewed from the distribution mode as a result of low-probability, high-energy depositions. [15, 45, 46]

The most probable energy loss can be calculated by ignoring the interactions which result in the high energy tail of the Landau-Vavilov distribution. The result is a restricted energy loss distribution, with a maximum value im-

posed on the allowed energy deposition range. The average of this converges to the most probable energy loss value as the high energy tail is reduced, and the restricted energy loss approaches a Gaussian distribution. [15, 35, 47]

The high energy tail of the Landau-Vavilov distribution, as it pertains to energy loss in thin absorbers, is due primarily to creation of fast δ-rays. While the emitted δ-rays may escape the sensor, the Timepix unit is able to detect these relative to the primary track prior to their escape. With appropriate pattern recognition, and provided they are not emitted at an angle near the axis along the surface normal, these can be separated from the primary track. Isolating and removing the δ-rays from the primary track allows the use of restricted or most probable energy loss calculations in analysis routines which is considered to be more appropriate for thin detectors such as those used in this work. [15, 35, 43, 44, 46]

2.2.3 Straggling

Ion straggling affects the track patterns recorded by a detector. As the ion traverses the detection material and loses energy, it undergoes multiple small-angle scattering interactions. The overall effect is that multiple ions with the same charge and energy will have differing endpoints as they enter and exit, or stop within, the material.

Lateral straggling is the deviation from the original trajectory perpendicular to the vector of travel. Longitudinal straggling is the deviation from the

continuous slowing down approximation (CSDA) range of the ion along the vector of travel. Longitudinal straggling applies to ions stopping in the material and is a result of the variations in the energy losses along a particle track. [15, 34, 47, 48]

With respect to thin sensors in a mono-energetic accelerator beam, straggling results in fluctuations in the energy deposited within the sensor layer for the individual particles. Each ion traversal contributes a point in the overall Landau distribution for the energy loss in the detector. A small number of events deposit larger fractions of their energy in the sensor, while the majority of the events result in energy losses near the distribution peak, i.e. the most probable value. For ions which stop within the material, the track endpoint will vary due to straggling effects, however the total energy deposit is unaffected by such variations unless energy is carried away by escaping δ-rays. [15, 34, 47]

2.2.4 Effective Charge

Effective charge is an quantity used to describe the variation of charge state of an ion as it traverses a medium. The effect is most pronounced at low energies when the incident ion is moving with a velocity low enough to allow electrons from the surrounding medium to be captured by the traversing ion. Effective charge can then be thought of as an average charge state of the incident ion. [49]

The variation of an ion's charge complicates ion identification efforts, since

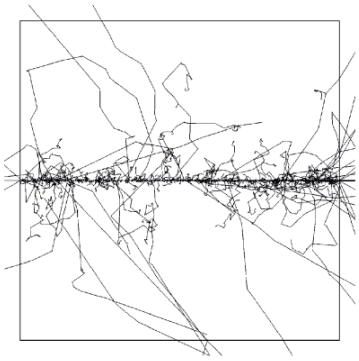

Figure 2.3: This image from [57] shows an example of track-structure resulting from ion passage through a material. The simulation by Kobayashi ran 1000 events through a 6 micron cube and the image shows the tracks of electrons ejected relative to the primary ion path.

the magnitude of Coulobmic interactions will vary in proportion to the variation in ionic charge, however this is not expected to be of significant impact for energies above those of the Ziegler-Andersen-Barkas region. [34]

2.3 Track-Structure Theory

The value of the energy deposited by an ion is not the only item of interest when examining the impact of radiation on materials. The distribution of the energy around the primary track is also important, especially when looking at the effects of ionizing radiation on biological systems or systems of similar size. [50–56]

The distribution and range of energy deposition surrounding the primary ion track has been studied by Chatterjee, Katz, and others. [50, 52, 58] Their

work focused on determining the spatial distribution of the energy from secondary particles in the areas immediately surrounding the primary ion track. This becomes important when looking at biological systems with feature sizes that fall within the extent of the energy deposition surrounding the primary track.

In addition, work on passive radiation detectors such as film badges and nuclear track detectors is impacted by the radial extent of the energy deposition surrounding a primary ion track based on the film grain size or etching parameters. [59]

2.4 Linear Energy Transfer

Linear Energy Transfer (LET) is the average energy absorbed per unit path length of a particle traversing a medium. Stopping power and LET are distinctly different quantities in that the former deals with energy lost by the incident particle, while the latter is related to the energy retained by the target material. [3] There are subtle variations of the energy loss and related assumptions of track structure that further complicate the definition. The most significant aspect is that of Charged-Particle Equilibrium (CPE). Invoking the assumption of CPE implies that the number of secondary particles entering the sensor volume are the same as those leaving the sensor volume. [11]

With the Timepix device, the concept of CPE applies to δ-ray production and escape. The benefit of the Timepix device is that the tracks from the

high energy δ-rays, those most likely to have a range sufficient to escape the sensor volume, are detectable in the Timepix data. Because the Timepix data contain such spatial information, these high energy knock-on electrons can be identified, isolated from the primary track, and excluded from the LET calculation.

Chapter 3

The Timepix Application-Specific Integrated Circuit

3.1 Pixel Detectors

Pixel detector construction covers a broad range of designs, from photon detecting Charge Coupled Devices (CCDs) found in digital cameras to hybrid detector technology found in current advanced radiation detection hardware. In general, pixel detectors consist of a collection volume used to create the signal from the incident radiation and a segmented grid readout system used to collect, amplify, and record signal information for data analysis or storage. [9, 60]

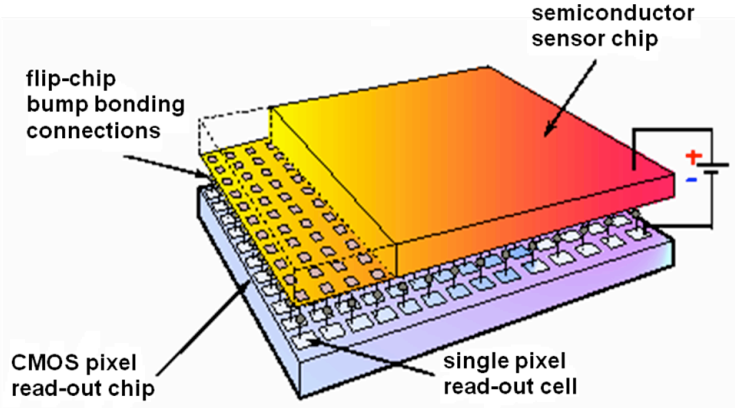

Figure 3.1: The primary features and assembly of the Medipix family of hybrid pixel detectors [62]. Note that the features are not to scale.

Pixel detectors can be subdivided based on how these components are arranged. In a hybrid pixel detector, the readout system and the collection volume are physically separate components. Monolithic pixel detectors, such as Silicon On Insulator (SOI) devices integrate the readout system components into the detector volume. Each has benefits and drawbacks which have been discussed in detail in works by Spieler, Lutz, and Rossi. [9, 10, 60]

A benefit of hybrid detectors is that the material of the sensitive detection volume can be chosen to match the radiation field of interest without modification of the electronics. While silicon provides a good signal response to a broad range of ionizing radiation which is applicable to the work in this dissertation, other materials provide higher efficiencies for measurement of the X-ray spectra used in imaging applications. [9, 61]

3.2 The Medipix Technology

A family of hybrid pixel detectors has been developed over the last two decades at CERN within the Medipix Collaboration. [62] Originally designed as a photon counter for medical imaging, the Medipix technology has evolved into a set of radiation-hard and highly capable devices with a broad range of applications. [63]

The first iteration of the Medipix Application Specific Integrated Circuit (ASIC) was developed at CERN as a photon counting detector with application to medical diagnostic imaging, such as mammography. [61, 64] This development work yielded a hybrid pixel detector with a 64 by 64 grid of pixels at a 170 micron pitch, a large dynamic range, and a global charge discrimination threshold with local threshold adjustment bits in each pixel circuit. [64, 65]

The second generation of the technology, the Medipix2 device, was designed to provide a grid of 256 by 256 pixels at a 55 micron pitch, with similar dynamic range and both an upper and a lower charge discrimination threshold. During data collection, the on-board pixel counter is incremented for each signal registered within the window created by the upper and lower energy thresholds. [66]

3.3 Timepix

3.3.1 Chip Development

The Timepix chip is a variant of the Medipix2 pixel detector development which has been adapted for use in High Energy Physics. The Timepix uses a single discrimination threshold but has 4 modes of operation: Medipix, Timepix-1hit, Timepix, and Time Over Threshold. Medipix mode is a hit counting mode similar to that found in the Medipix version of the device which increments the pixel counter for every time the signal exceeds threshold during the acquisition window. Timepix 1-hit mode is a binary hit mode which increments the counter once if the signal exceeds threshold once or more during the acquisition time window, leading to a hit/no-hit record for each pixel. Timepix mode records the number of clock cycles between the time at which the collected charge signal exceeds the threshold and the end of the collection frame. Combined with the timestamp in the meta-data for the beginning of the acquisition frame and the acquisition time window, this arrival time mode allows the measurement of the time of arrival of the charge cloud at the sensor/readout pixel interface. [62, 67, 68]

The inclusion of a Wilkinson-type Analog-to-Digital Converter (ADC), also called a linear ramp converter [11], in the pixel electronics adds the capability for a Time Over Threshold (TOT) measurement. The Wilkinson-type ADC allows the collected charge to be translated into on-board clock counts corresponding to the amount of time the signal remains above the pixel thresh-

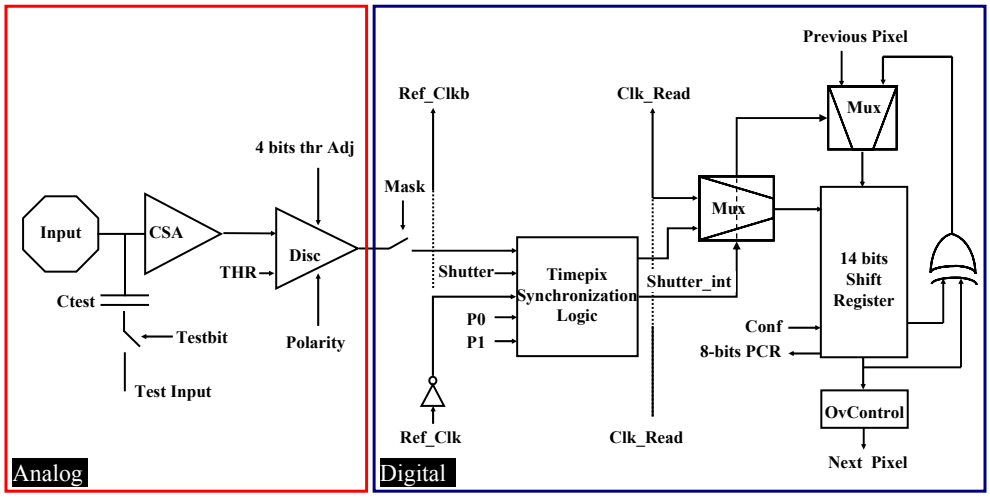

Figure 3.2: Each pixel of the Timepix ASIC contains an analog and a digital component to provide signal acquisition and digitization within each pixel footprint. [72]

old. [69] The combination of this timing information with the feedback current used to dissipate the collected charge allows the device to be calibrated to provide energy deposition in each pixel. [62, 70, 71] TOT mode is the mode used within this work since this is the operational mode best suited to provided energy deposited per pixel for mixed field radiation.

Each pixel in the Timepix ASIC contains an analog and a digital component of the circuit. The analog portion collects the signal and contains a charge sensitive preamplifier while the digital section provides for the on-board signal digitization and data storage until the next readout operation. [67]

3.3.2 Analog Pixel Circuit

The analog portion of at Timepix pixel circuit contains a preamplifier and a discriminator. [67] The preamplifier is a charge-sensitive type, meaning that the amplifier output is proportional to the charge collected, and is based on a design proposed by Krummenacher [73]. The Krummenacher-type preamplifier, due to the specifics of its design, has the advantage of reduced noise sensitivity and includes leakage current compensation. The preamplifier integrates the collected charge and shapes the collected signal. [72]

The bias current in the Krummenacher preamplifier can be set via the Ikrum DAC on the Timepix ASIC. The bias current controls the charge shaping in the preamplifier, and hence the return to zero in the Wilkinson-type conversion into TOT counts. [72] As a result, changes in Ikrum can have significant impacts on data collection as well as calibration application, though such impacts can be mitigated by using consistent Ikrum settings during both data collection and instrument calibration.

The pixel discriminator threshold can also be set via DAC settings on the Timepix ASIC. This allows per-pixel threshold adjustment beyond the global threshold setting, resulting in a nearly noise free measurement as discussed in the section on threshold equalization. [72]

3.3.3 Digital Pixel Circuit

The digital portion of the circuit contains the pseudo-random counter, shutter logic, and clock input. The pseudo-random counter is used to retain the digitized signal information until the data is read out from the chip. [67,72]

Signal shaping takes place in the preamplifier, and the shaped signal is digitized by the counting logic in conjunction with the global clock signal while the acquisition shutter is open. The resulting counts in the pseduo-random counter complete the Wilkinson-type ADC conversion and produce a Time Over Threshold result in the pseudo-random counter that can be read out and converted. [67, 69, 72]

The use of a pseudo-random counter, more commonly referred to as a Linear Feedback Shift Register (LFSR) increases digitization speed while reducing overall circuit complexity. [74, 75] A pseudo-random counter is a shift counter with one or more feedback loops, depending on design. The output signal of the shift register at any given time is a deterministic function of the previous state, but the output for sequential states can seem to be a a random sequence. The fact that the sequence repeats with a certain periodicity leads to the label of pseudo-random counter. See Appendix E for additional discussion.

The result is a shift register, which due to the feedback loop, utilizes fewer components to achieve a similar count limit compared to a shift register without a feedback loop. [75] And because the resultant random sequence is deterministic based on hardware design, it results in a count value that can retrieved

via look-up table after data readout.

3.3.4 ASIC Readout

A few comments regarding data readout are worthwhile at this point. The data, as read directly from the Timepix chip, are not suitable for higher level analysis. The data must first be processed to convert pseudo-random counter to true values, as well as to reconstruct the values for each pixel from the raw data stream.

Each individual pixel contains a 14-bit shift register, and pixels are arranged in a 256 by 256 element matrix. When the data are read out from the Timepix, each column is shifted out one bit at a time, with the most significant bit shifted out first. This results in a data stream consisting of 14 * 256 segments of 256 bits each, or 917504 bits per data frame. For this data to be useful, the bit-wise data must be restructured back into the 14 bit values corresponding to each pixel value. Following pixel data reconstruction, the pseudo-random count values can be converted to the corrected count values via a look-up table for the implemented pseudo random counter design.

The preceding discussion points out that the amount of data processing required to utilize the Timepix data stream for analysis is not insignificant. While existing computers have sufficient capacity to complete the task, the same is not necessarily true for embedded hardware systems, such as those which may be used for space exploration missions. One of the drivers for

utilizing a single Timepix device for radiation field characterization is the minimization of the processing operations, and hence computational power, required to achieve an operationally useful output from the hardware utilizing a Timepix detector assembly.

3.3.5 Threshold Equalization

Due to variations in materials and processing techniques, the transistor response across all pixel circuits is not perfectly uniform. To account for this, the pixel electronics contain a global Digital-to-Analog Converter (DAC) which is used to apply a detection threshold value to the entire pixel array, as well as a pixel-specific threshold adjustment DAC to allow adjustment within individual pixels around the global threshold setting. The combination of these two allows each pixel threshold to be set just above the pixel noise threshold. [70, 72]

Threshold equalization is the process by which these DAC values are set and the device is brought into a state where the output signal is nearly noise free. In addition, the pixel electronics also contain a digital mask bit allowing individual pixel values to be removed. This last feature is important in the case where a few individual pixels exhibit noise levels beyond the local adjustment range after threshold equalization has been performed. [70, 74]

3.3.6 Timepix Calibration

Calibration of the Timepix detectors is performed to allow conversion from the measured Time Over Threshold into deposited energy on a per-pixel basis. This requires that each pixel in the detector be calibrated independently to account for individual pixel variations. In order to calibrate individual pixels, the energy deposition from the calibration sources used must fall completely within the pixel of interest, which requires that only single pixel hits be used in the calibration process. [71,76] See Appendix D for a more detailed description of the calibration process.

3.4 Hardware Limitations

The Timepix hardware, in it's current state, does have a few drawbacks in terms of signal generation and acquisition. The most significant of these are what are referred to as the 'volcano' and 'saturation' effects.

The 'volcano' effect is an apparent reduction in the measured TOT counts, and hence measured energy, within the core of larger clusters. The result is a large cluster where energy deposition in a single pixel often exceeds 1 MeV in several places, but with a characteristic minimum where the cluster maximum would be expected. The result, when plotted in two dimensional position and in energy results in a structure that looks very much like the caldera of a volcano. This effect is more pronounced for energetic heavy ions, and various mechanisms have been proposed to explain this behavior within the data.

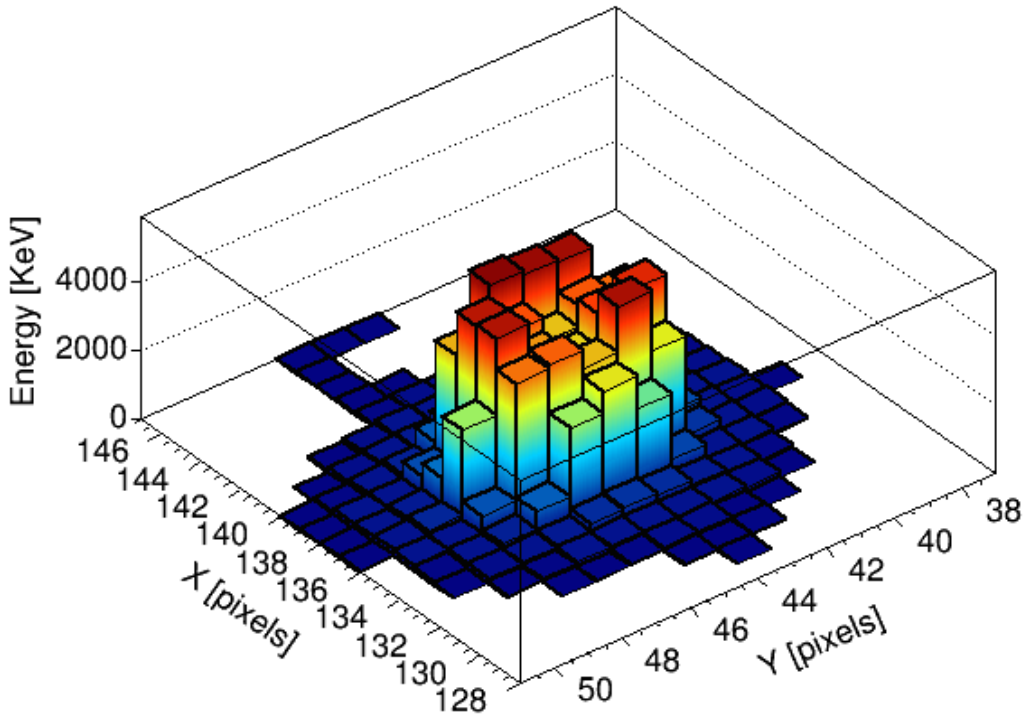

Figure 3.3: The 'Volcano Effect' is shown for a 500 MeV/nuc iron cluster incident normal to the detector surface (0° incidence) with high localized energy deposition along the track core. The large amount of collected charge in a single pixel initiates an over-current protection circuit within the pixel, leading to a shape similar to that of the caldera of a vocano when the cluster is plotted in three dimensions.

The mechanism which is thought to be the cause of the volcano effect is an over-current suppression circuit built into each pixel of the detector. Above a certain voltage level, the circuit shunts the charge to ground in order to avoid damage to the ASIC.

The 'Saturation Effect' is a result of the charge sensitive preamp implemented in the pixel circuit. The signal generated from the preamp becomes non-linear above the preamp saturation point. In terms of the effect on the calibration curve, beyond the preamp saturation point the calibrated energy value increases rapidly and then decreases a short while later with respect to measured TOT counts. Since the calibration relies upon a linear response of the Timepix above several hundred KeV, the non-linearity in the detector response results in a systematic error in the conversion of TOT counts to energy. [71] Future iteration of the Timepix ASIC are expected to address this issue, but with the current Timepix devices, and in this work, compensation for the saturation effect is addressed in the data processing and analysis algorithms. [77]

Other mechanisms contributing to the general signal degradation are the plasma effect coupled with carrier recombination. [78, 79] When the carrier density is large enough to produce a plasma condition within the detector, it decreases the overall collection time while increasing local charge carrier freedom as the external electric field is screened by the local charge cloud. The resulting increase in mobility of the two opposing charge carrier components allows more rapid carrier recombination, leading to an overall decrease in the

charge collected at the interface between detector and Timepix ASIC. [79, 80]

Other items considered drawbacks in this purview, such as silicon's response to the UV spectrum or fluorescence effects in silicon, are more specific to the application of interest and may be considered beneficial in alternate applications. For example, in situations where the incident radiation field is a known photon field, the response of the silicon Timepix detector can be used to evaluate dose. [74] However, in the case of heavy ion identification, both of these items produce signals which may add complexity to identification efforts.

Chapter 4

Silicon Sensor Chip

4.1 Silicon as a Radiation Sensor

One of the benefits of using a hybrid detector is the ability to select the sensor material to suit the radiation field of interest. Material selection is important in detector design both to optimize performance for the detection task at hand and to minimize experimental impacts resulting from damage to the sensor from intense radiation fields. [81, 82] Damage effects range from minor impacts, such as lattice dislocations which result in decreased carrier mobility, through destructive effects such as electron avalanche breakdown which can lead to device burnout. [60, 83]

For the space radiation environment, a high quality and well developed sensor material is needed which has a broad range of response across the full charged particle spectrum to allow detection of low energy electrons through

very high energy heavy ions. Silicon sensors provide a broad detection spectrum and have the benefit of being well documented in terms of response. In addition, silicon is highly developed in terms of processing, and high quality detectors are widely available. [84] For these reasons, this work was carried out using silicon sensor materials.

4.2 The P-N Junction

The basic pixel components of the Timepix detector assembly pixel cell is shown in Figure 4.2. This basic pixel cell contains a p-n junction in the sensor layer bonded to the Timepix readout pad for the cell via solder bump-bonding. [9] The p-n junction provides the mechanism by which free charge carriers can be removed from the sensitive detection volume, allowing only the charge produced by interaction with ionizing radiation to be collected. [60, 83, 85]

This is accomplished by using different dopant elements to change the charge concentration in the p and the n regions of the material. The differing concentrations of charge then lead to an inherent bias voltage across the boundary between these regions of opposing charge concentrations. Application of an external bias voltage across the boundary, opposite to the inherent bias voltage, extends the width of the region in which free charge carriers are depleted. When the bias voltage applied is large enough, the depletion width extends across the entire silicon sensor layer leading to a condition known as full depletion, in which all free charge carriers have been removed from the

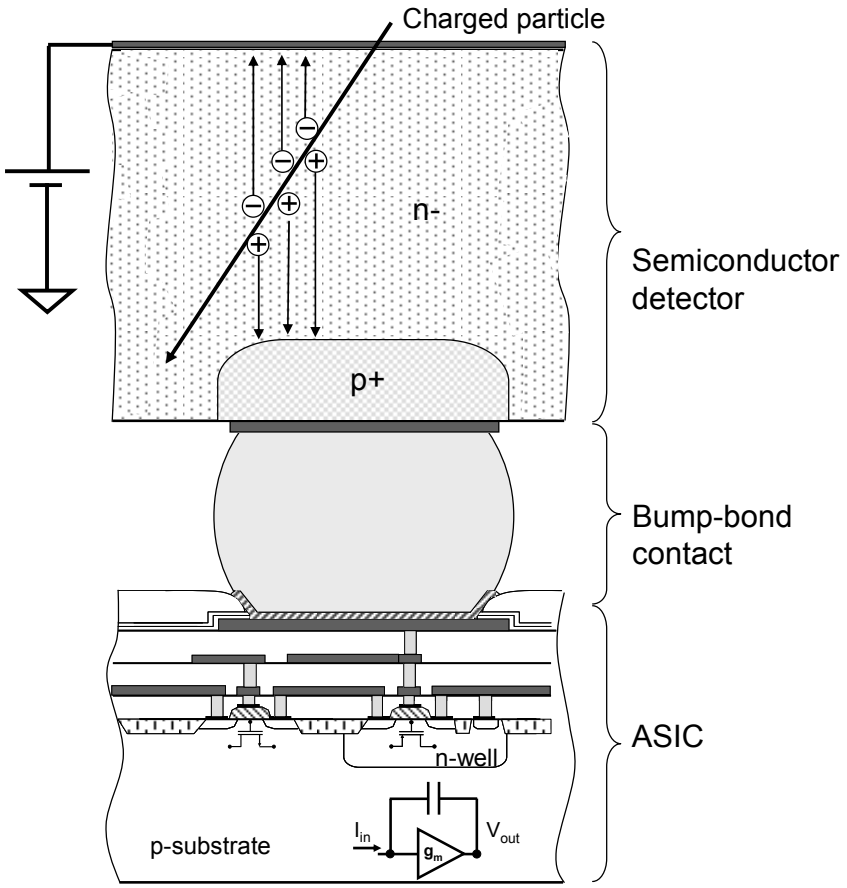

Figure 4.1: A hybrid pixel cross section is shown with the relevant features. [86]. The figure shows, from top to bottom, the silicon sensor with p-n junction, bump bond connecting p-n junction to ASIC collection pad, and an ASIC pixel circuit.

silicon volume. [10, 60, 83]

Thermal excitation can cause release of additional free carriers, however, the Timepix detector provides a mechanism to allow threshold adjustment within each pixel to set a baseline threshold for signal acquisition, allowing rejection of the thermal noise signal. [70]

The sensor of the silicon Timepix assembly is a monolithic silicon sensor consisting of a grid of 256 by 256 p-doped implant regions in a bulk n-type silicon chip. The patterning of the implant regions corresponds to the spacing and layout of the collection pads on the Timepix ASIC. [67]

4.3 Charge Carrier Motion and Signal Production

The process of ionization in the sensor material frees electrons from the bound states within the constituent atoms. Ionization results in the creation of an electron free to move within the material, and a corresponding electron vacancy, or hole, that also moves as the shared electrons still bound within the material move to fill the vacancy created by the ionization.

4.3.1 Signal Formation

In silicon, the average energy needed to create an electron-hole pair is approximately 3.6 electron volts (eV) at room temperature. [83,87] The energy

for this ionization is provided by the the incoming particle as it passes through and interacts with the sensor material. The energy deposited creates free carriers, electrons and holes, which move under the influence of built in and applied electric fields. [85]

4.3.2 Carrier Drift and Diffusion

Free charge carriers are influenced by both intrinsic and applied electric fields, causing a drift movement according to carrier charge and field polarity. The dopant concentrations within the p-n diode junction create an intrinsic electric field, causing carrier drift. Application of a bias voltage across the junction further modifies the carrier drift.

Applying a bias voltage opposite that to the built-in voltage (which results from the intrinsic electric field) of the p-n junction creates a reverse bias situation, and when the applied bias is greater than the built-in bias, a depletion region is formed where charge carriers drift away from the p-n junction. This creates a region in the semiconductor where excess charge carriers are removed and only thermally generated charge carriers are present. This thermally generated charge carrier component is the semiconductor dark current. [83, 85]

Charge carriers also undergo interaction with one other. In the case of like-charges moving together in the applied external electric field, this leads to diffusion of charge carriers from regions of higher concentration to areas of lower concentration. In terms of signal generation resulting from ionization,

this leads to both a component parallel to the bias field (drift) and a component of movement perpendicular to the bias field (diffusion). The diffusion component perpendicular to the field results in a variation of charge cloud diameter collected at the sensor/ASIC interface which is dependent upon the depth at which the ionization interaction occurs. Thus the charge carriers released from an interaction further from the collection pad are more diffuse than those released from an interaction near to the pad. [88–90]

4.3.3 Induced Charge

The high density of carriers released during ionization of the semiconductor material results in induced image charges in the bump bonds and collection pads of the ASIC. Over the full course of the carrier movement to the collection pads, the induced charges sum to zero. [10, 74, 91, 92] Due to the difference in hole and electron mobilities, combined with the behavior of the integrating circuit of the Timepix ASIC, the charge integrated in the pixels affected by the induced charge does not necessarily reflect the zero sum, and this results in low levels of charge integration in pixels which are not covered by the arriving charge cloud produced by the initial ionization process. [93]

Chapter 5

Particle Identification Techniques

The Timepix device is used in accelerator systems in various roles, however the application of the device to space-borne missions presents restrictions on hardware not applicable in the lab setting. [94–96] In order to approach the problem of particle identification in the restrictive case of a single sensor Timepix, we first survey existing particle identification techniques for both high energy physics experiments and space-based particle identification.

For accurate identification of charged particles in high energy physics experiments, a magnetic field is typically applied within the region of particle tracking in order to measure particle momentum. Velocity measurements are then required in order to determine the particle mass from the momentum measurements. Time of Flight (ToF) measurements are one method to deter-

mine velocity, but require sufficient measurement speed or instrument size to capture the information of interest for high energy particles. [97, 98]

Detectors providing spatial information about a particles trajectory are important for isolating individual events, tracking particles as they move through various components of the experimental apparatus, and measuring the necessary track parameters to determine the ion momentum. [99] A short survey of the various instrumentation types used in energy and position measurements needed to determine momentum and velocity in the accelerator environment are discussed in the sections that follow.

5.1 Accelerator Particle Detection and Identification

5.1.1 Bubble Chambers and Emulsions

When an ion passes through a material, it deposits energy. If the material is at the proper temperature and pressure, the energy deposition can initiate a local boiling of the material, serving as a nucleation site for further boiling. Using this effect, bubble chambers provide a method to generate a visible track with the generated ion traversal track captured via photography to record the events. In the presence of a magnetic field, the particle tracks will curve, as described above, allowing the particle properties to be determined. [99]

Nuclear Emulsions use a similar approach in that they provide a way to

visualize an ion's passage through a material, but do so directly on to a photographic film or plate. Nuclear emulsions, used as individual ion trajectory trackers, are generally thicker than film emulsions, but utilize similar technology. The grains of material in the emulsion are sensitive to the energy deposition as an ion traverses the material, darkening as energy is lost in the individual grains. The resulting series of darkened grains, which are on the order of microns in size, in the material provide a way to view the particle track following development of the emulsions. [11, 100]

In some respects, the Timepix detector can be thought of as an active readout nuclear emulsion. The data output from the Timepix is a series of intensity graded (i.e. energy graded) 55μm square pixels, which are larger than, but analogous to, film grains in an emulsion. The Timepix also registers track patterns, and while the spatial resolution is less for a Timepix than for nuclear emulsions, some of the same techniques used for nuclear emulsions may be applicable in some form to Timepix data analysis. [58, 59, 100]

5.1.2 Scintillation Detectors

Scintillation detectors utilize specific materials, such as doped sodium iodide, that produce light when particles interact in the detector volume. The light is converted into an electronic signal through the use of a photo-diode or photo-multiplier, the latter of which uses a series of amplification steps where the electron generation from the incident photon signal is increased, and the

generated signal is collected as a measurable voltage pulse in the front end electronics. [11, 15]

The number of pulses registered from a scintillation detector can be recorded to give a particle hit count for the detector area. Using a series of individual detectors, the presence of particle passage can be determined, and this technique is used in several experiments including the Large Hadron Collider beauty experiment (LHCb) and the Alpha Magnetic Spectrometer on the ISS (AMS-02). [101, 102]

5.1.3 Drift Chambers

Drift chambers consist of a series of long thin 'straws' containing a gaseous volume where the ionization occurs. A low intensity electric field is applied to drift the released electron signal along the straw axis to an amplification region near the collection anode. Since the gasses utilized in the drift chamber construction are chosen for consistency in drift velocity and the applied electric field is known, the time required to collect the signal provides location information for the interaction. [99, 103]

5.1.4 Time Projection Chambers

Time Projection Chambers (TPCs) are similar in concept to drift chambers, but operate on a larger scale. Both drift chambers and TPCs can be used for particle tracking, but a TPC uses a large volume instead of several small

volumes, with a two dimensional detection grid incorporated in the endplate of the detector volume. [99, 104]

5.1.5 Transition Radiation Trackers

Transition Radiation Trackers are a combination of the drift chamber tracking detectors with materials in which transition radiation is produced by the traversing relativistic particles. The angle of the transition radiation is a function of the Lorentz factor,γ, so the identification of the transition radiation emission angle relative to the particle direction provides a measure of both trajectory and γ. [105]

5.1.6 Semiconductor Detectors

Semiconductor detectors work on principles similar to those discussed in chapter 4, but can vary greatly in design and construction. The two primary types to note with respect to the current discussion are strip detectors and pixel detectors.

Strip detectors use a series of semiconductor strips to isolate the location of a particle track while gathering information about the amount of ionization. Double sided strip detectors are made up of two sets of strip detectors aligned perpendicular to one another on opposing sides of a semiconductor wafer. This alignment allows a two dimensional measurement of the track position. Layering such detectors can provide a third dimension to the measurement.

[9, 10, 60]

Pixel detectors can be in designed the form of a hybrid detector like the Timepix device, or such detectors can be designed and produced in a monolithic detector where the electronics for the detector are built directly into the sensor material. Silicon On Insulator (SOI) detectors are an example of this type of construction. Pixel detectors may also be combined to provide additional tracking capability. [9, 10, 60, 95, 106]

5.1.7 Calorimeters

Calorimeters are used to measure energy deposition of traversing particles with the intent of stopping the particle and recording its full energy. Calorimeters can be classified into electromagnetic and hadronic calorimeters depending upon the type of particles the calorimeter is designed to measure.

Electromagnetic calorimeters measure the energy of electrons, positrons, and photons, while hadronic calorimeters measure the energy of hadrons. Calorimeters utilize absorber materials which act as the detectors, or use absorber material interleaved with drift chambers or other energy sensitive tracking detectors, and measure the energy loss as the interactions with the absorber materials reduce primary ion energy and create secondary particles. Hybrid calorimeters are being built to detect both the hadron component and the lighter secondary fragments which may otherwise remain unmeasured in traditionally segmented calorimeter arrangements. [45, 107]

5.1.8 Cerenkov Detectors

As a particle moves through a material at speeds faster than the speed of light for the material, Cerenkov light is produced. The Cerenkov light forms a conical surface in the direction of travel which can be detected directly by, or through reflection to, imaging detectors or other photo-detectors. The angle of the produced Cerenkov light provides velocity information about the particle traversing the medium. [11, 101, 108]

5.2 Particle Detection and Identification in Space

5.2.1 Tissue Equivalent Proportional Counters

Standard proportional counters consist of a gas filled volume with an anode wire to collect the ionization charge, while a multi-wire proportional counter uses several anode wires within the gaseous volume. A Tissue Equivalent Proportional Counter (TEPC) contains a gas in the detection volume which is chosen such that it simulates the energy loss characteristics of tissue. [11]

Single anode TEPC devices are flown aboard the International Space Station as part of the operational radiation detection program to track crew radiation exposure. In addition, the measurements from ISS TEPC hardware are used as a verification for other radiation detection experiments on-board, such as bubble detectors or the Timepix-based ISS REM instruments. [109]

5.2.2 Charged Particle Telescopes

Charged particle telescopes utilize a series of detector planes to track individual particles as they pass through the instrument. Energy deposition in the individual detectors, associated with the individual plane crossings, provides an energy loss measurement for the entire track. Particle identification can be achieved within the bounds of energy and direction that the device has been optimize to measure.

Such instruments have been utilized both inside and outside the ISS, as well as on interplanetary satellite missions. Comparisons of internal and external charged particle telescope measurements aboard the ISS show differences in the measured particle spectra resulting from mass shielding from the ISS vehicle components. [110, 111]

5.2.3 Alpha Magnetic Spectrometer

The Alpha Magnetic Spectrometer on the ISS (AMS-02) contains a full suite of particle detection and identification instrumentation, similar to what would be found at ground-based particle accelerator facilities. This provides an unprecedented look at the particle field in Low Earth Orbit. [102] Unfortunately, the mass and power requirements for such an instrument prohibit its use as an operational radiation monitor or its application to exploration missions.

Chapter 6

Data Collection and Analysis

6.1 Data Sources

6.1.1 International Space Station Radiation Monitoring Data

As discussed in Chapter 1, the primary application of the information gleaned from ion charge and velocity identification is toward protection of on-orbit crew and systems. In order to further this use, the National Aeronautics and Space Administration (NASA) has delivered several Timepix-based devices to the International Space Station (ISS). These devices, officially dubbed as Radiation Environment Monitors (REMs) by NASA, have been operating on orbit since late 2012, and have provided data for analysis as well as operational experience using the Timepix hardware in crewed spaceflight ap-

plications. [112]

Frame Rate Adjustment and Related Algorithms

The REM instruments aboard the ISS encounter a significantly changing radiation field over the course of a 24 hour period, with particle fluxes ranging over several orders of magnitude. [112] In order to minimize the data transfer loads while maintaining particle tracks that are well isolated from one another - a feature that is critical for individual particle identification and analysis - frame rate adjustment algorithms were developed and included in the ISS REM flight software that allow the flight software to use data feedback in order to adjust acquisition parameters based on existing environmental conditions. Thresholds and detector parameters can also be updated from the NASA Mission Control Center using initialization files for each unit. [113, 114].

Prior to the launch and deployment of the ISS REM hardware, basic simulations were carried out using FLUKA to generate energy deposition tracks in a silicon wafer with the same dimensions as that expected for the ISS REM hardware in proton fields with fluxes similar to those expected on orbit. [114–116] The FLUKA data was generated using a bin sizing corresponding to the Timepix pixel pitch of 55 microns, and the resulting raw data from the FLUKA runs was reprocessed to generate Timepix-native raw data files which could be viewed and processed using standard Pixelman software. [117]

The frame rate simulation scored energy deposition in the specified binning geometry only and did not incorporate any charge carrier dynamics or device

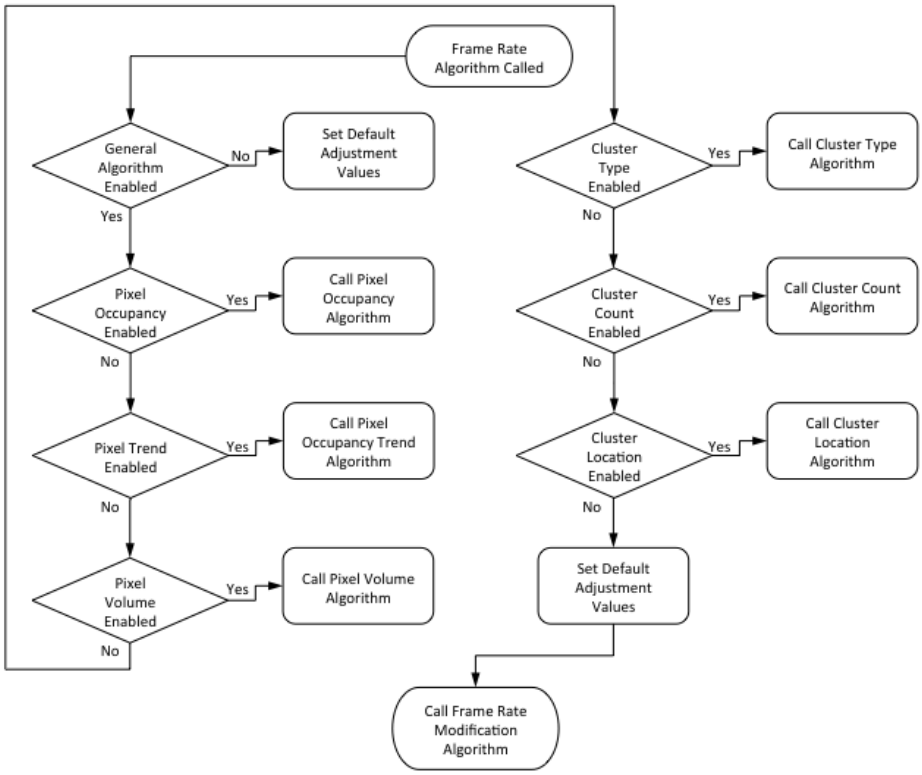

Figure 6.1: Top level flow of the frame rate algorithm is shown. Each of the subroutines can be deactivated to provide maximum flexibility in frame rate response.

specific effects beyond geometry and basic material composition of the detection hardware. The simulation results provided information on what range of acquisition times would be required for the proton fluxes under investigation. It also revealed that effects from track overlaps would impact the data keys, such as cluster count and pixel occupancy, needed for feedback. This allowed the frame rate algorithm to be written with such effects taken into account, and it also allowed the proper ranging of variables used for the feedback parameters.

The frame rate adjustment algorithm implemented in the REM flight software uses multiple data keys to allow it to respond to changes in the local radiation flux. Individual sub-algorithms specific to these data keys can be activated independently of each other, or used in series, to maximize the flexibility of the acquisition parameters. Pre-set comparison values are included in initialization files read by the flight software, allowing the users to update these setting remotely.

The flight software changes the data acquisition parameters to increase or decrease frame acquisition times depending on algorithm feedback. Once the acquisition time reaches a minimum (user-set) value, the time delay between data frames is increased until flux begins to decrease, at which point time delay between frames is decreased until the minimum acquisition time threshold is exceeded again and operation returns to modification of the frame acquisition time.

The data keys used are pixel occupancy, pixel occupancy trends, pixel

volume, cluster type analysis, cluster count, cluster count trends, and cluster localization. The adjustment algorithm checks an activation setting in the initialization file to determine whether each sub-algorithm is executed, and the algorithm proceeds until one of the activated sub-algorithms updates the frame rate. If none of the sub-algorithms are activated, the current frame's pixel occupancy is used to set the frame rate relative to the lowest pixel occupancy threshold in the initialization file.

The first level of the algorithm utilizes the number of non-zero pixels relative to the total number of pixels in the detector, termed pixel occupancy. The pixel occupancy is compared to a series of threshold settings and the acquisition parameters are increased, held constant, or decreased based upon the current pixel occupancy value relative to these thresholds. Thus, if the occupancy jumps sharply, the acquisition time is reduced in proportion in order to keep the occupancy near the threshold value.

The next sub-algorithm compares pixel occupancy values over the last three data frames to establish a trend in the changes in occupancy. If the variable of interest is increasing or decreasing over the three frames, showing a locally consistent trend, the acquisition parameters are adjusted accordingly. Otherwise the parameters are held constant.

Continuing on in the order of sub-algorithm activation, pixel volume is checked relative to two values used for comparison, where pixel volume is the sum of all pixel TOT values in the frame. If the current value is between the two set points, the frame rate is held constant, otherwise the frame rate is

adjusted to maintain the pixel volume near the values set in the initialization file.

The cluster type analysis sub-algorithm utilizes the cluster sorting routines within the Pixelman software [117] to classify a pixel cluster as a blob, straight track, or curly track. The cluster type with the highest count in a given frame is used to adjust the frame rate relative to initialization file settings for the respective track type, again in order to maintain the current value close to the value specified in the initialization file.

Cluster count and cluster count trending are used following the cluster type sub-algorithm. This is analogous to the pixel occupancy sub-routine but uses a separate comparison value set in the initialization file for cluster count and/or cluster count trending.

Wrapping up the description of the frame rate algorithm operation is the cluster localization sub-algorithm. This algorithm divides the current frame into a series of square subgrids. The cluster count within each of these subgrids is determined using the cluster center points. The average number of clusters per subgrid is determined, and the number of subgrids above or below a fractional amount of this average is calculated. The frame rate is then adjusted to bring the subgrid values within the fractional tolerance of the average.

Log files created by the ISS REM flight software provide information on which of the sub-algorithms is used to modify the acquisition parameters as well as how the parameters were modified relative to the previous data frame. Upon deployment of the ISS REM hardware on-orbit, only minor modifica-

tions to the pixel occupancy thresholds were required to obtain well-separated clusters.

Data Transfer and Processing

For the ISS REM hardware, data is acquired for each instrument on the Station Support Computer where the unit is deployed. [112] The data is then transferred by the flight software onto the ISS file server where it is downlinked to NASA Mission Control (MCC). The data is then transferred to the Space Radiation Analysis Group file servers by the MCC Houston Radiation Console operator.

Automatic transfer of the data from SRAG servers to University of Houston servers is done twice daily. The first transfer moves data from NASA servers to UH servers for calibration application and initial processing. The second transfer returns the calibrated and processed data to NASA SRAG for further analysis.

Initial processing of the raw data received from NASA includes application of the calibration information to convert from TOT counts into energy per pixel. The data is also converted to a ROOT based file format and basic properties such as dose, Linear Energy Transfer, and orbital trajectory information are calculated and saved to files. The raw data is subdivided during processing into individual files based on Greenwich Mean Time (GMT), date, and on ISS REM unit name so that one file contains data for one day (in GMT) and from one instrument.

6.1.2 Accelerator Data

Over the last several years, Timepix based data has been taken routinely at HIMAC in Chiba, Japan, as well as at NSRL at Brookhaven National Lab in New York. These data sets provide a useful base of information for assessing the effectiveness of identification routines. Data has been taken with several instruments, at various incidence angles, and with various DAC settings. A summary of ions and energies is presented in Table 6.1.

The data is of the same format as that taken on orbit and processed using the same calibration and data formatting as previously described. A naming convention has been adopted for use in processing and analysis of the accelerator data sets. See Appendix B for details on the naming convention.

6.2 ROOT framework

This work has utilized the ROOT packages extensively and some discussion of this decision is warranted. ROOT provides an open-source and operating system independent basis for creating a data analysis environment. The data structures implemented within ROOT have been built to allow flexibility in application with a focus on high energy physics data. The ROOT data file format also has the benefit of incorporating compression algorithms and data table redundancy to provide a measure of resilience against data corruption and loss.The ROOT package is freely available from CERN and contains an extensive set of documentation and examples. [118, 119]

Table 6.1: Ion Species and Energy for Data Taken Using Timepix Devices

Nuclide	Energy [MeV/nuc]	Facility
^{1}H	7	NSRL
	5	NSRL
	10	NSRL
	25	NSRL
	50	NSRL
	100	HIMAC
	200	NSRL
	1000	NSRL
^{4}He	100	HIMAC
	180	HIMAC
	230	HIMAC
^{12}C	100	HIMAC
	230	HIMAC
^{14}N	180	HIMAC
	290	HIMAC
^{16}O	100	HIMAC
	230	HIMAC
^{20}Ne	180	HIMAC
	430	HIMAC
	600	HIMAC
^{28}Si	400	HIMAC, NSRL
	600	HIMAC, NSRL
	800	HIMAC
^{56}Fe	105	NSRL
	200	NSRL
	300	NSRL
	500	HIMAC

The general approach taken throughout this project has been to consolidate data formats in order to allow the broadest access to the data possible. The guiding tenant behind this has been that all which should be required to view and perform additional analysis on the Timepix data is a computer with the ROOT framework installed and the data itself. This goal has been realized primarily through utilization of a standardized internal data structure for different levels of data processing.

Timepix device raw data is recorded in an [x,c] format, meaning the pixel number 'x' (ranging from 0 to 65535) and TOT count 'c' for the associated pixel are stored in binary or ASCII format for each frame of data. This is a function of the Pixelman software used to control the data acquisition, and Pixelman also generates a set of metadata corresponding to each frame of data recorded. [117].

The raw data is calibrated and processed into a Level 1 data format containing both the raw and calibrated data, along with the metadata from data acquisition and a set of basic cluster identification data for each data frame. The Level 1 data is stored in a ROOT TTree format within a ROOT TFile data structure. [118, 119]

Level 2 data consists of a similar TTree and TFile formatting scheme, but separates the data by pixel cluster, while retaining frame reconstruction information. The separation of data into a cluster based format is required to allow filtering and analysis at the individual track level, as opposed to the data frame level used in the Level 1 data. The Level 2 processing also includes

additional cluster analysis information.

Level 3 data contains basic ion charge and β identification parameters, and is essentially an extension of the Level 2 data focused on adding or retaining information necessary to perform identification of ion charge and velocity.

6.2.1 PROOF and parallel processing

An additional benefit of the ROOT package is the inclusion of PROOF, which is a package for parallelization of ROOT based data analysis routines. [120] Due to the processing requirements necessary for isolation of electron and stopping ion clusters, the processing algorithms used to generate Level 3 data are performed within the PROOF framework. This allows the processing of individual clusters to be run independently and this processing can be done on high performance computing systems which provides the benefit of using a large number of computer processors to analyze many pixel clusters at the same time.

6.3 Analysis Tools

Over the course of this project, several analysis tools have been developed to provide visualization of the data and to create environments in which to develop, test, and validate algorithms used in the data processing.

6.3.1 Radiation Environment Monitor Analysis Software

The ISS Radiation Environment Monitor project required a visualization tool to allow pixel maps and plots of dose and dose equivalent versus time to be created. This bulk of this tool was built by Dr. Son Hoang using elements of the ROOT package for plotting and display. This software is capable of reading in multiple Level 1 data files and displaying individual frames of data with energy calibration applied.

The REM analysis software integrates several other features as well which can be used to investigate the Timepix data and applied analysis routines. Several software tabs exists to allow the user to select the data features for viewing, including LET spectrum, vehicle trajectory versus dose rate plots (dose maps), and cluster visualization to show the user how pattern recognition aspects are applied to a cluster. The dose maps also allow the user to view the frame generating a point in the dose map as selected by the user along the trajectory.

In addition to these visualization and investigation tools, the ISS REM analysis software integrates the data conversion capability to process raw data files into Level 1 format data files. Typically the conversion is done separately, and the REM analysis software is used as an investigation tool. However, with the conversion routine included, it allows the user to take a raw data set and calibration information and generate Level 1 data files directly.

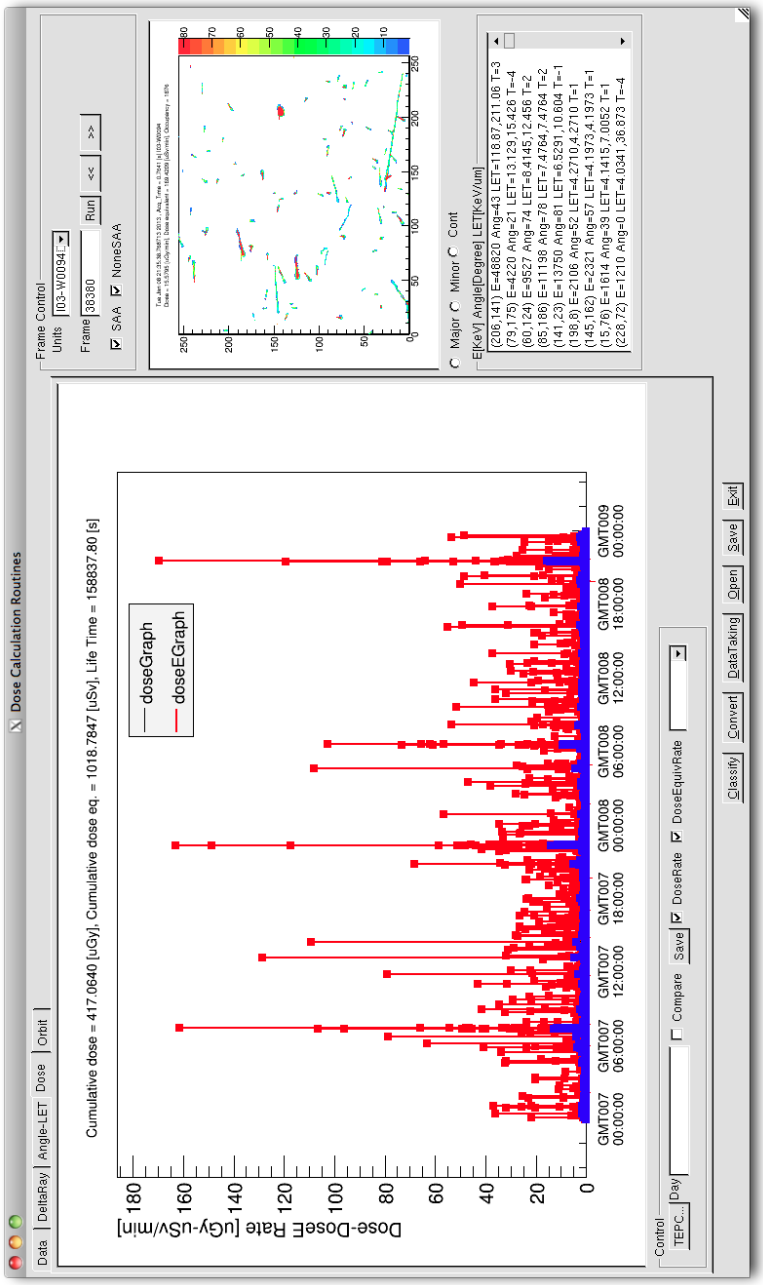

Figure 6.2: A screen capture of the REM analysis software showing the dose rate versus time plot. The data frame on the right was displayed by selecting the highest dose equivalent rate point on the right of the primary plot.

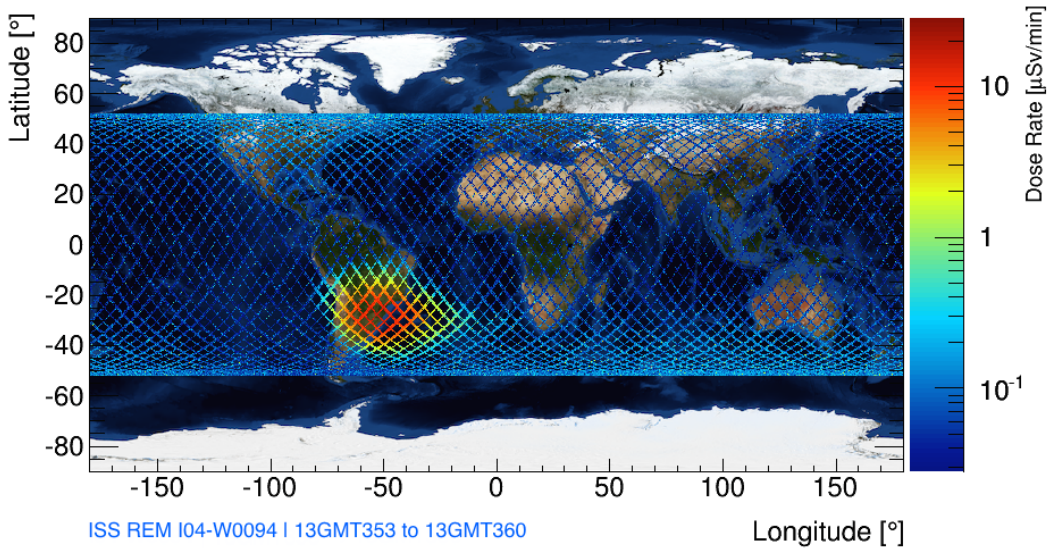

Figure 6.3: Dose rate map showing the dose rate at locations along the ISS trajectory over the course of one week. The ISS has an inclination of 51.6° and completes a single orbit in approximately 90 minutes.

6.3.2 Determination of Orbital Elements

The conversion software, both stand alone and integrated into the REM analysis software, utilizes a wrapper for the Simplified General Perturbation 4 (SGP4) orbital elements generator and related software to determine latitude, longitude, and altitude to be associated with any given frame. The wrapper takes in a Two Line Element (TLE) trajectory set as well as a time associated with the frame. The wrapper then calls the related trajectory conversion algorithms [121, 122] and returns the latitude, longitude, and altitude for the specified time and TLE.

The use of the SGP4 routines is required since these routines were utilized to generate the publicly available TLE data sets. The SGP4 documentation warns that utilizing different routines to encode and decode the orbital information will result in errors, and this is due to the equations and parameterizations made during encoding ephemeris into the TLE data sets. The TLE information for the International Space Station, where the REM units are deployed, is obtained from NASA's Human Space Flight Orbital Elements website or from the Celestrak website. [121, 123, 124]

6.3.3 Pattern Recognition Algorithms

The pattern recognition algorithms have been described in detail within previous works [77, 125–127] but will be reviewed briefly in this section.

The primary pattern recognition algorithms used are those found in the

BlobFinder class (and associated classes required for its function) within the Level 1 processing codes. The BlobFinder class is utilized again during Level 2 processing to provide a method for isolating clusters from one another. When combined with TOT or energy threshold cuts applied to pixel data, the BlobFinder class allows portions of the cluster to be separated as well.

The primary mechanism in the cluster isolation is the use of a bit mask for comparison of the current pixel contents to the surrounding pixels. [128, 129] The nearest neighbor pixels are those pixels to the top, bottom, left, and right, of the current pixel. The next-nearest neighbors are those pixels to the upper left, upper right, bottom right, and bottom left of the current pixel. The bit mask is a pattern of zero or non-zero values for these 8 nearest and next-nearest neighbor pixels. Selecting the pattern to use allows filtering processes at the pixel level based on the surrounding pixels as the mask is applied to each pixel.

Using the mask with non-zero nearest neighbor pixels, the determination can be made if a given pixel is an inner pixel (the nearest neighbors are non-zero valued) or a border pixel (at least one nearest neighbor pixel contains a zero value). A cluster is defined by the closed boundary formed by its border pixels. [128, 129]

There are two angles of interest for each cluster. The first is the in-plane angle of the cluster within the pixel grid. The second is the angle of travel through the sensor volume relative to the vector normal to the sensor surface. The pattern recognition algorithms utilize a weighted least square fit method

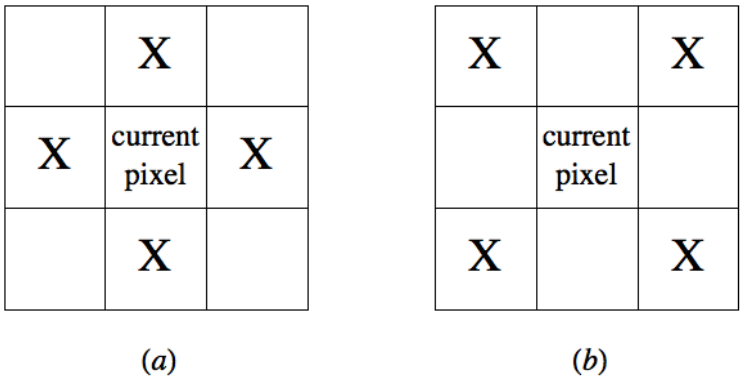

Figure 6.4: The nearest neighbor (a) and next nearest neighbor (b) masks are shown as they apply to boundary identification. If the nearest neighbor pixels are nonzero for a nonzero target pixel, then the target pixel is labeled as an inner pixel. Otherwise it is labeled as a border pixel.

to find the former with pixel energy as the weighting parameter. [77]

The angle through the sensor volume, which we refer to here as the dip angle, is determined utilizing the energy-weighted cluster profile in both the horizontal and vertical direction along with fuzzy logic operations to apply a membership weight. The fuzzy logic operations are used to separate the track core from the low energy penumbra or 'skirt' surrounding the higher energy core pixels. The result is a set of parameters which are used with the sensor thickness to determine the dip angle of the track. [77, 128]

6.3.4 InCA: An Analysis Sandbox Toolset

The Individual Cluster Analysis (InCA) codes are a testing and sandbox environment tool set built during the course of this dissertation work. The code arose from the need to visually assess the pixel patterns of a given cluster

and assess how those patterns related to the results of the various analysis algorithms. This code set has been used extensively to verify algorithm operation and investigate unexpected features in the data as such features were found.

In addition, the InCA code provides a 'sandbox' environment where an analysis algorithm can be built and investigated before being integrated into the full analysis tool-chain. InCA was designed to use the Level 2 data as input. Replicating processing calculations, or in some cases simply porting the computational methods from the processing code to the InCA code set, allows visual inspection and comparison of the results to calculations performed during processing of Level 1 data into Level 2 data.

The ROOT Graphical User Interface (GUI) classes were used to build the InCA GUI. This interface allows input file selection and data browsing. In addition, event selection criteria can be used to filter the data being viewed. For instance, if the user wished to examine only pixel clusters with an associated LET greater than a given value, the LET selection criteria can be entered into the GUI and the resulting data will be restricted to only clusters meeting the selection criteria.

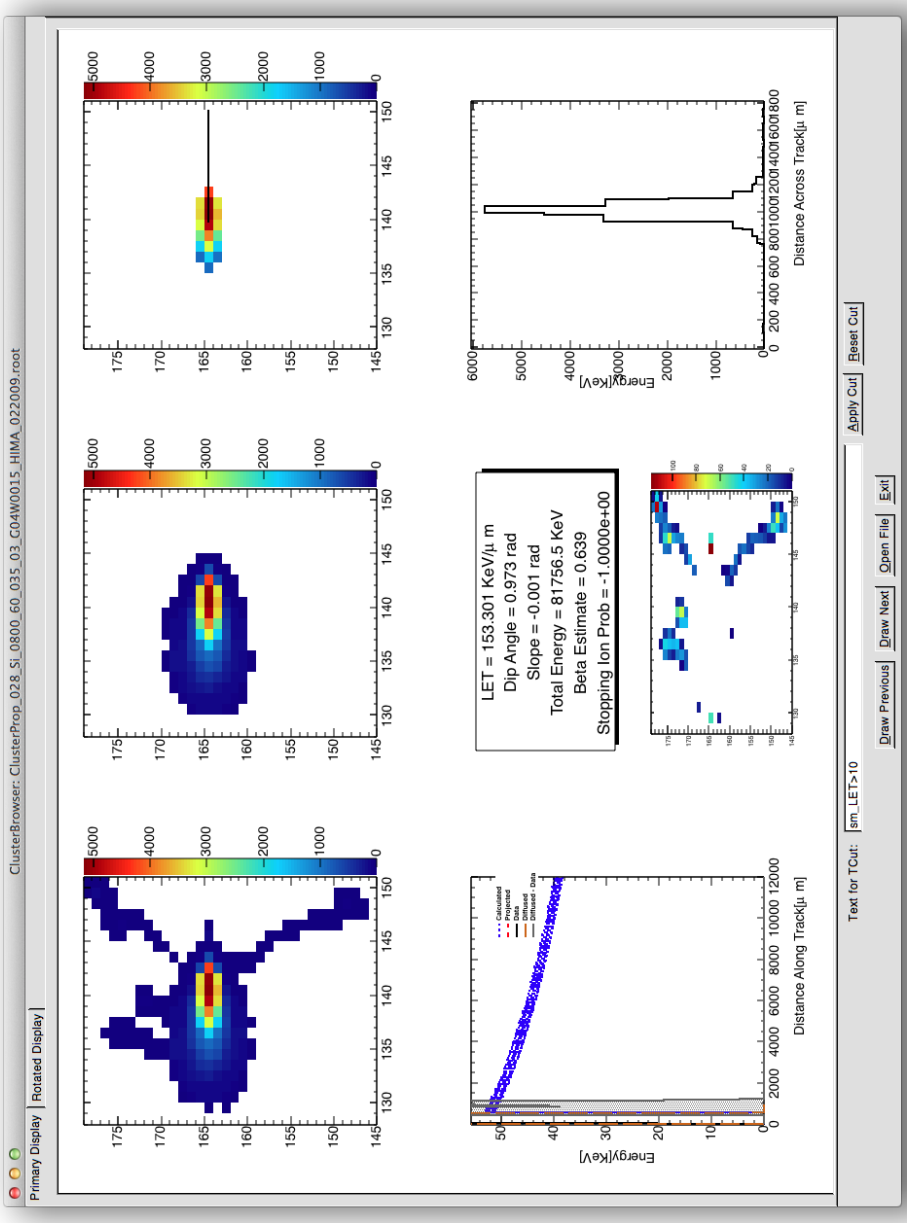

Figure 6.5: The primary tab display for the ClusterDrawGUI interface is shown. This display contains the cluster pixel map (x and y grid with color coded energy in KeV) as well as various displays to investigate calculation results and algorithm performance.

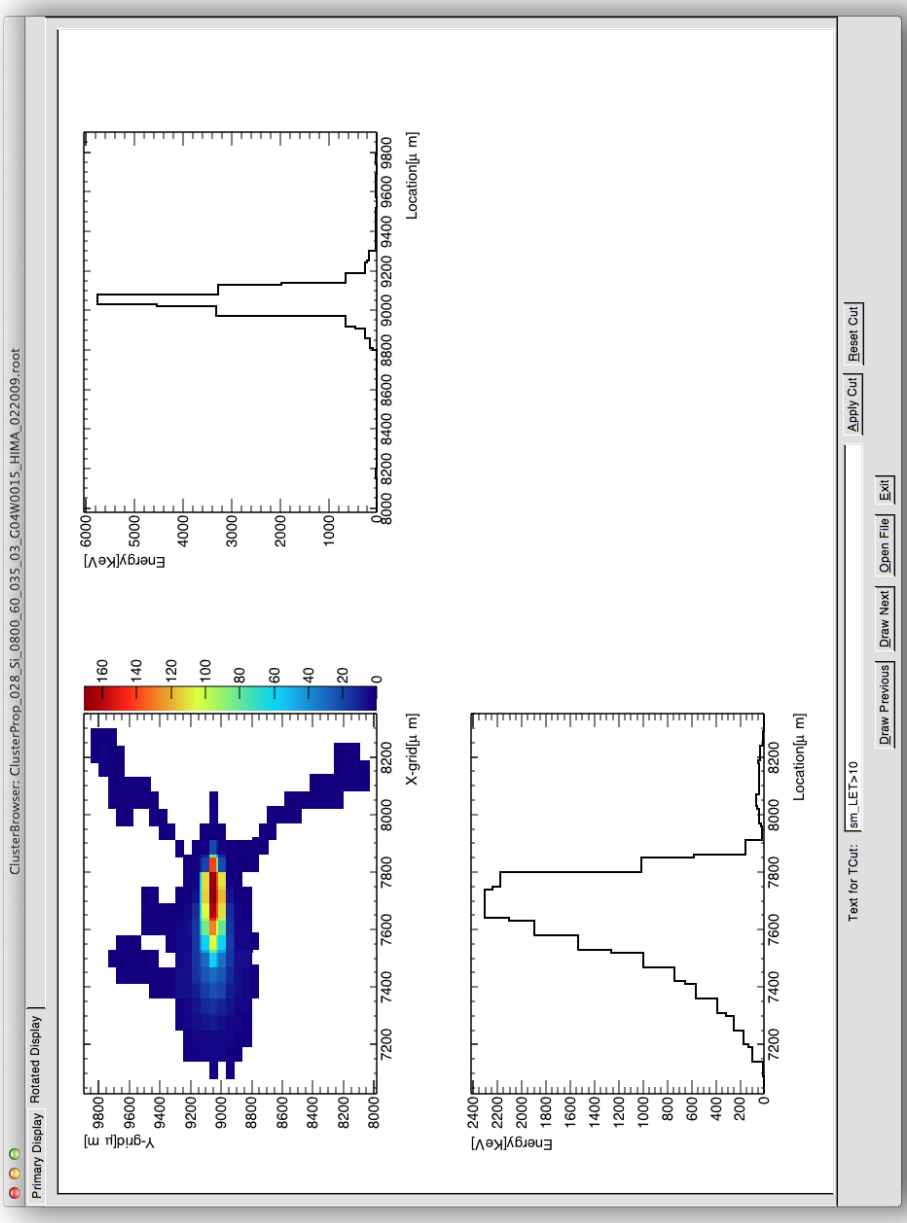

Figure 6.6: The secondary tab display for the ClusterDrawGUI interface is shown. This display shows the cluster map (x and y grid with color coded energy in KeV) after it has been subdivided and rotated, along with the projections on the x and y axis.

Chapter 7

Identification of Ion Charge and Velocity

7.1 Overview

The method currently applied toward identifying individual charge and velocity has several components. The first step is to identify electron tracks. Electron tracks are present in nearly all data taken with the Timepix detectors, and these are either the incident particle under measurement or, more often, produced through interactions with surrounding material or through interactions with the sensor. Such tracks have morphological features which allow them to be identified and labeled as electron tracks.

The next step in the process is to identify stopping ion tracks. This is done by making the assumption that the track is a stopping ion track and

comparing the energy and calculated stopping curves with those contained in the Timepix data. If the data and the calculations resulting from the stopping ion assumption are a good fit with one another, then the track is labeled as a stopping ion.

Once electrons and stopping ions are identified, the remaining tracks are either of interest for identification, or are tracks with overlaps and/or the result of nuclear interactions near or within the sensor. An attempt is made to identify overlapping or interaction tracks, and these are labeled as well. The labeled clusters are then filtered and the identification algorithms are performed on the remaining tracks.

7.2 Electron Identification

Separation of electron tracks within the Timepix data frames is necessary for both accelerator and on-orbit data to allow segregation of low energy electron, proton (along with high energy electron), from heavier ion tracks. Low energy electron tracks are characterized by small energy deposition values along the track (relative to heavier ion core depositions), thin track morphology (one or two pixels in width), and exhibiting the characteristic meandering-path resulting from multiple scattering within the detector material. [15, 130, 131]

7.2.1 Method

The initial approach of electron track separation is to identify clusters which have all, or very nearly all, pixels labeled as border pixels using edge identification algorithms. This will limit the clusters identified for additional analysis to those which are very thin - the expectation is the low energy deposition from electrons, protons, and other light particles will extend across 2 or possibly 3 pixels in width across a section of the track, however only electrons are expected to exhibit significant track curvature.

The Pixel class within the BlobFinder.cpp code [77] contains the Blob:: isInnerPixel() function, which compares the surrounding pixels of the current pixel of interest with an 8 element bitset of $01010101b$, equal to 85 in decimal, corresponding to non-zero TOT values (or energy if calibration is applied) in pixels to the left, top, right, and bottom of the current pixel. The pixels surrounding the pixel under analysis, that is to say the values of the 8 neighbor surrounding pixels, is compared to this inner-pixel expectation bit mask, and the boolean value is returned true if the top, bottom, left, and right neighbor pixels are non-zero. In this way, a pixel within a cluster is labeled as an inner pixel.

The inner-pixel labeling can be used to determine how many pixels are on the border of a cluster, which in turn, can then be compared to the total number of pixels in the cluster to find the ratio of border pixels to total pixels. If all pixels are border pixels, the track is very likely a light ion (proton,

electron, muon, etc.) track since this indicates a width of no more than two to three pixels, depending on the angle of the track pattern relative to the pixel grid. The fraction of border to total pixels is set as a value in the Level2 processing data (per-cluster data) as "sm_borderFraction". Combined with a curvature estimate, this can be used to filter out curved lower energy electron tracks while retaining proton and high energy electron tracks.

Once such clusters are identified, there are two separate branches of analysis that may be followed. First, assuming the cluster is separate from other clusters (i.e. not connected to a larger cluster), the slope of the line in the plane of the detector surface can be determined relative to the pixel grid utilizing functions defined in the BlobFinder code set. The cluster is then rotated and translated so that this line is parallel with the x-axis and the the cluster center of gravity is located at the origin.

An estimate for curvature is calculated for the cluster using a variant of the method proposed by Opalka (Opalka et al., 2013) to determine 'straightness' of a pixel cluster. [132]. With the described rotation and translation completed, slices of the cluster perpendicular to the x-axis are used to find a local weighted mean in energy distribution across the subsection of the cluster at that x coordinate. The maximum deviation of the mean along the full track is then used as a measure of track curvature.

The second branch of the analysis uses a slope fit line in the same manner as the previous method, but applied after performing additional steps for separation of both the track from a parent cluster and the slope angle relative

to the trajectory of the parent. The slope angle relative to the parent track trajectory allows identification of the ejection angle of the electron and the previous analysis branch can be used to allow an estimate of the deviation from this straight line which may help to separate delta-ray sub-clusters from those related to interactions or fragmentation processes. The relative angle analysis, however, requires an additional step of separating of the sub-cluster from the primary (parent) pixel set.

An alternative approach to the problem of identifying lines or arbitrary predefined curves is the use of a Hough Transformation as described by Duda, and modified for real-time implementation by Fernandes et al. [133,134] Initial investigation into this method indicates it may be quite useful and more tolerant of gaps between line segments, but it incurs a rather sizable computational burden, even with the efficiency introduced by Fernandes, and so has been left for a future effort.

7.2.2 Results and Effectiveness of Filtering

Computational load issues have prevented the execution of the full analysis codes using PROOF for parallelization during migration of the code to the NASA computing cluster, and only the border fraction approach is currently applied to the HIMAC data sets. The analysis of on-orbit data will require the additional algorithms described above, but the border fraction algorithm is well suited to isolating heavy ion tracks in accelerator data sets and serves

to reduce the number of clusters passed on to the heavy ion algorithms.

7.3 Stopping Ion Identification

Particle identification in a thin detector can be separated into two primary tasks: identification of ions passing through the sensor and identification of ions stopping in the sensor. The general goal of this dissertation deals with heavy ions, and as a result focuses on the former component. However, the task of filtering stopping ions was found to be necessary. This section focuses on the latter of these identification tasks for stopping ions.

The identification of stopping ions in a thin sensor layer is also applicable beyond the Timepix detector. Non-pixel, thin silicon detectors may not have sufficient resolution to identify stopping ion signals directly. The associated analysis for such instruments utilizes an average path length through the detector volume to generate Linear Energy Transfer (LET) spectra without isolating stopping ions. As a result, stopping ion LET is underestimated and the energy deposition from ions stopping in the detector may artificially inflate the (assumed) penetrating LET spectrum when using average chord in calculate LET calculations. [135,136] Utilizing Timepix data corresponding to similar time periods may allow deconvolution of stopping and penetrating ion LET spectra for other instrumentation.

7.3.1 Background

Minimum ionizing carbon has an Linear Energy Transfer peak in silicon near 14 KeV/μm and has been shown to be present in the GCR component of the LEO radiation field [137]. Carbon is expected be present at the same, or lower, fluences within the trapped components of the LEO radiation field due to the penetration of the GCR ions into the Van Allen Belts, however a fluence of minimum ionizing carbon higher than that present in the GCR component of the LEO radiation field is not expected to be localized in the South Atlantic Anomaly (SAA).

During the initial data analysis on the International Space Station Radiation Environment Monitor (ISS REM) data sets, a peak in the calculated LET spectra was noted near 14 KeV/μm, similar to that expected from GCR carbon. Separation of the data into trapped and Galactic Cosmic Ray components based on orbital location of the ISS resulted in visible peaks in the LET spectrum that differed in magnitude, with the trapped component unexpectedly higher than that of the GCR component.

Data taken at the NASA Space Radiation Laboratory beam line using Timepix assemblies and proton beams moderated to energies between 5MeV and 50MeV exhibited similar data features as those seen in the on-orbit data. While ground based measurements were insufficient to cover the full range of incidence angles seen in on-orbit data, the analysis of the NSRL runs shows that stopping ions contribute to the observed features.

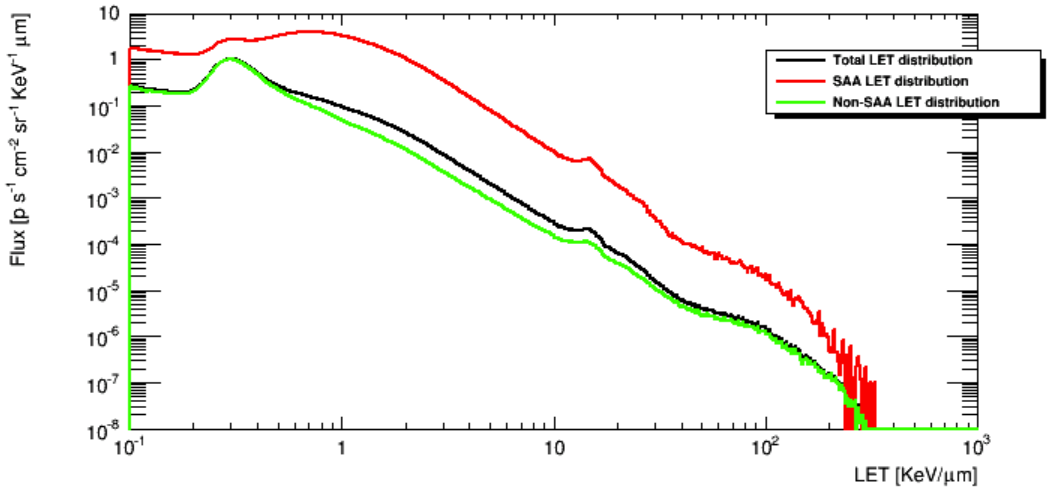

Figure 7.1: The LET flux shown is for ISS REM I04-W0094 and has been divided into SAA and non-SAA components. Note that the flux for the peak near 14 KeV per micron is higher in the SAA component of the LET spectrum.

7.3.2 Method

The stopping ion identification task has been divided into two subtasks. The first is the identification of features in the bulk data that can be associated with stopping protons. The second task is the track-by-track identification of stopping ions.

Bulk Data Feature Characterization

The features noted in the on-orbit data were indicative of stopping protons, as shown in the data taken at NSRL, but the effects of stopping protons on the LET spectrum were not well understood for the Timepix detector assemblies. The approach was then to create a simulation of what the effect would be for a

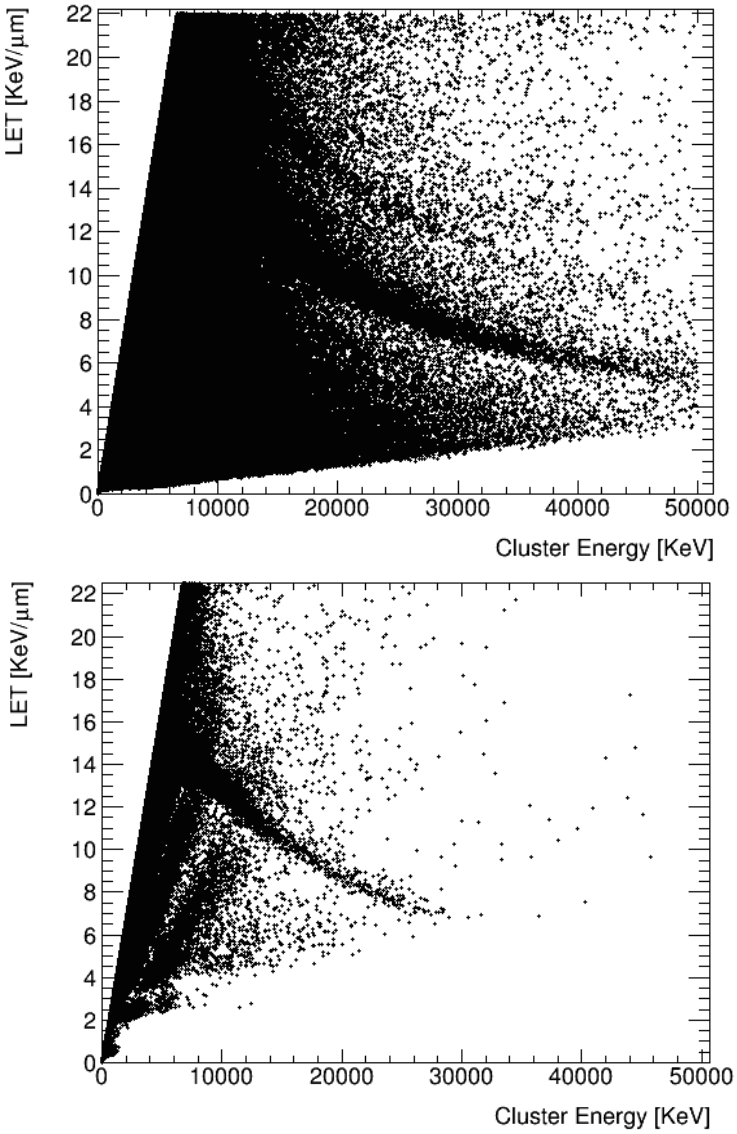

Figure 7.2: Comparison of on-orbit data (left) and data taken at NSRL for protons with energies of 5, 7, 10, 25, and 50 MeV (right) shows similar data features in the two data sets. Energies below 25 MeV in the NSRL data contribute to the features between roughly 5 and 15 KeV per micron.

range of proton energies and incidence angles on the LET spectrum generated by the Timepix device.

Using stopping and range tables generated by SRIM [138], algorithms were developed to simulate the energy loss profiles for incident ions, initially protons. The simulation scans through a range of energies and angles of incidence for the ions, interpolating the stopping powers and ranges based on the number of steps defined for the ion transit in order to map incident ion energy and angle into LET and energy lost in silicon.

If the projected CSDA range of the ion is larger than the projected path length through the silicon, the ion is assumed to fully penetrate the sensor layer, and the energy loss while the ion is traversing the sensor is tabulated for the track. However, if the projected range of the ion is shorter than the projected path length, the assumption is made that the ion deposits all its energy in the silicon sensor, an energy loss profile is not generated, and the LET is calculated in the same manner it would be for the ISS REM data.

The ISS REM LET calculation assumes the ion penetrates fully even in cases where that assumption is invalid, and so stopping ions are not properly handled in the ISS REM calculations. The simulation replicates this invalid assumption by finding the projection of the track path onto the back plane of the Timepix detector. This projected length, analogous to the length of the ion track's pixel pattern in the data, is then used with the assumption of full ion penetration to find the LET as calculated by the ISS REM algorithms.

Longitudinal ion straggling is incorporated in an effort to better replicate

the features seen in the data. Since this is not a true Monte Carlo simulation, the effect is of minimal use, but it does widen the simulated feature slightly and allow it to be seen more clearly in data plots. Inclusion also shows the straggling has minimal impact on the simulation results, aside from the noted widening effect.

The inclusion of longitudinal straggling is handled by using the estimate of longitudinal straggling provided by SRIM for the ion and energy of interest as an upper limit and using a normalized random number to vary the straggling applied to each stopping ion from zero to the SRIM defined upper limit. The applied straggling is then included in the total path length when calculating LET.

The simulation results are collected into ROOT histograms of LET, LET versus Energy Loss, and LET vs Ion Energy. LET plots are further separated into total, stopping, and penetrating components. Results are discussed in the section 7.3.3.

Individual Track Identification

Individual stopping ion identification must be handled on a track-by-track basis. It has been shown previously that the pixelated Timepix data can provide energy loss curves for ions. [139, 140] Utilizing this, the assumption is made that an ion track is a stopping ion track. Under this assumption, with the total cluster energy as the stopping ion's incident energy, the track is compared to an energy loss curve for ions of the same energy generated using

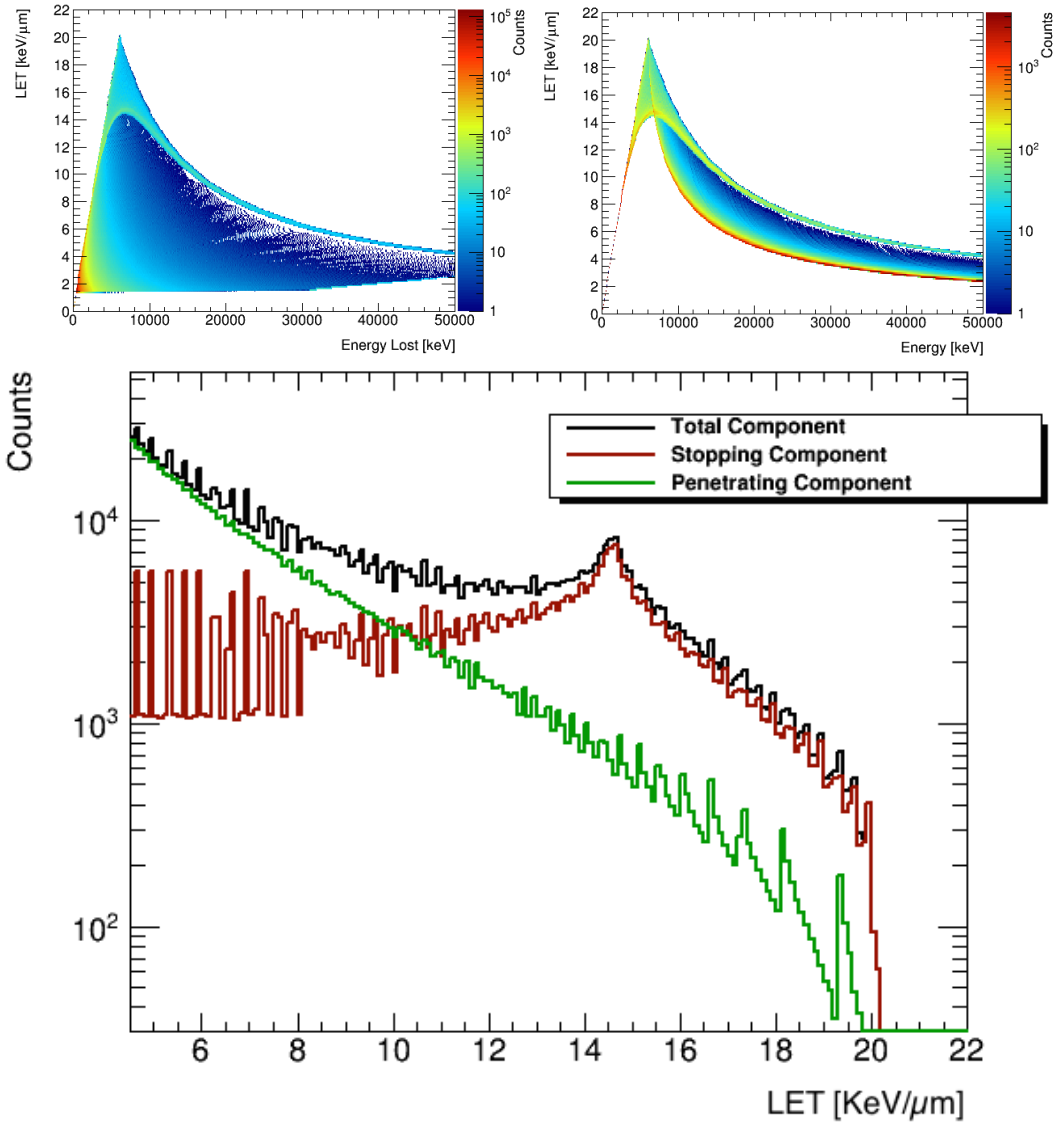

Figure 7.3: Simulation results for protons between 10keV and 10GeV at angles between 0 and 90 degrees incidence. The triangular region in the top two plots is due to ions stopping in the detector.

SRIM data tables for the appropriate particle species.

Drift and diffusion effects are incorporated into the calculated stopping ion energy loss curves to allow better fit to data curves. The drift and diffusion effects are applied by using a Gaussian distribution centered at each individual histogram bin in the energy loss curve. The total energy in the bin is spread across adjacent bins, and the spread algorithm is applied to all bins in the calculated energy loss curve to generate a new histogram with drift and diffusion effects incorporated.

Directionality of ion travel and curve alignment must also be addressed. The peak of the energy loss curve is found in each case and the calculated histograms is flipped so that the peak values of each curve are on the same side of the associated histograms. This is done to ensure the directionality is the same for both energy loss curves (i.e. that the Bragg peak is located at the same end for both curves).

Curve alignment presented some difficultly in achieving sufficient alignment of the curves. Initially, the peaks of the two curves were aligned in an attempt to avoid curve offsets which would introduce unnecessary errors into the goodness-of-fit comparisons. This approach proved to be inadequate during a visual comparison of the curve alignment. This is not unexpected and is a result of the Poisson nature of the energy loss processes. [15, 43, 44]

Instead of alignment of the energy loss peaks between the two histograms, the approach of maximizing the goodness-of-fit between the two curves was utilized. This proved to be much more effective at aligning the histograms for

comparison. Chi-squared and Kolmogorov goodness-of-fit tests were investigated for this purpose. The Kolmogorov test, which is more sensitive to the distribution shape than the chi-squared test, was chosen as the test of choice to apply in this case. [141]

The Kolmogorov goodness-of-fit test is already implemented in the ROOT code set, and was utilized without modification to return a probability of fit value. [119] The returned probability is used for comparison to a threshold value to make the determination of whether or not the stopping assumption is valid for the track under analysis.

Goodness-of-fit checks are applied to data and to stopping ion energy loss curves for several ions. The above best-fit maximization algorithm is applied using energy loss curves calculated for protons, deuterons, tritons, Helium-3, and Helium-4, and the best fit probability is retained from among these ions.[1] A determination is made whether or not the stopping ion assumption is appropriate using this information. If so, and the fit probability exceeds the threshold, the track is flagged as a stopping ion track and the ion energy, charge, and mass for the best fit curve are recorded.

7.3.3 Results and Discussion

The results are divided into two sections. The first deals with identification of the features of the bulk ISS REM data, while the second covers the results of track-by-track identification.

[1]Hydrogen isotope data were obtained from the IAEA Isotope Browser [142].

Bulk Data Feature Characterization

The comparison of simulation results to ISS REM data show that the features reproduced by the simulation, which result from the manner in which the ISS REM algorithms calculate LET, correlate very well with features seen in the on-orbit data. Simulations have been run using proton, deuterium, and tritium stopping power and range data, and the results show that the secondary data features also correlate well with the hydrogen isotopes.

It is interesting to note that modification of the projected range (which affects projected length of the track on the back-plane of the detector) in the simulation by a factor of 0.85 produces a better fit with data for protons, but not for deuterium. This could be due to a number of possible reasons in the ISS REM data, such as errors in the energy calibration, impacts from saturation effect on the calibration, and issues in angle identification for calculating path length in the data. However, since the correction factor is not consistent across all detector units, this suggests that additional investigation is required into variations in, and accuracy of, unit calibration.

Dopant concentrations of boron were added to the silicon target makeup in generating the SRIM stopping tables, and used as input into the simulation in order to investigate if the range modification could be related to dopant concentrations, however no significant impacts to the simulation results were found when adding boron doping between 0.01% and 5%.

It is possible that the saturation effects which impact conversion of pixel

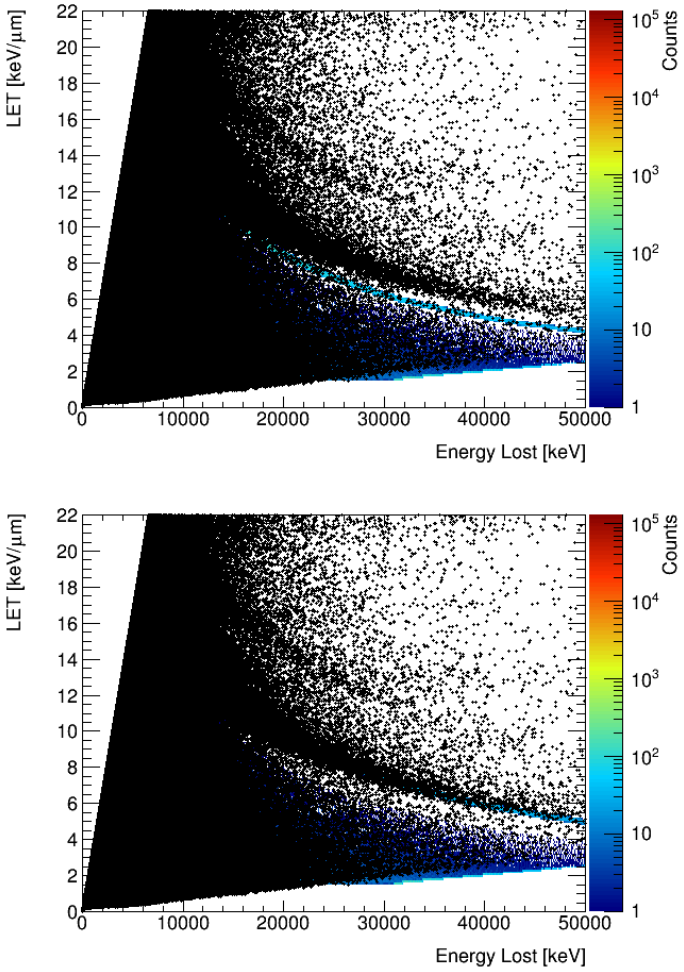

Figure 7.4: Simulation results for proton energy loss overlayed with ISS REM data from unit I04-W0094 in 2013 (first 175 days). The top image shows the simulation with no correction to the stopping ion range. The bottom image shows simulation results with stopping ion range reduced by a factor of 0.85 during calculation of the pathlength for LET.

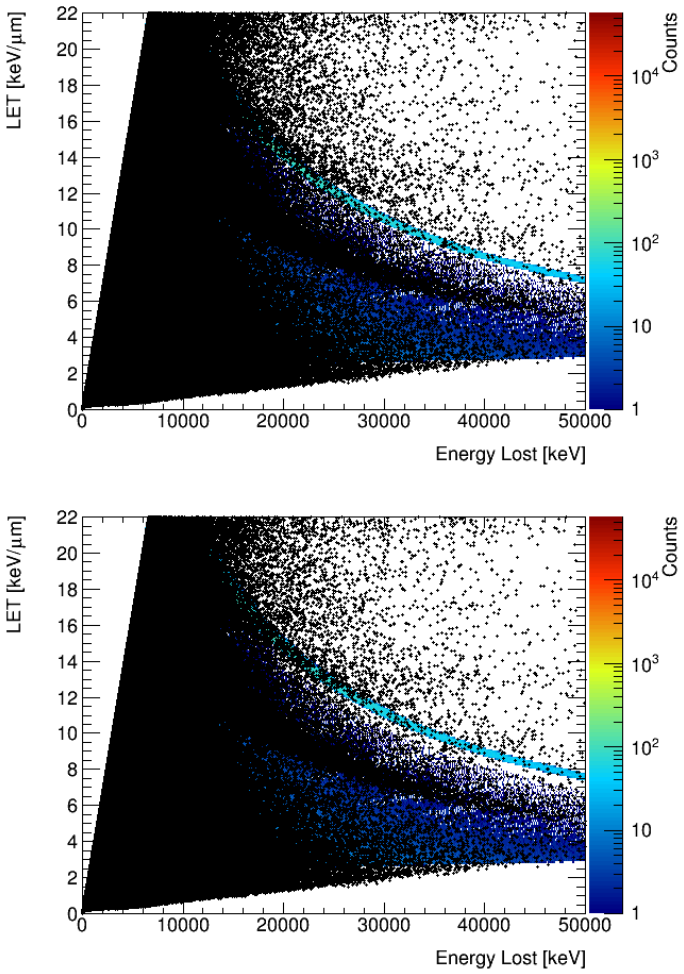

Figure 7.5: Simulation results for deuterium energy loss overlayed with ISS REM data from unit I04-W0094 in 2013 (first 175 days). The top image shows the simulation with no correction to the stopping ion range. The bottom image shows simulation results with stopping ion range reduced by a factor of 0.95 during calculation of the path length for LET.

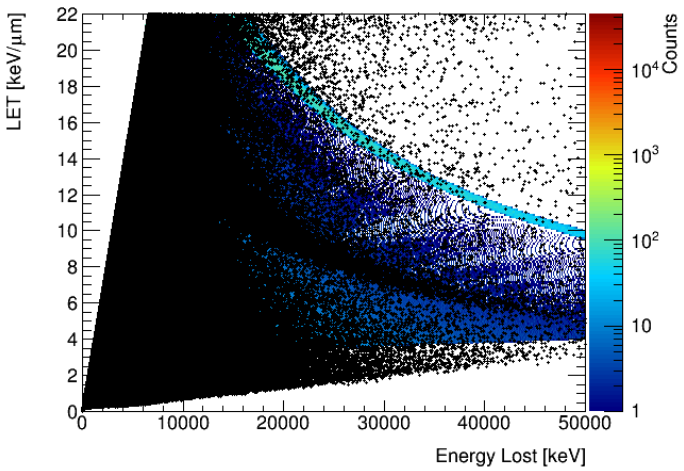

Figure 7.6: Simulation results of tritium energy loss overlayed with ISS REM data from unit I04-W0094 in 2013 (first 175 days). The image shows the simulation with no correction to the stopping ion range.

TOT counts to energy are affecting the LET calculations preferentially for stopping ions due to the large localized energy deposition associated with the Bragg curve. This has been discussed internally within our research group, and additional investigation into correction of saturation effects is ongoing.

Individual Track Identification

Results related to the per-track ion identification are satisfactory, though further work is possible to refine the fit methods and optimize the maximization process. The process is currently quite computationally intensive and has required parallelization of the code using PROOF in order to utilize the high performance computing cluster maintained by the Space Radiation Analysis Group at NASA Johnson Space Center. [120]

Application of the individual track identification allows the majority of the peak at 14 KeV/μm to be removed by filtering out the individual tracks identified as stopping ions. Using stopping power and range tables generated from SRIM for only protons requires setting the stopping ion probability threshold quite low in order to affect the 14 KeV/μm peak. Addition of SRIM tables for the hydrogen isotopes is expected to allow the probability threshold setting to be increased, in turn decreasing misidentification rates.

Inspection of the data relative to the calculated stopping curves has also revealed that clusters with a small number of pixels (roughly 10 or less) have a greater misidentification rate. This is not unexpected since the Kolmogorov Test algorithm implemented in ROOT is known to have poor performance in situations where the number of bins in a histogram is low. [119]

7.4 Interaction and Track Overlap Filtering

Tracks which overlap, or are a result of fragmentation or other interactions in the silicon detector layer or surrounding materials, affect the identification process. Such tracks often have very high energy depositions associated with them and contribute to the high-LET portion of the spectrum. Interactions may be useful in identifying the incident particle, though for the current effort, these have been excluded.

A threshold is applied to a cluster, removing pixels with energy values below one tenth of the maximum value. The cluster isolation algorithm is

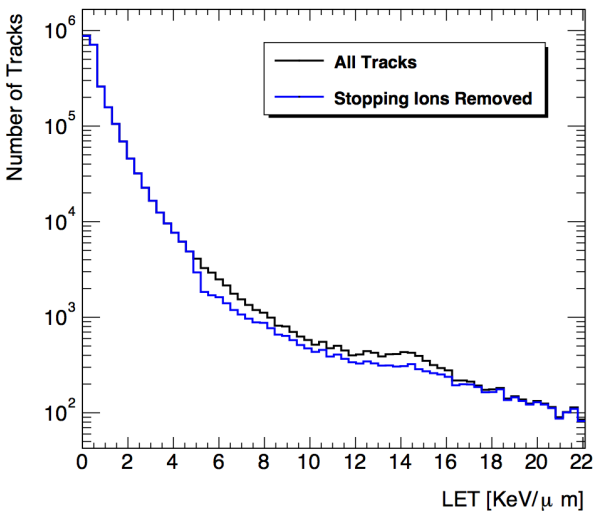

Figure 7.7: LET spectrum for a single unit over the course of six days with and without the stopping ion track filter applied. The filter used to generate this plot uses only proton stopping tables, so the probability threshold is set quite low. Updates in work to update the filter algorithm to include stopping tables for isotopes through ^{4}He

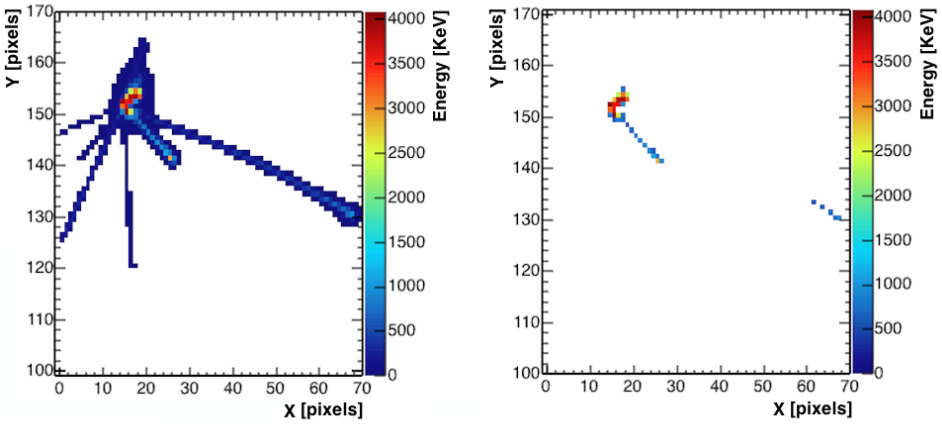

Figure 7.8: An interacting track (left) can be identified in many cases by applying a threshold to the cluster to remove the low energy pixels and reapplying the cluster isolation algorithms (right). Clusters with multiple well-separated peaks can be identified in this way.

then run on the reduced cluster. The threshold is chosen such that contains the 'skirt' of the pixel while remaining low enough that it does not remove secondary peaks in cluster energy. if these peaks are sufficiently separated, as in the case of a core track and stopping secondary track emanating from it, the cluster isolation algorithm will identify multiple sub-clusters. In this manner, larger interactions can be found and tagged.

This method is sensitive to the maximum energy in the cluster and is less effective for clusters of lower energy. Additionally, it relies on the assumption that the fragments will slow significantly or stop in the detector, resulting in an increase in energy loss along the fragment track. While the method does work in many cases, visual inspection of plots similar to those in figure 7.8

indicates such an assumption is generally invalid and a more reliable method for interaction isolation based on track morphology would be better suited to this application.

7.5 Energy Loss Profile

At this point we take a moment before moving on to heavy ion identification methods to describe the process used for all clusters to generate an energy loss profile. This process, or portions of it, is applied to nearly all clusters in the analysis, and so the process is worth reviewing in detail.

To calculate the energy loss profile, the first step is to find the center of gravity for the cluster. Looping over the pixel array, we find the center of gravity location using the energy weights in each pixel i.

$$CG_x = \frac{\sum_i x_i E_i}{\sum_i E_i} \tag{7.1}$$

$$CG_y = \frac{\sum_i y_i E_i}{\sum_i E_i} \tag{7.2}$$

Each pixel in the cluster is then subdivided into an 11x11 grid. The energy is assumed to be equally distributed across the entire original pixel, so each sub-pixel contains an equal fraction of the original pixel energy. This is done in an attempt to retain the spatial distribution of the cluster energy during the subsequent rotation process.

Ideally the energy surface for the pixel would be described by the values

at the boundary of adjacent pixels, and this would be used to increase the accuracy of energy distribution across the cluster, but this approach has not yet been implemented or tested and remains as forward work.

In order to facilitate several of the calculations used in the analysis codes, the subdivided cluster is translated prior to rotation so the center of gravity is coincident with the grid origin. The slope of the cluster in the plane of the sensor surface and relative to the pixel grid axes is identified by the pattern recognition algorithms during cluster separation. (Note that the slope is a ratio of lengths for the cluster and not an angle.) This slope is used to rotate the subdivided cluster so the direction of travel of the ion is oriented along the x-axis using a rotation transformation after calculating the rotation angle from the slope:

$$\theta = \arctan(slope) \tag{7.3}$$

$$x' = xcos\theta + ysin\theta \tag{7.4}$$

$$y' = ycos\theta - xsin\theta \tag{7.5}$$

The cluster profile is generated by projecting the two dimensional cluster onto the x-axis. The energy is summed for each increment along the x-axis, providing a total energy per unit of travel distance. This can also be performed relative to the y-axis to get the energy profile perpendicular to the direction of travel. Because the charge carrier spread is assumed to be symmetric in the

plane of the detector surface, the forward diffusion and backward diffusion from subsequent ionization sites along the path of the track compensate each other. A similar method used to generate proton profiles was shown to reproduce the ionization loss curves for protons generated by SRIM. [34, 138, 139]

7.6 Heavy Ion Identification

The sections that follow discuss the approaches which have been applied toward the goal of identifying ion charge and velocity. We first discuss the estimation of ion β based on the largest δ-ray identified in the cluster pattern. Then the methods for isolating ion charge are discussed along with the effectiveness of the applications.

There are two charge identification algorithms that have been tested, with several more in the early stages of development. The tested approaches are covered in detail within this chapter, and those remaining are described in chapter 8. The first of the tested algorithms uses stopping power estimated from track LET and combines this with the estimate for minimum β. The second approach divides the cluster into core and skirt regions, with the ratio of the energies in these two areas providing information on the incident particle's charge.

7.6.1 Estimate of β from δ-rays

A per track estimate of $\beta = v/c$ is required to do general binning of charge and velocity on an individual particle basis. The Timepix data contains pixel maps with energy and spatial distribution information after calibration is applied. The pattern recognition algorithms employed use a border identification algorithm to isolate individual clusters. Applying a core isolation algorithm to the cluster pixel maps, the simplest example of which would be to use a threshold energy to divide high energy core from low energy 'skirt' or 'brim' regions, allows the core to be separated from the skirt region containing the δ-ray information. The same border identification algorithms used to isolate the clusters can then be used to isolate individual δ-ray tracks. The individual δ-ray tracks can then be analyzed to find total energy in the knock-on electron tracks.

A comment on the current accuracy of the identification should be made here. The algorithms employed are not robust to the point of differentiating electron-type wandering tracks (multiple scattering) from other, straight-line type tracks within the cluster structure, and so the likelihood exists that clusters/tracks from interactions will be misinterpreted using this method without additional checks or analysis involved. Such algorithms have been implemented for whole clusters, but have not been applied to sub-clusters since the required separation algorithms have not been developed fully. In addition, due to the effects of scattering on the high energy electron paths in the silicon, heavy

ion tracks with several closely spaced δ-ray tracks have a higher likelihood of over-inflating the β estimate due to overlapping electron tracks.

Method

Once one has found the track with the largest energy in the set of δ-ray tracks, the maximum energy can be used as a lower limit in the calculation of β, since the highest energy δ-ray seen in a track provides a lower limit on the energy of the incident ion based purely on the kinematic analysis.

From the Particle Data Group reviews section 31.2.2 [15], the maximum energy possible for an ion to impart to an electron in the "low-energy" approximation is:

$$T_{max} = 2m_e c^2 \beta^2 \gamma^2 \tag{7.6}$$

which is valid when $2\gamma m_e/M \ll 1$.

The validity of the low-energy approximation holds for protons up to approximately $0.995c$. Using m_e/m_p as the ratio in the validity criteria, the criteria simplifies to $\gamma(0.001) \ll 1$, and γ does not exceed a value of 10 until around $0.995c$. Larger ions with β less than or equal $0.995c$ should also maintain the validity of this approximation since only the denominator mass will increase, causing the overall value of the right hand side of the inequality to decrease. However, above this value of β, the validity of the approximation should be verified. See Jackson for additional information [143] on an analysis of the introduced error related to collisional energy loss.

Solving Equation 7.6 for β yields the following:

$$\beta = \left[\frac{T_{max}}{2m_e c^2 + T_{max}}\right]^{1/2} \tag{7.7}$$

This is the form used to find the lower limit on β, using the largest identified δ-ray energy per track as T_{max}. Using natural units ($c = 1$), further simplifies the denominator.

Results

Figure 7.9 shows that the distribution of β in ^{56}Fe and in ^{28}Si accelerator data. This method is completely dependent on the production of δ-rays by the incident ion, and so as the number and range of the produced δ-rays decrease, the method becomes less effective in providing meaningful estimates of β. For those ions which produce δ-ray components, however, this method provides a lower limit on the particle velocity which can be used to sort the track into identification bins as described in the next section.

The values beyond the expected β value in figure 7.9 are not surprising based on previous discussion relating to electron track isolation and overlap for heavy ions. In addition, the accelerator data runs present the challenge of short bursts of high particle counts which are very close to one another both in distribution and arrival time. The values observed above the expected β are likely the result of multiple δ-rays overlapping in the periphery of the clusters or of interaction products being improperly assumed to be δ-rays. The

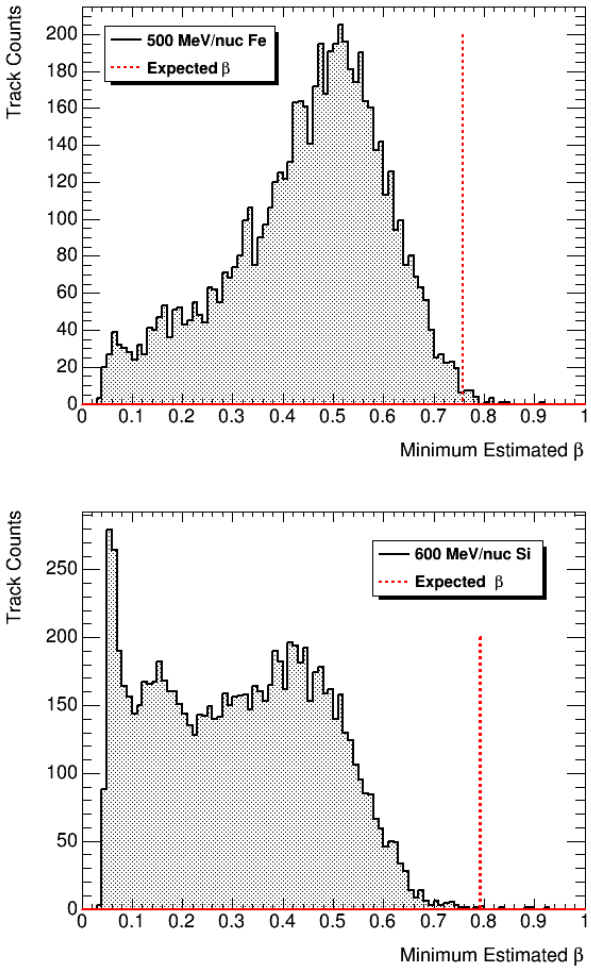

Figure 7.9: β estimation algorithm results for 500 MeV per nucleon ^{56}Fe and 600 MeV per nucleon ^{28}Si data taken at HIMAC. The black curve is the data histogram, with the red vertical line indicating the expected β value calculated from accelerator run parameters.

current algorithms do not differentiate between apparent interaction products and δ-ray production. Though analysis flags are included to attempt such separations in existing algorithms, the pattern recognition component has not been refined far enough to reliably separate such products. The analysis flags, which currently have a high false-positive rate, indicate the number of these products in on-orbit data is less than one percent of all clusters.

7.6.2 Binning Based on Linear Energy Transfer and β

At this point in the analysis, electron and stopping ion tracks have been identified and can be excluded from further processing. Excluding these tracks allows both a decrease in the computations necessary to complete the processing as well as increase in confidence that the tracks being processed contain tracks where energy loss along the track remains relatively stable within the bounds of statistical fluctuations in energy loss. [15, 46]

The individual steps along the energy loss profile may be considered as individual energy loss measurements. Without significant change in the energy loss along the track profile, the LET and the average of the energy loss along the track converge to the same value. While energy loss and stopping power are not directly equivalent, the assumption is made that the two are sufficiently equivalent to perform the analysis, and, under these conditions, LET is used as a surrogate for stopping power.

Method

Much of the necessary overhead in terms of analysis has been done by this point in the calculation, and the remaining task is to find solutions for ion velocity and charge at a given stopping power. With electrons and stopping ions removed, the energy loss along the remaining tracks is expected to vary about an average. Making the assumption then that this average value is the LET, and using it as a surrogate for stopping power allows us to define a minimum charge for the ion. This is done by excluding the solutions to the Bethe-Bloch equation (see eq. 2.3) for charge states with minimum ionization stopping powers above the LET surrogate for the current track.

The minimum β calculated for the track further isolates the possible solutions. As an example, at stopping powers below roughly 3.5 KeV/μm, which is the stopping power for minimum ionizing lithium ions, the incident particle charge ze can be limited to that of hydrogen or helium (see figure 7.10). The minimum β further limits the possible charge and velocity possibilities.

Results

This method of using LET and the lower estimate on β provides for binning of ion tracks based on isolation of the available range of charge and velocity values. Figure 7.11 shows the method as applied to several ion species using data taken at the HIMAC facility in Japan along with the related Bethe-Bloch curves. The estimated minimum $\beta\gamma$ values, as calculated from the δ-ray based

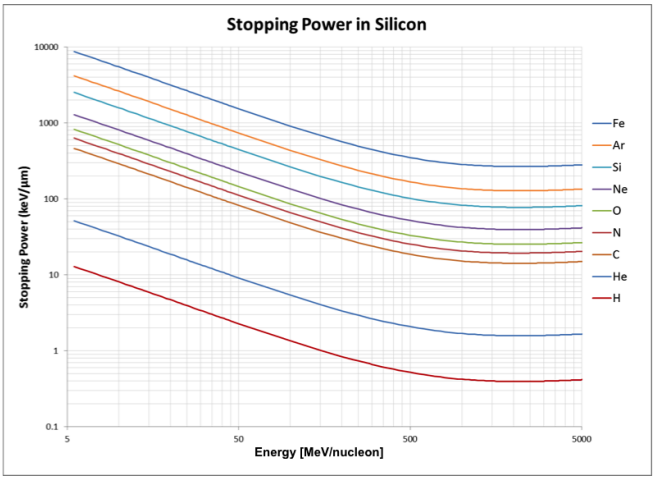

Minimum dE/dx (keV/μm)	
H	0.395
He	1.580
Li	3.555
Be	6.319
B	9.874
C	14.219
N	19.353
O	25.278
Ne	39.496
Si	77.413
Ar	127.968
Fe	266.996

Figure 7.10: Stopping power in relation to incident ion energy and charge, with the assumption of full ionization (z=nucleon count). Minimum ionizing energies are also given for the plotted curves.

estimate of β, fall within the range between zero (i.e. no delta rays identified) and the related Bethe-Bloch curve for most of the data points, with some exceeding the Bethe-Bloch value. This is consistent with previous discussions on the β estimate and is a result of interactions and track overlap.

In addition, we note that the LET values are self consistent for the majority of the data points, and vary about an average value as expected. In applying the binning to individual ion tracks, the silicon and neon data shown would be consistently limited to charge bins falling below the minimum ionization energy of iron at approximately 267 KeV/μm, while the iron data would not.

These results show promise with several opportunities for further refinement as discussed in the chapter 8. Improvements are possible by increasing confidence in the separation and isolation of individual δ-rays, which in turn

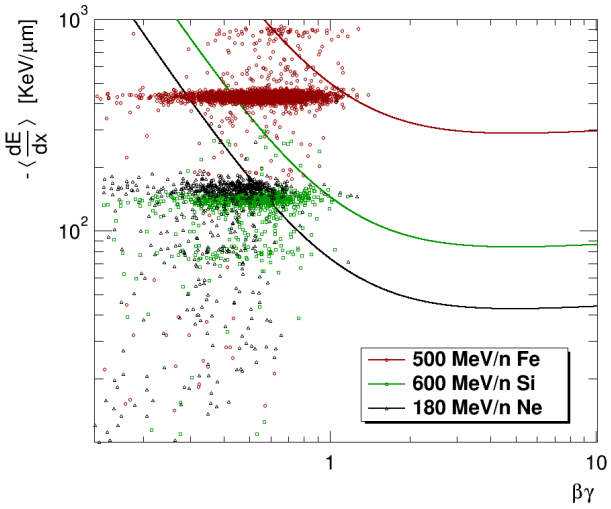

Figure 7.11: LET and minimum $\beta\gamma$ estimates for iron, neon, and silicon ions at measured at HIMAC. The lines represent the calculated Bethe-Bloch curve for each of the three different ions in silicon.

increases confidence in the estimate of β. The use of most probable energy loss instead of Bethe-Bloch stopping power is also discussed in chapter 8 as a suggested improvement path, and work on these and other refinements will continue within the framework of the larger joint project between the University of Houston and NASA Johnson Space Center.

7.6.3 Energy Ratio of Core and Skirt

Investigations by Dr. John Idarraga revealed that the ratio of cluster 'skirt' to total cluster energy provided charge separation information. This was tested for several angles of incidence using data taken at HIMAC with good results for ions at energies with well separated stopping powers relative to one another.

Figure 7.12 shows this separation for three ions. Ions with similar stopping powers are not as well resolved, as shown in figure 7.13. This correlates well with work being done at IEAP by Dr. Jan Jakubek which has linked cluster skirt formation with the magnitude of ionization along the track (see chapter 8 for further details).

This approach requires a consistent separation of cluster skirt and core regions beyond a simple energy cut-off level. Some work has been done to increase the robustness of the cluster skirt isolation, and efforts in this area are ongoing.

The ratio of cluster 'skirt' to total energy is also highly sensitive to track overlap. The energy contained in the 'skirt' region is minimal compared to the cluster core. If tracks overlap, significant portions of the 'skirt' are contained in the overlapping cluster, changing the ratio of 'skirt' to total cluster energies. This is assuming the tracks can be separated. In figure 7.12, the less distinct iron bunch near 300 MeV is a result of overlapping tracks as shown in 7.14.

7.6.4 Unidentified Clusters

Despite best efforts to the contrary, there are pixel clusters which do not contain enough information to apply the methods described. Such clusters contain a small number of pixels and may represent low energy electrons, secondary electrons, interactions from gamma rays, or muons with an incidence angle very nearly parallel to the sensor surface normal vector. These tracks

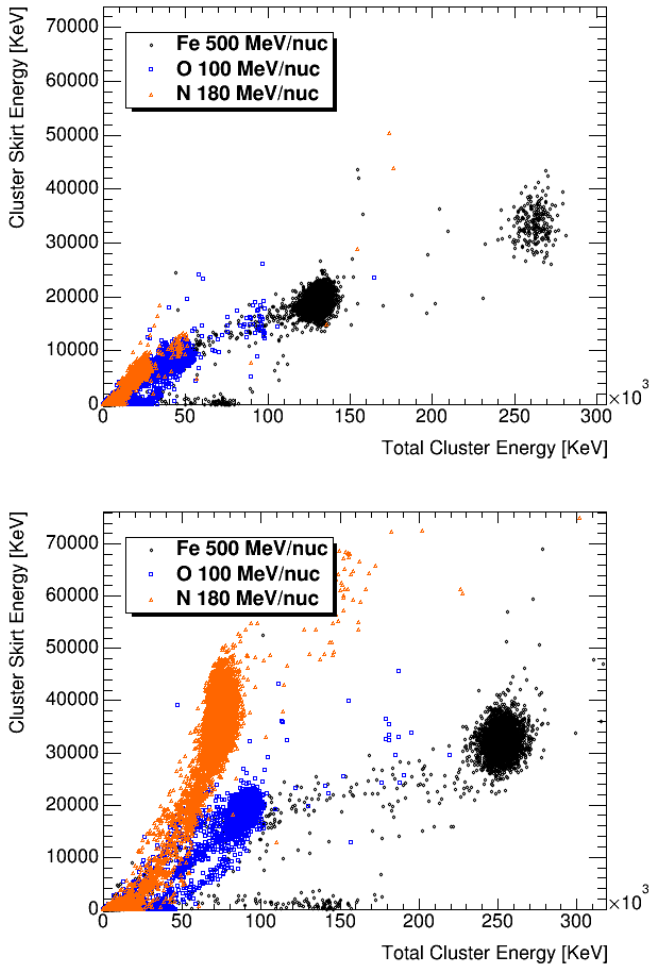

Figure 7.12: The ratio of skirt energy to total cluster energy shows separation of ions with differing stopping powers. Shown here for 0 degree (left) and 60 degree (right) angles of incidence are iron(Fe), oxygen(O), and nitrogen(N) with stopping powers of approximately 353 KeV/μm, 87 KeV/μm, and 44 KeV/μm, respectively.

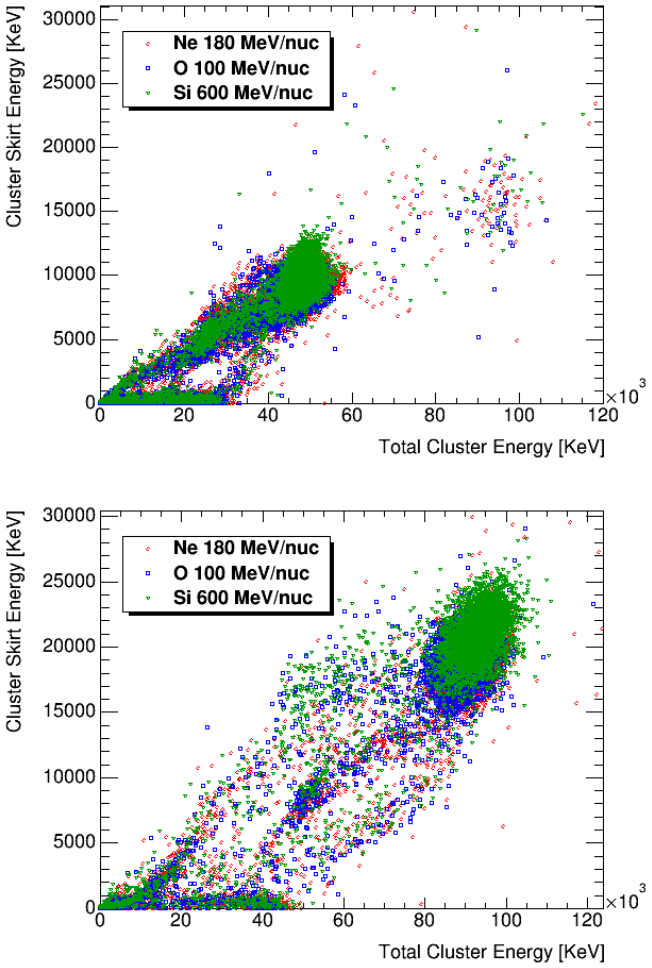

Figure 7.13: The ratio of skirt energy to total cluster energy shows overlap for ions with similar stopping powers. Shown here for 0 degree (left) and 60 degree (right) angles of incidence are neon(Ne), oxygen(O), and silicon(Si) with stopping powers of approximately 91 KeV/μm, 87 KeV/μm and 95 KeV/μm, respectively.

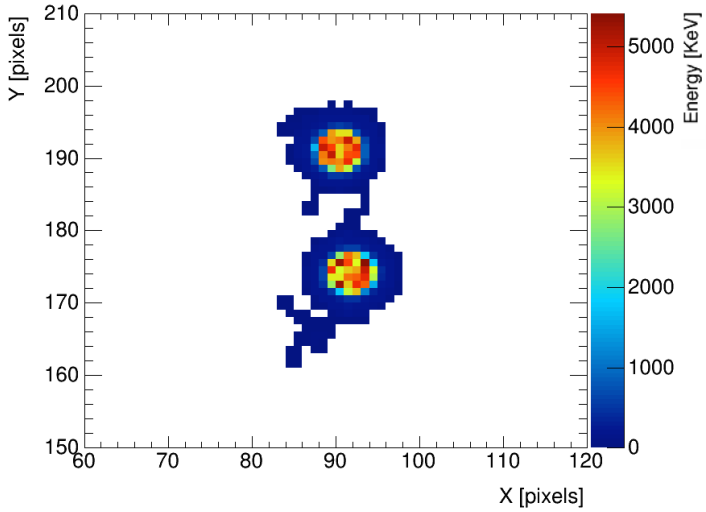

Figure 7.14: Overlapping primary tracks result in both tracks identified as a single cluster. This effectively doubles the identified cluster energy, and affects any analysis values based on cluster identification. This issue of overlap is the primary reason for the development of the frame rate algorithm used in ISS data acquisitions to minimize occurrence of such overlaps.

constitute the remainder of the radiation field after the described identification methods are applied.

To some extent, these can be isolated through cuts on the number of pixels, however above pixel counts of 6, the difference between such clusters and small electron tracks becomes much more difficult to identify without more advanced pattern recognition techniques.

Chapter 8

The Way Forward

While significant progress has been made toward the identification of ions using the Timepix detector, there are many tantalizing paths to follow which promise to increase the capabilities of the Timepix with respect particle identification. In this chapter, several avenues for development and expansion of existing methods are discussed, as well as possible applications of the Timepix hardware with the added capability of ion identification.

8.1 Upgrades to Single Pixel Detector Particle Identification Methods

8.1.1 Most Probable Energy Loss Estimates

The concept of most probable energy loss is more appropriate for measurements made with thin detectors. As discussed in chapter 2, the average energy loss value resulting from the Bethe-Bloch equation is not coincident with the energy loss distribution mode. This is a result of a small number of high energy-loss interactions. High energy δ-rays are an example of these types of interactions. [46]

Such interactions are less likely in thin detectors such as those used currently with the Timepix detectors. However, since such δ-rays are of high enough energy and have sufficient range to be visible in the pixel data, these interactions can be removed from the primary ion track for comparisons of track energy loss profiles to most probable energy loss calculations.

Work describing the energy loss profiles of Timepix based measurements for application to hadron therapy beam characterization has been done recently by researchers at the Institute for Experimental and Applied Physics at the Czech Technical University in Prague. [139, 140] The work shows that such energy loss profiles can be found for electron and proton tracks in silicon Timepix detectors.

Most probable energy loss is a function of thickness of a thin absorber.

Since the variation of incidence angle changes the detector thickness as seen by the incident ion, the most probable energy loss calculations must take into account both detector thickness and angle of incidence. Aside from this aspect, the approach for finding ion charge is the same as that described previously for LET estimates.

8.1.2 δ-ray Angular Information and Incident Particle Identification

The expression for delta ray angle in terms of incident particle T_{max} and δ-ray energy has the potential to allow calculation of the T_{max} of a particle based on one or more δ-ray tracks, provided the direction of travel of the secondary electrons can be determined.

The latter presents some difficulty for several reasons . Electrons undergo multiple scattering interactions causing the distinctive meandering path characteristic of low energy electron tracks in silicon. In addition, the δ-ray tracks are difficult to isolate and identify separate from the core of the track. Often multiple δ-ray tracks can overlap, causing difficulty in the pattern recognition and image analysis algorithms used to isolate δ-rays from the core of the track.

The fact that the electron track pattern is a 3-dimensional, multiple-scattering path projected into the 2 dimensions of the detector pixel grid complicates the problem of identifying the ejection angle. However, the approach has the potential to provide a much better estimate of T_{max} than previous approaches

using only δ-ray energy if this hurdle can be surmounted.

Finally, since the separation of the δ-rays from the core is difficult, some portion of the charge/energy of the δ-ray will be contained within the cluster 'skirt', or possibly even completely enveloped by the skirt. Data taken with 500 μm and thicker sensors, along with recent work by Jan Jakubek on the cause of the 'skirt' or 'brim' regions, indicates the δ-rays may still be able to be resolved, though with some uncertainty added in terms of the baseline signal added by the 'brim' region.

The equation describing δ-ray ejection angle is given in the Particle Data Group reviews (PDG equation 31.9) and is given below [15]:

$$\cos\theta = \frac{T_e}{p_e}\frac{p_{max}}{T_{max}} \tag{8.1}$$

When combined with the equation for the "low-energy" approximation of T_{max} (equation 7.6):

$$T_{max} = 2m_e c^2 \beta^2 \gamma^2 \tag{8.2}$$

this yields the following:

$$\beta\gamma = \left[\frac{T_e}{2cp_e\cos\theta}\right] \tag{8.3}$$

Where T_e is the δ-ray energy, p_e is the δ-ray momentum, p_{max} is the maximum momentum possible for the electron due to T_{max}, θ is the angle of deflection relative to the primary ion track, and c is the speed of light.

dE/dx can be plotted versus $\beta\gamma$ and the intersection can be compared to Bethe-Bloch curves to find an estimate for effective charge of the incident ion.

8.1.3 δ-ray Spectra and Distribution Properties

Another interesting path for investigation is the use of the δ-ray spectrum of an ion to be generated and used to better estimate the ion velocity. This type of investigation will require significant work in extending the pattern recognition algorithms to allow separation of overlapping or very closely spaced electron tracks. Provided the ion has generated enough knock-on electrons and these can be isolated, the δ-ray spectrum can be fit to give additional information on ion velocity.

8.1.4 Stopping Power Difference Along Track

Generation of the cluster energy loss curve along the direction of travel provides information regarding energy loss at points along the ion track. Thus the possibility exists for examining the change in energy loss at the beginning and end of the track. Correlating this with distance traveled or total energy deposited may provide enough information for a subset of ions to be identified below the minimum ionization energies.

8.1.5 Cluster Skirt Extent and Ion Charge

As discussed in the related section in chapter 7, the use of cluster pattern skirts may be able to provide additional information on the charge of the incident ion. Improvements in methods used to isolate cluster core and skirt regions should provide more consistent results for a larger range of cluster patterns and incidence angles.

The development of a full detector response model, as discussed in section 8.2.1, would benefit this task of isolating the cluster core in that work on such separation would benefit greatly from having control over the incident ion energies in much greater detail than current accelerator data sets provide.

8.1.6 Interaction and Fragmentation Identification

The methods described in chapter 7 rely on the removal of overlapping tracks and tracks resulting from nuclear interactions within or near the sensor. Additional refinement in the operation of the pattern recognition utilized to identify such tracks will increase the reliability of any subsequent identification operations applied.

8.2 Analysis Tool Upgrades

8.2.1 Development of Full Detector Response Model

One of the more important advances necessary for continued progress in using Timepix detectors for particle identification is the creation of a robust simulation of the charge collection and digitization by the detector. Along those lines, work is ongoing by Dr. Jan Jakubek at IEAP toward developing an analytic description of the charge generation, collection, and digitization in the Timepix hardware.

Dr. Jakubek's model, in it's current state, shows that the low energy penumbra surrounding the core pixels (the 'skirt' or 'brim'), is a linearly dependent function of the ionization imparted by the incident ion. Further, the model indicates that the charge induced during the collection time affects the measured signal. [93]

The combination of Monte Carlo particle transport codes and a Timepix hardware simulation will allow the creation of Timepix data set simulations. Such simulations, where the input particle spectrum is known, could then be used as input for analysis algorithms to verify methods for ion identification or other processes.

8.3 Hardware Refinement

8.3.1 Timepix3

The Timepix3 hardware is in development, with the first batch of units available for general testing expected in mid 2014. [144] The Timepix3 departs from the frame-based data acquisition and instead moves to a constant data stream acquisition philosophy. The Timepix3 will have two identical sets of acquisition and digitization electronics in each pixel, allowing one to continue data acquisition while the other sends the previously acquired data for retrieval.

The Timepix3 will also have the capability to provide both Time of Arrival (ToA) and Time Over Threshold (TOT) information simultaneously for each pixel. This combination will allow reconstruction of individual tracks based on both temporal and spatial information, with the added information of when individual pixels within the cluster were activated relative to other pixels. While this presents some challenges in filtering through the data stream to reconstruct track clusters, the added information will allow for determination of ion direction of travel as well as eliminate the requirement to separate of overlapping tracks which exists in current Timepix data. [144]

Once the track reconstruction is complete to create pixel clusters for individual ion tracks from Timepix3 data, the previously described algorithms will be portable to the data since pixel size and changes to the geometric details in the Timepix3 sensor will be transparent to the end user in terms of data. The

current approach of analyzing clusters of pixels corresponding to individual ion tracks will remain consistent between Timepix and Timepix3 data analysis.

8.3.2 Embedded Systems

The Timepix based Radiation Environment Monitor hardware currently aboard the ISS has proven to be a robust radiation measurement system on par with existing radiation monitoring hardware. As a result, NASA has begun developing dedicated radiation monitoring hardware based on the Timepix technology. The Battery-operated Independent Radiation Detector (BIRD) project is expected to fly on the Multi-Purpose Crew Vehicle (MPCV) test flight in 2015. A distributed monitoring system is currently in the design phase as well for use on the MPCV crewed missions, and further development projects are expected along similar lines.

This shows the need to transition current and future identification algorithms into the embedded systems regime. This will require significant optimization in order to transfer identification algorithms to such systems, however the opportunity also exists to develop hardware systems based upon only the necessary analysis components in order to build dedicated monitoring hardware.

The size and minimal power draw of the Timepix hardware, combined with embedded hardware systems to perform the necessary analysis, puts the goal of small, crew-worn, active radiation detectors within reach.

Chapter 9

Summary

The Timepix detectors present a unique opportunity to adapt existing technology to the space radiation environment. The low power requirements and small mass make it ideal for use in aerospace applications. Timepix-based detectors are already being used in research related to medical imaging and radiation monitoring, and the capability of the hardware is driving further developments both in Timepix hardware design and in development and expansion of application of the devices to new challenges.

The Radiation Environment Monitor hardware currently deployed aboard the International Space Station is the first application of Timepix detector technology to manned spaceflight. The hardware has been providing data continuously since late 2012 and has proven to be capable of providing dosimetry information on par with existing operational radiation monitoring hardware on the ISS. With NASA moving to a particle charge and energy dependent

assessment of radiation risk for its astronauts, the Timepix is poised to provide a significant portion of the required radiation monitoring capability.

In this work we have focused on presenting the progress made both in adapting the Timepix technology to spaceflight applications, as well as in the development of data analysis techniques for extension of the already significant capability of the Timepix devices. The development of a feedback-based adjustment algorithm which has been incorporated into current NASA Advanced Exploration Systems projects to control similar Timepix based acquisitions, has been reviewed. We have also discussed the current progress in identifying electron and stopping ion tracks within the data. The stopping ion track identification presents a significant computational hurdle, but it also presents an excellent opportunity to measure the low energy proton component of the environment within the spacecraft. And while the computational hurdle is significant, it is not insurmountable using current high performance computing resources.

Finally, progress in estimating ion velocity in terms of $\beta = v/c$ was discussed, along with methods to bin ion tracks by charge component. We touched upon the ongoing work relating to development of device response simulations. The tasks ahead are complex, but there are many exciting paths to follow which promise to bring the goal of charge and velocity identification in the space environment within reach.

Appendices

Appendix A

ROOT Data Structure for Timepix Data

In this appendix we describe the implemented data structures for the various analysis levels and the associated data keys used within each.

A.1 Raw Data

The data saved by either the standard Pixeleman software [117] or by the ISS REM flight software [112] allows data to be written both in human readable and in binary format, as specified by the user. The frame data is written to one file, and the meta-data, such as start time and DAC settings, is saved to a separate, but similarly named file.

Binary format saves the data frame information in a big-endian [x,c] for-

mat, with meta-data in text format. The binary format is the most compressed of the available data formats currently available for data taking with the Pixelman variants, but it requires specific data conversion methods to reconstitute the data into a form useful for analysis.

The ASCII format uses either an [x,c] format or an [x,y,c] format in most cases. In the [x,c] format, the data is written as a list of pixel number (x), from 0 to 65535, and TOT counts (c). In [x,y,c] format, the pixel number is instead expressed as an (x,y) grid pair each ranging from 0 to 255.

In addition, the data can be stored in a multiframe format, where multiple frames of data can be saved in one file. Similarly, the meta-data files are stored in a single file. The multiframe format creates a third file as well, with the extension .idx, whcih correlates the frames between data and meta-data files for file read operations. The user determines how many frames will be stored to a single file, and using the multiframe format provides for easier data storage and file transfer as compared to storing data in individual frame files.

A.2 Level1 Data

Level 1 data are organized according to acquisition frame. Each frame has a set of metadata as well as a set of pixel locations, energies, and TOT counts within each frame. The data is stored in a ROOT TTree format within a ROOT TFile data structure. [118, 119] The following is a list of the data keys within the data structure, as well as a brief description of the information

contained within the key. The data analysis is written using C++. [145]

Data Type	Parameter Name	Description
map (int,int)	m_frameXC	Vector of map pairs containing pixel [x,c] data for frame in TOT counts
map (int,double)	m_frameXC_E	Vector of map pairs containing pixel [x,c] data for frame in energy [KeV]
Int_t	fWidth	
Int_t	fHeight	
Int_t	fAcq_mode	Refers to Timepix acqusition mode
Double_t	fAcq_time	Frame time length
TString	fCustom_name	
TString	fChipboardID	Chip specific identifier
vector (Int_t)	fDACs	DAC values recorded for frame
TString	fFirmware	
Double_t	fHV	Bias voltage setting
Int_t	fHw_timer	Hardware clock setting
TString	fInterface	
Double_t	fMpx_clock	Medipix clock setting
Int_t	fMpx_type	Hardware variant
TString	fPixelmanVersion	
Int_t	fPolarity	Collect electrons or holes
Double_t	fStart_time	Unix epoch time of acquisitions start
String	fStart_timeS	Human readable acquisition start time
Double_t	fTimepix_clock	Timepix clock setting
Double_t	fLatitude	SGP4 Latitude
Double_t	fLongitude	SGP4 Longitude
Double_t	fAltitude	SGP4 Altitude
Int_t	m_occupancy	Ratio of non-zero to total pixels
Double_t	m_DoseRate	Dose rate of the frame
Double_t	m_DoseEquivalentRate	Dose Equivalent rate of the frame

A.3 Level2 Data

Level 2 data are organized according by individual clusters while retaining the information necessary to reconstruct the frame if desired. Each cluster

retains a set of the metadata for the frame to which is belongs, as well as a set of pixel locations, energies, and TOT counts relative to the original frame pixel grid. The data is stored in a ROOT TTree format within a ROOT TFile data structure. [118, 119] The following is a list of the data keys within the data structure, as well as a brief description of the information contained within the key. The data analysis is written using C++ and utilizes a MapEntry class constructed to hold the individual pixel location and energy information within the cluster (i.e. within the local map of pixles). [145]

MapEntry Class:		
Data Type	Parameter Name	Description
Int_t	X	Pixel X grid position
Int_t	Y	Pixel Y grid position
Double_t	Energy	Pixel energy value

ClusterProperties Class:		
Data Type	Parameter Name	Description
Bool_t	cflag_IsHeavyIon	Set true if ze>1
Bool_t	cflag_IsStopping	Set true if identified in stopping algorithm
Bool_t	cflag_IsSymmetric	Set true if transverse profile peak is near centerline
Int_t	sm_clusterX	from BlobFinder
Int_t	sm_clusterY	from BlobFinder
Int_t	sm_frameNumber	Frame count within file - used for associating clusters within same frame
Int_t	sm_blobNumber	Cluster count within frame
Int_t	sm_deltaRayCount	Number of delta rays identified
Int_t	cflag_IsAnomalous	0 if not anomalous (false), but otherwise it holds the number of peaks found in the cluster
Int_t	cflag_type	from MPXTree m_type: -1 indicates interaction or overlap. -2 indicates cluster lies on the detector border (pixel x or y of 0 or 256)

Float_t	sm_coreCenterX	Geometric cluster center in X
Float_t	sm_coreCenterY	Geometric cluster center in Y
Float_t	sm_roundness	measure of cluster roundness from 0 to 1 (deviation from circle of same area, 1 indicates circular cluster) [Not Implemented]
Float_t	sm_linearity	measure of cluster stretching from 0 to 1 (ratio of on axis vs across axis range) [Not Implemented]
Float_t	sm_straightness	measure of cluster curvature- deviation distance from cluster centerline in microns
Double_t	sm_CGX	Cluster Center of Gravity X coordinate
Double_t	sm_CGY	Cluster Center of Gravity Y coordinate
Double_t	sm_slope	Ratio of the track lengths in the plane of the detector surface - use atan(slope) to get angle
Double_t	sm_angle	Angle of the track through the detector relative to the surface normal (i.e. the dip angle)
Double_t	sm_totalEnergy	Energy sum within cluster
Double_t	sm_coreEnergy	Energy sum within core of cluster
Double_t	sm_coreRange	maximum distance from geometric center to core edge
Double_t	sm_skirtEnergy	difference between full cluster and core cluster energy
Double_t	sm_skirtRange	maximum distance from geometric center to skirt edge
Double_t	sm_LET	Linear Energy Transfer for cluster (from BlobFinder)
Double_t	sm_transverseRange	maximum distance across the track perpendicular to the the path of travel
Double_t	sm_deltaRaysEnergy	Total energy of identified delta rays [KeV]
Double_t	sm_maxDeltaRayEnergy	in KeV
Double_t	sm_maxDeltaRayRange	in micrometers

Double_t	sm_betaFloorEstimate	This is a derived estimate of minimum possible beta from the maxDeltaRayEnergy and the formulation for Tmax from Bethe-Bloch theory [see PDG Online]
Double_t	sm_borderFraction	The fraction of border pixels (technically non-inner-pixels) relative to the total number of pixels in a cluster - used in isolating electron tracks
Double_t	sm_StoppingIonProb	Value greater than 1e-7 seems to return good confidence in the ion being a stopping proton. This value is returned from MinimizeKolmogorov function and gives the Normalized probability of the ion being a stopping proton (upgrade later to look at isotopes or other ions)
Double_t	sm_frameTime	from Level 1 data
Double_t	sm_acqTime	from Level 1 data in seconds as recorded in the metadata from the Timepix
Double_t	sm_lat	from Level 1 data
Double_t	sm_lon	from Level 1 data
Double_t	sm_alt	from Level 1 data
TString	sm_frameFile	File name of parent file
TString	sm_chipboardID	from Level 1 data
vector (Double_t)	sm_HEDeltaRayEnergies	This is the list of energies summed from individual blobs within the deltaRay pattern after core cluster removal
vector (MapEntry)	sm_mEntry	Vector containing list of x,y,E information for all pixels in the cluster
vector (MapEntry)	sm_mCoreEntry	Vector containing list of x,y,E information for pixels in core of cluster
vector (MapEntry)	sm_mWithoutHEDeltaEntry	Vector containing list of x,y,E information for skirt without delta-rays
vector (MapEntry)	sm_mHEDeltaRays	Vector containing list of x,y,E information for delta ray pixels in cluster

Appendix B

Data File Naming Convention

Using the following format for ROOT data file names on calibrated Timepix data allows the datasets to be identified by the relevant parameters without the need to open the files and inspect the associated metadata. It also allows for selection and processing of files based on parsing the filename. The format is below, with the individual element descriptions following. This iteration of the file naming convention was adopted beginning Nov 14, 2013.

MMM_SS_EEEE_PAA-RRR_BBB_II_UUUUUUUU_FFFF_DDDDDD.root

M - incident particle Mass

S - elemental Symbol of the incident particle (i.e. Fe for Iron)

E - incident particle Energy in MeV per nucleon

P - direction of the surface normal of the Timepix detector relative to ion travel (P is positive along the ion velocity vector component, N is opposite the velocity component)

A - incident Angle relative to the surface normal of the Timepix detector

R - Rotation angle in the plane of the detector surface clockwise from vertical (y axis of detector grid)

B - applied Bias voltage in Volts

I - IKrum setting

U - Unit chip identifier (i.e. 'G03-W0094')

F - first four letters of the Facility where data was acquired (i.e. 'HIMA' for data taken at the HIMAC facility)

D - Date of the data acquisition in MMYYYY format with the two digit month and four digit year (i.e. '022013' for February 2013)

.root - standard root file format designation

In the event that the space allocated for the parameter is larger than the number of parameter digits or letters, leftmost entries in the field are replaced with zero for numerical values or with underscore for text entries.

Example:

014__N_0180_N00-000_035_03_B04W0015_HIMA_022009.root

This is the filename for 180 MeV/nucleon ^{14}Ne (Neon) with the incident beam directed normal to the detector surface. The detector layer is toward the beam aperture and not rotated. The unit chip ID is B04-W0015 with an IKrum of 3 and a bias voltage of 35V. The data was acquired at HIMAC in February of 2009.

Appendix C

Conversion of on-orbit data to units of pfu

Flux for the ISS REM data (found in pfu per LET) is calculated as follows:

1. Create a histogram of individual particle (track) LET using log-width bins to produce an LET spectrum in terms of raw particle count

2. Scale the histogram by the inverse of total acquisition time for the region traversed (SAA, etc.) which converts from raw particle count into particles per unit time

3. Divide each histogram bin by the bin width (in KeV/um), converting to counts per unit time per unit LET

4. Scale the histogram by the inverse of the geometrical factor for a single element particle telescope (see Sullivan 1971) [146]. This final step incor-

porates the geometry of the detector and includes area and solid angle to get the final flux in particles per square centimeter steradian second per unit LET. [147] This equates to units of pfu (particle flux units) per unit LET, such that integration over the LET spectrum provides total flux in pfu.

This process, while viable, ignores the capability of the Timepix to determine the angle of incidence for particle tracks. In this respect, the isotropic field assumption used by Sullivan is not complete for this detector, since there are portions of the radiation field which may be highly directional, such as the South Atlantic Anomaly in Low Earth Orbit. By including the directionality information when calculating flux, one can include the capability to determine flux variations over the solid angle viewed by the detector.

Appendix D

Timepix calibration

The Timepix detector provides pixel based measurements of Time Over Threshold (TOT). While the TOT values are proportional to the energy deposited, each unit must be calibrated to find the per-pixel mapping of TOT to energy. Much work has already been done on this topic, including temperature dependence of the calibrations, and the following is a short summary of the process as performed for ISS REM units by Martin Kroupa. [71, 148–150]

Initially, a threshold equalization scan is performed in order to get the optimal settings for noise-free data acquisition. The threshold equalization process scans through multiple settings of the local threshold values (i.e. on-pixel values, as opposed to the larger valued global threshold for the entire Timepix) and sets individual pixel thresholds based on the scan response. Following the threshold equalization process, there may be a few isolated pixels that require further manual adjustment, but the number of such pixels is

usually very limited.

An ^{241}Am source and a foil of Sn, or other materials depending on desired secondary production, along with an ^{55}Fe source, are used to produce the calibration radiation fields. Single pixel hits are required for accurate calibration since these clusters contain all the energy deposited in the pixel being calibrated, reducing errors due to charge sharing or threshold differences between pixels. In general, acquisition times are optimized to obtain the best rate of single pixel hits in order to minimize overlapping or directly adjacent clusters.

Table D.1: Sources and Energies used for ISS REM Calibration

Nuclide	Primary Energy [KeV]	Florescence Energy [KeV]
^{241}Am	59.54	-
^{118}Sn	-	25.27
^{55}Fe	5.90	-

The spectrum obtained from single pixel hits provides a per-pixel data set to perform the required calibration analysis. A curve containing the relevant peaks (Am, Sn, and Fe in this case) is obtained for a given pixel. From this, the Am and Sn peaks provide data points to correlate Time Over Threshold counts to energy values. The low energy 'knee' in the calibration curve (see Figure D.1) is found by deconvoluting the Fe curve from the Am and Sn curve fits. The resultant curve fit yields four calibration parameters, a, b, c, and t, for the pixel, and the process is repeated for all 65536 pixels in the detector.

Pixels that fall very far outside the range of the average fit parameter values

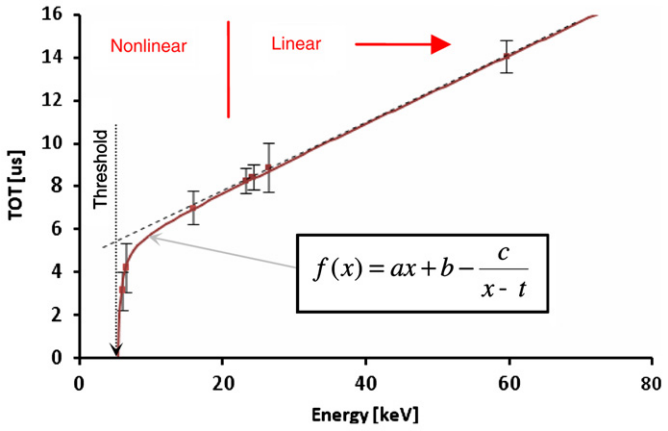

Figure D.1: The multi-parameter fit to calibrate Time Over Threshold to energy values for the Timepix detectors is shown as developed by Jan Jakubek at IEAP. [71]

for each of the four parameters are masked (i.e. the output is ignored). The parameter values for these masked pixels are found by interpolating across neighboring pixels. This ensures that values of the fit parameters remain within viable bounds for the device and processing software, while the masking removes the related TOT/energy information from the output data stream.

The original spectrum used for the calibration is used with the calibration to verify that the energy peaks in the spectrum correspond to the expected peaks for the sources used. Resolution for a high quality detector layer results in a sigma near 1.8 in KeV. It is important to note that changing DAC settings on the Timepix, such as Ikrum, or using a different pixel configuration file than that used for calibration (i.e. changing the pixel mask settings) can affect the resolution and validity of the calibrations.

Appendix E

Pseudo-Random Counters

Pseudo-Random Counters are more commonly referred to as Linear Feedback Shift Registers (LFSRs). [75] The devices themselves are straightforward implementations of basic digital logic components, utilizing a series of edge triggered D type flip flops along with one or more exclusive OR gates in a feedback loop to the series input.

The flip flops are sequentially arranged so that the non-negated output of the previous flip flop serves as the input to the next flip flop in the series. Without a feedback loop, this configuration yields a shift register in which the signal at the input of one flip flop is propagated to the next flip flop during the rising pulse of the clock input. [151]

The use of XOR gates on a feedback line from one or more taps between flip flops in the chain allows the production of a pseudo-random series. Provided the chain is not allowed to enter the lock state, where all inputs are either

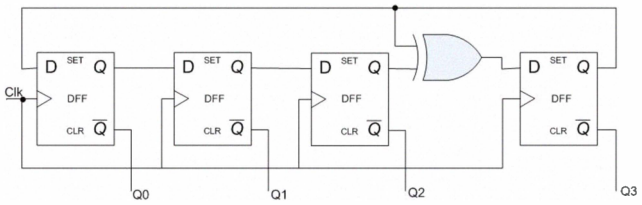

Figure E.1: An example of a 4-bit pseudo-random counter, or LFSR. The 4-bit LFSR contains 4 D-type flip flops with a feedback loop. Each clock cycle changes the state of the flip flop chain. [75]

zero or one depending on logic used, the series repeats after 2n-1 states with n being the number of flip flops in the chain. In such a configuration, the current counter state is based on the previous state of the counter chain. The selection of the XOR tap locations are dependent on the number of bits in the counter, and a primitive polynomial corresponding to tap location and number can be used to determine the device state numerically.

The end result is a shift counter that has a very fast response time, low transistor count, and a large number of available states to shift through before repeating the pseudo-random pattern. Such devices are often used in situations where power and space are at a premium in integrated circuit fabrication. An additional benefit of the LFSR is that the same circuit used for counting can be used to shift data out (data transfer) with minimal modifications. [72, 74]

Appendix F

Publications

Simulation of Van Allen Belt and Galactic Cosmic Ray Ionized Particle Tracks in a Si Timepix Detector

Nicholas Stoffle, Lawrence Pinsky, Anton Empl, Son Minh Hoang, Stanislav Pospisil, Jan Jakubek, Daniel Turecek, Zdenek Vykydal

The Timepix readout chip is a hybrid pixel detector with over 65k independent pixel elements. Each pixel contains its own circuitry for charge collection, counting logic, and readout. When coupled with a Silicon detector layer, the Timepix chip is capable of measuring the charge, and thus energy, deposited in the Silicon detector layer. FLUKA simulations of energy deposition within the silicon layer have been carried out using models describing the particle

flux within the Van Allen Radiation Belts as well as for Galactic Comic Ray particle interactions. Such simulations will be useful in characterizing the Timepix Si detector response in a mixed radiation field with application to similar detectors' future use as dosimeters and area monitors aboard manned spaceflight missions. The core technology is also applicable to purely scientific instrumentation.

N. Stoffle, L. Pinsky, A. Empl, S. Hoang, S. Pospisil, J. Jakubek, D. Turecek, and Z. Vykydal: *Simulation of Van Allen Belt and Galactic Cosmic Ray Ionized Particle Tracks in a Si Timepix Detector*, Experiments and Instrumentation, International Cosmic Ray Conference, 2011, 11, 436, DOI: 10.7529/ICRC2011/V11/1332

URL:

www.ihep.ac.cn/english/conference/icrc2011/paper/proc/vb/vb_1332.pdf

Initial results on charge and velocity discrimination for heavy ions using silicon-Timepix detectors

N. Stoffle, L. Pinsky, S. Hoang, J. Idarraga, M. Kroupa, J. Jakubek, D. Turecek, and S. Pospisil

The Timepix ASIC is a version of the hybrid pixel detector technology developed by the Medipix2 Collaboration. Within the 256 by 256 pixel matrix,

the electronics for each of the 55um individual pixels are contained in the footprint of that pixel. The Timepix has a charge-sensitive pre-amp and an associated discriminator attached to a logic unit capable of being employed in one of several different modes. For the present work, the Time-Over-Threshold mode was used to allow measurement of deposited energy in the silicon sensor layer.

Ionization along heavy ion particle tracks in the silicon sensor results in the production of free charge carriers in the detector. The charge carrier motion under the influence of an applied bias voltage leads to charge collection at the Timepix-sensor interface in one or more pixels. Signatures within the pixel cluster patterns are currently being examined, and initial results indicate that such signatures, when coupled with stopping power information, provide enough discrimination capability to begin to resolve heavy ion charge and velocity. Here we present the salient characteristics that have been identified for heavy ion charge and velocity discrimination using Timepix Silicon detectors and discuss the application of this method for particle track characterization.

N. Stoffle, L. Pinsky, S. Hoang, J. Idarraga, M. Kroupa, J. Jakubek, D. Turecek, and S. Pospisil: *Initial results on charge and velocity discrimination for heavy ions using silicon-Timepix detectors*, Journal of Instrumentation, IOP Publishing, 2012, 7, C12009, DOI: 10.1088/1748-0221/7/12/C12009

URL:

iopscience.iop.org/article/10.1088/1748-0221/7/12/C12009/pdf

Timepix-based radiation environment monitor measurements aboard the International Space Station

Nicholas Stoffle, Lawrence Pinsky, Martin Kroupa, Son Hoang, John Idarraga, Clif Amberboy, Ryan Rios, Jessica Hauss, John Keller, Amir Bahadori, Edward Semones, Daniel Turecek, Jan Jakubek, Zdenek Vykydal, Stanislav Pospisil

A number of small, single element radiation detectors, employing the CERN-based Medipix2 Collaboration's Timepix Application Specific Integrated Circuit coupled to a specially modified version of the USB-Lite interface for that ASIC provided by the Institute for Experimental and Applied Physics at the Czech Technical University in Prague, have been developed at the University of Houston and NASA Johnson Space Center. These detectors, officially designated by NASA as Radiation Environment Monitors, were deployed aboard the International Space Station in late 2012. Six REM units are currently operating on Station Support Computers and returning data on a daily basis. The associated data acquisition software on the SSCs provides both automated data collection and transfer, as well as algorithms to handle adjustment of acquisition rates and recovery and restart of the acquisition software. A suite of ground software analysis tools has been developed to allow rapid analysis of the data and provides a ROOT-based framework for extending data analysis

capabilities.

N. Stoffle, L. Pinsky, M. Kroupa, S. Hoang, J. Idarraga, C. Amberboy, R. Rios, J. Hauss, J. Keller, A. Bahadori, E. Semones, D. Turecek, J. Jakubek, Z. Vykydal, and S. Pospisil: *Timepix-based radiation environment monitor measurements aboard the International Space Station*, Nuclear Instruments and Methods in Physics Research Section A: Accelerators, Spectrometers, Detectors and Associated Equipment, Elsevier BV, 2015, 782, 143-148, DOI: 10.1016/j.nima.2015.02.016

URL:

www.sciencedirect.com/science/article/pii/S0168900215001977

Initial Report on International Space Station Radiation Environment Monitor Performance

Nicholas Stoffle, John Keller, Edward Semones

The International Space Station Radiation Environment Monitor (ISS REM) is a small, low-power, hybrid-pixel radiation detector based on the CERN Timepix technology. Five detectors were flown aboard ISS beginning in late 2012. This document contains the initial results from the first year of operation as reviewed in late 2013, including hardware issues, detector performance, and development efforts.

N. Stoffle, J. Keller, and E. Semones: *Initial Report on International Space Station Radiation Environment Monitor Performance*, NASA/TM-2016-219278,

NASA Johnson Space Center, 2016

URL:

ston.jsc.nasa.gov/collections/TRS/_techrep/TM-2016-219278.pdf

Bibliography

[1] *Radiation Protection Guidance for Activities in Low-Earth Orbit: Recommendations of the National Council on Radiation Protection and Measurements (NCRP Report 132)*. National Council on Radiation Protection, 2000, ISBN 0929600657.

[2] *Operational Radiation Safety Program for Astronauts in Low-Earth Orbit: A Basic Framework (NCRP Report 142)*. National Council on Radiation Protection, 2002, ISBN 0929600754.

[3] *Information Needed to Make Radiation Protection Recommendations for Space Missions Beyond Low-Earth Orbit (NCRP Report 153)*. National Council on Radiation Protection, 2006, ISBN 0929600908.

[4] Francis A Cucinotta, MY Kim, and Lori J Chappell: *Space radiation cancer risk projections and uncertainties-2010*. NASA Tech. Pap., NASA/TP-2011-216155, 2011.

[5] Lawrence W Townsend: *Implications of the space radiation environment for human exploration in deep space*. Radiation protection dosimetry, 115(1-4):44–50, 2005.

[6] James E. Turner: *Atoms, Radiation, and Radiation Protection*. Wiley-VCH, 2007, ISBN 3527406069.

[7] Francis A Cucinotta, MY Kim, and Lori J Chappell: *Space radiation cancer risk projections and uncertainties-2012*. NASA Tech. Pap., NASA/TP-2013-217375, 2013.

[8] David J. Griffiths: *Introduction to Electrodynamics (3rd Edition)*. Addison Wesley, 1999, ISBN 013805326X.

[9] Leonardo Rossi, Peter Fischer, Tilman Rohe, and Norbert Wermes: *Pixel Detectors: From Fundamentals to Applications (Particle Acceleration and Detection)*. Springer, 2006, ISBN 3540283323.

[10] Helmuth Spieler: *Semiconductor Detector Systems (Semiconductor Science and Technology)*. Oxford University Press, USA, 2005, ISBN 0198527845.

[11] Glenn F. Knoll: *Radiation Detection and Measurement*. John Wiley & Sons, Inc., 3rd edition, 2000.

[12] *Guidance on Radiation Received in Space Activities (NCRP Report N0. 98)*. National Council on Radiation Protection and Measurements, 1989, ISBN 0929600045.

[13] Johan Moan and Meyrick J. Peak: *Effects of UV radiation on cells*. Journal of Photochemistry and Photobiology B: Biology, 4(1):21–34, Oct 1989, ISSN 1011-1344.

[14] Jean Luc Ravanat, Thierry Douki, and Jean Cadet: *Direct and indirect effects of UV radiation on DNA and its components*. Journal of Photochemistry and Photobiology B: Biology, 63(1-3):88–102, Oct 2001, ISSN 1011-1344.

[15] J. Beringer, J. F. Arguin, R. M. Barnett, K. Copic, O. Dahl, D. E. Groom, C. J. Lin, J. Lys, H. Murayama, C. G. Wohl, and et al.: *Review of particle physics*. Physical Review D, 86(1), Jul 2012.

[16] G.D. Badhwar and P.M. O'Neill: *An improved model of galactic cosmic radiation for space exploration missions*. International Journal of Radiation Applications and Instrumentation. Part D. Nuclear Tracks and Radiation Measurements, 20(3):403 – 410, 1992, ISSN 1359-0189.

[17] G.D Badhwar and P.M O'Neill: *Galactic cosmic radiation model and its applications*. Advances in Space Research, 17(2):7 – 17, 1996, ISSN 0273-1177.

[18] Patrick M O'Neill: *Badhwar-o'neill 2010 galactic cosmic ray flux model-revised*. Nuclear Science, IEEE Transactions on, 57(6):3148–3153, 2010.

[19] M Kroupa, N Stoffle, S Hoang, and L Pinsky: *Semiconductor Radiation Detectors: Technology and Applications*, chapter Semiconductor Pixel Detectors as Radiation Monitors, page TBD. CRC Press, In press (2015).

[20] W Heinrich, S Roesler, and H Schraube: *Physics of cosmic radiation fields*. Radiation protection dosimetry, 86(4):253–258, 1999.

[21] Sebastien Bourdarie and Michael Xapsos: *The near-earth space radiation environment*. Nuclear Science, IEEE Transactions on, 55(4):1810–1832, 2008.

[22] James A. Van Allen and Louis A. Frank: *Radiation around the earth to a radial distance of 107,400 km.* Nature, 183(4659):430–434, Feb 1959.

[23] Tamas I. Gombosi: *Physics of the Space Environment (Cambridge Atmospheric and Space Science Series)*. Cambridge University Press, 1998, ISBN 052159264X.

[24] Thomas F. Tascione: *Introduction to the Space Environment (Orbit: a Foundation Series)*. Krieger Publishing Company, 2010, ISBN 0894640712.

[25] S Biswas and CE Fichtel: *Nuclear composition and rigidity spectra of solar cosmic rays.* The Astrophysical Journal, 139:941, 1964.

[26] MA Shea and DF Smart: *A summary of major solar proton events*. Solar Physics, 127(2):297–320, 1990.

[27] JR Letaw, R Silberberg, and CH Tsao: *Radiation hazards on space missions outside the magnetosphere*. Advances in Space Research, 9(10):285–291, 1989.

[28] B Klecker: *Energetic particle environment in near-earth orbit*. Advances in Space Research, 17(2):37–45, 1996.

[29] J. Giacalone, J. F. Drake, and J. R. Jokipii: *The acceleration mechanism of anomalous cosmic rays*. Space Science Reviews, 173(1-4):283–307, Nov 2012.

[30] JA Simpson: *Elemental and isotopic composition of the galactic cosmic rays*. Annual Review of Nuclear and Particle Science, 33(1):323–382, 1983.

[31] Francis A Cucinotta, Shaowen Hu, Nathan A Schwadron, K Kozarev, Lawrence W Townsend, and Myung Hee Y Kim: *Space radiation risk limits and earth-moon-mars environmental models.* Space Weather, 8(12), 2010.

[32] ER Benton and EV Benton: *Space radiation dosimetry in low-earth orbit and beyond.* Nuclear Instruments and Methods in Physics Research Section B: Beam Interactions with Materials and Atoms, 184(1):255–294, 2001.

[33] John David Jackson: *Classical Electrodynamics Third Edition.* Wiley, 1998, ISBN 047130932X.

[34] J. F. Ziegler: *SRIM, the stopping and range of ions in matter.* SRIM Co, Chester, Maryland, 2008, ISBN 978-0-9654207-1-6.

[35] Claude Leroy and Pier Giorgio Rancoita: *Principles of Radiation Interaction In Matter And Detection (3rd Edition).* World Scientific Publishing Company, 2011, ISBN 9814360511.

[36] Jerrold T. Bushberg, J. Anthony Seibert, Edwin M. Leidholdt Jr., and John M. Boone: *The Essential Physics of Medical Imaging, Third Edition.* LWW, 2011, ISBN 0781780578.

[37] William R. Leo: *Techniques for Nuclear and Particle Physics Experiments: A How-To Approach.* Springer-Verlag, 1994, ISBN 0387572805.

[38] Arthur Compton: *On the interaction between radiation and electrons.* Physical Review, 31(1):59–65, Jan 1928.

[39] National Institute of Standards and Technology, M.J. Berger, J.H. Hubbell, S.M. Seltzer, J. Chang, J.S. Coursey, R. Sukumar, D.S. Zucker, , and K. Olsen. `http://physics.nist.gov/xcom`.

[40] Robley Dunglison Evans and Atome Noyau: *The atomic nucleus*, volume 892. McGraw-Hill New York, 1955.

[41] H. Andersen, J. Bak, H. Knudsen, and B. Nielsen: *Stopping power of al, cu, ag, and au for MeV hydrogen, helium, and lithium ions. z_1^3 and z_1^4 proportional deviations from the bethe formula.* Phys. Rev. A, 16(5):1929–1940, Nov 1977, ISSN 0556-2791.

[42] P Lorrain and D Corson: *Electromagnetic Fields and Waves*. Co-CBS, 2003, ISBN 8123909802.

[43] L. Landau: *On the energy loss of fast particles by ionization*. J.Phys.(USSR), 8:201–205, 1944.

[44] P.V. Vavilov: *Ionization losses of high-energy heavy particles*. Sov.Phys.JETP, 5:749–751, 1957.

[45] P. E. Hodgson, E. Gadioli, and E. Gadioli Erba: *Introductory Nuclear Physics (Oxford Science Publications)*. Oxford University Press, USA, 1997, ISBN 0198518978.

[46] Hans Bichsel: *A method to improve tracking and particle identification in tpcs and silicon detectors*. Nuclear Instruments and Methods in Physics Research Section A: Accelerators, Spectrometers, Detectors and Associated Equipment, 562(1):154–197, Jun 2006.

[47] Hans Bichsel: *Straggling in thin silicon detectors*. Reviews of Modern Physics, 60(3):663–699, 1988.

[48] Hans Bichsel: *Straggling of heavy charged particles: Comparison of born hydrogenic-wave-function approximation with free-electron approximation*. Phys. Rev. B, 1(7):2854–2862, Apr 1970, ISSN 0556-2805.

[49] L C Northcliffe: *Passage of heavy ions through matter*. Annual Review of Nuclear Science, 13(1):67–102, Dec 1963.

[50] R. Katz, S.C. Sharma, and M. Homayoonfar: *Detection of energetic heavy ions*. Nuclear Instruments and Methods, 100(1):13–32, Apr 1972.

[51] Robert Katz: *Track structure theory in radiobiology and in radiation detection*. Nuclear Track Detection, 2(1):1–28, Mar 1978.

[52] FA Cucinotta, JW Wilson, Robert Katz, W Atwell, GD Badhwar, and MR Shavers: *Track structure and radiation transport model for space radiobiology studies*. Advances in Space Research, 18(12):183–194, 1996.

[53] Francis A Cucinotta, Robert Katz, and John W Wilson: *Radial distribution of electron spectra from high-energy ions*. Radiation and environmental biophysics, 37(4):259–265, 1998.

[54] A. Akkerman, J. Barak, and D. Emfietzoglou: *Ion and electron track-structure and its effects in silicon: model and calculations.* Nuclear Instruments and Methods in Physics Research Section B: Beam Interactions with Materials and Atoms, 227(3):319–336, Jan 2005.

[55] A. Akkerman, M. Murat, and J. Barak: *Ion track structure calculations in silicon - spatial and temporal aspects.* Nuclear Instruments and Methods in Physics Research Section B: Beam Interactions with Materials and Atoms, 269(14):1630 – 1633, 2011, ISSN 0168-583X.

[56] A. Akkerman, M. Murat, and J. Barak: *Delta-electron spectra, inelastic cross sections, and stopping powers of ions in silicon: Comparison between different models.* Nuclear Instruments and Methods in Physics Research Section B: Beam Interactions with Materials and Atoms, 321:1–7, Feb 2014.

[57] A.S. Kobayashi, A.L. Sternberg, L.W. Massengill, R.D. Schrimpf, and R.A. Weller: *Spatial and temporal characteristics of energy deposition by protons and alpha particles in silicon.* IEEE Transactions on Nuclear Science, 51(6):3312–3317, ISSN 0018-9499.

[58] A. Chatterjee and H. J. Schaefer: *Microdosimetric structure of heavy ion tracks in tissue.* Radiat Environ Biophys, 13(3):215–227, Sep 1976, ISSN 1432-2099.

[59] M Ichimura, K Kirii, and T Shibata: *δ-ray simulation for the charge determination of heavy cosmic-ray primaries with the use of a ccd scanning system.* Nuclear Instruments and Methods in Physics Research Section A: Accelerators, Spectrometers, Detectors and Associated Equipment, 300(3):616–627, 1991, ISSN 0168-9002.

[60] Gerhard Lutz: *Semiconductor Radiation Detectors: Device Physics.* Springer, 2007, ISBN 3540716785.

[61] SR Amendolia, E Bertolucci, MG Bisogni, U Bottigli, A Ceccopieri, MA Ciocci, M Conti, P Delogu, ME Fantacci, P Maestro, *et al.*: *Medipix: a vlsi chip for a gaas pixel detector for digital radiology.* Nuclear Instruments and Methods in Physics Research Section A: Accelerators, Spectrometers, Detectors and Associated Equipment, 422(1):201–205, 1999.

[62] Medipix Collaboration. `http://medipix.web.cern.ch/medipix/`.

[63] Michael Campbell: *10 years of the medipix2 collaboration.* Nuclear Instruments and Methods in Physics Research Section A: Accelerators, Spectrometers, Detectors and Associated Equipment, 633:S1–S10, 2011.

[64] M Campbell, EHM Heijne, G Meddeler, E Pernigotti, and W Snoeys: *A readout chip for a 64 × 64 pixel matrix with 15-bit single photon counting.* Nuclear Science, IEEE Transactions on, 45(3):751–753, 1998.

[65] E Heijne: *Rd19: Status report on activities in 1996-7 development of hybrid and monolithic semiconductor micropattern pixel detectors.* Leb status report/rd19 CERN/ LHCC 97-59, CERN, 10 October 1997.

[66] Xavier Llopart, Michael Campbell, R Dinapoli, D San Segundo, and E Pernigotti: *Medipix2: a 64-k pixel readout chip with 55-μm square elements working in single photon counting mode.* Nuclear Science, IEEE Transactions on, 49(5):2279–2283, 2002.

[67] Xavier Llopart: *TIMEPIX Manual v1.0.* Medipix Collaboration, CERN, 2008.

[68] P. Soukup, J. Jakubek, M. Martisikova, M. Kroupa, and S. Pospisil: *Dynamics of charge collection in pixelated semiconductor sensor studied with heavy ions and timepix.* In *Nuclear Science Symposium and Medical Imaging Conference (NSS/MIC), 2012 IEEE*, pages 4184–4187, 2012.

[69] D. H. Wilkinson: *A stable ninety-nine channel pulse amplitude analyser for slow counting.* Mathematical Proceedings of the Cambridge Philosophical Society, 46(03):508, Jul 1950.

[70] Xavier Llopart, Rafael Ballabriga, Michael Campbell, Lukas Tlustos, and Winnie Wong: *Timepix, a 65k programmable pixel readout chip for arrival time, energy and/or photon counting measurements.* Nuclear Instruments and Methods in Physics Research Section A: Accelerators, Spectrometers, Detectors and Associated Equipment, 581(1):485–494, 2007.

[71] Jan Jakubek: *Precise energy calibration of pixel detector working in time-over-threshold mode.* Nuclear Instruments and Methods in Physics Research Section A: Accelerators, Spectrometers, Detectors and Associated Equipment, 633:S262–S266, 2011.

[72] Xavier Llopart Cudié: *Design and characterization of 64K pixels chips working in single photon processing mode.* PhD thesis, Mid Sweden University, Department of Information Technology and Media, 2007.

[73] F. Krummenacher: *Pixel detectors with local intelligence: an ic designer point of view.* Nuclear Instruments and Methods in Physics Research A, (305):527–532, 1991.

[74] Winnie Wong: *A Hybrid Pixel Detector ASIC with Energy Binning for Real-Time, Spectroscopic Dose Measurements.* PhD thesis, Mid Sweden University, Department of Information Technology and Media, 2012.

[75] A. Ajane, P.M. Furth, E.E. Johnson, and R.L. Subramanyam: *Comparison of binary and lfsr counters and efficient lfsr decoding algorithm.* In *Circuits and Systems (MWSCAS), 2011 IEEE 54th International Midwest Symposium on*, pages 1–4, 2011.

[76] Jan Jakubek: *Energy-sensitive x-ray radiography and charge sharing effect in pixelated detector.* Nuclear Instruments and Methods in Physics Research Section A: Accelerators, Spectrometers, Detectors and Associated Equipment, 607(1):192–195, Aug 2009.

[77] S. M. Hoang: *A Pattern Recognition Approach to Learning Tracks of Heavy-Ion Particles in Timepix Detectors.* PhD thesis, University of Houston, 2013.

[78] Lawrence Pinsky, Nicholas Stoffle, Anton Empl, Jan Jakubek, Stanislav Pospisil, Claude Leroy, Hisashi Kitamura, Nakahiro Yasuda, and Yukio Uchihori: *Application of the medipix2 technology to space radiation dosimetry and hadron therapy beam monitoring.* Radiation Measurements, 46(12):1610–1614, Dec 2011.

[79] PA Tove and W Seibt: *Plasma effects in semiconductor detectors.* Nuclear Instruments and Methods, 51(2):261–269, 1967.

[80] Julian Becker, Klaus Gartner, Robert Klanner, and Rainer Richter: *Simulation and experimental study of plasma effects in planar silicon sensors.* Nuclear Instruments and Methods in Physics Research Section A: Accelerators, Spectrometers, Detectors and Associated Equipment, 624(3):716 – 727, 2010, ISSN 0168-9002.

[81] Mara Bruzzi: *Radiation damage in silicon detectors for high-energy physics experiments.* Nuclear Science, IEEE Transactions on, 48(4):960–971, 2001.

[82] TE Schlesinger, JE Toney, H Yoon, EY Lee, BA Brunett, L Franks, and RB James: *Cadmium zinc telluride and its use as a nuclear radiation detector material.* Materials Science and Engineering: R: Reports, 32(4):103–189, 2001.

[83] Simon M. Sze and Kwok K. Ng: *Physics of Semiconductor Devices.* Wiley-Interscience, 2006, ISBN 0471143235.

[84] Alan Owens and A. Peacock: *Compound semiconductor radiation detectors.* Nuclear Instruments and Methods in Physics Research Section A: Accelerators, Spectrometers, Detectors and Associated Equipment, 531(1-2):18–37, Sep 2004.

[85] Robert Pierret: *Semiconductor device fundamentals.* Addison-Wesley, Reading, Mass, 1996, ISBN 978-0201543933.

[86] Rafael Ballabriga: *The Design and Implementation in 0.13 μm CMOS of an Algorithm Permitting Spectroscopic Imaging with High Spatial Resolution for Hybrid Pixel Detectors.* PhD thesis, Universtat Ramon Llull, 2009.

[87] M.N. Mazziotta: *Electron-hole pair creation energy and fano factor temperature dependence in silicon.* Nuclear Instruments and Methods in Physics Research Section A: Accelerators, Spectrometers, Detectors and Associated Equipment, 584(2-3):436–439, Jan 2008.

[88] Bjorn Kreisler, Gisela Anton, Jurgen Durst, and Thilo Michel: *Charge carrier motion in semiconductors.* In *Excerpt from the Proceedings of the COMSOL Users Conference 2006 Frankfurt*, pages 64–66, 2006.

[89] Björn Kreisler, Gisela Anton, Jürgen Durst, and Thilo Michel: *3d simulation of induced signals in the medipix detector.* In *Nuclear Science Symposium Conference Record, 2007. NSS'07. IEEE*, volume 4, pages 3166–3169. IEEE, 2007.

[90] M.Ali Omar and Lino Reggiani: *Drift and diffusion of charge carriers in silicon and their empirical relation to the electric field.* Solid-State Electronics, 30(7):693–697, Jul 1987, ISSN 0038-1101.

[91] Simon Ramo: *Currents induced by electron motion.* Proceedings of the IRE, 27(9):584–585, 1939.

[92] William Shockley: *Currents to conductors induced by a moving point charge.* Journal of Applied Physics, 9:635, 1938.

[93] J. Jakubek: *The response function of semiconductor pixel detectors for highly ionizing particles.* FLUKA Collaboration Meeting Presentation, Nov 2013.

[94] Erik H.M. Heijne, Rafael Ballabriga Sune, Michael Campbell, Claude Leroy, Xavier Llopart, Jean Pierre Martin, Stanislav Pospisil, Jaroslav Solc, Paul Soueid, Michal Suk, Lukas Tlustos, Daniel Turecek, Zdenek Vykydal, and Winnie Wong: *Measuring radiation environment in {LHC} or anywhere else, on your computer screen with medipix.* Nuclear Instruments and Methods in Physics Research Section A: Accelerators, Spectrometers, Detectors and Associated Equipment, 699(0):198 – 204, 2013, ISSN 0168-9002.

[95] Kazuyoshi Akiba, Marina Artuso, Ryan Badman, Alessandra Borgia, Richard Bates, Florian Bayer, Martin van Beuzekom, Jan Buytaert, Enric Cabruja, Michael Campbell, Paula Collins, Michael Crossley, Raphael Dumps, Lars Eklund, Daniel Esperante, Celeste Fleta, Abraham Gallas, Miriam Gandelman, Justin Garofoli, Marco Gersabeck, Vladimir V. Gligorov, Hamish Gordon, Erik H.M. Heijne, Veerle Heijne, Daniel Hynds, Malcolm John, Alexander Leflat, Lourdes Ferre Llin, Xavi Llopart, Manuel Lozano, Dzmitry Maneuski, Thilo Michel, Michelle Nicol, Matt Needham, Chris Parkes, Giulio Pellegrini, Richard Plackett, Tuomas Poikela, Eduardo Rodrigues, Graeme Stewart, Jianchun Wang,

and Zhou Xing: *Charged particle tracking with the timepix {ASIC}*. Nuclear Instruments and Methods in Physics Research Section A: Accelerators, Spectrometers, Detectors and Associated Equipment, 661(1):31 – 49, 2012, ISSN 0168-9002.

[96] Lawrence S Pinsky and Jeffrey Chancellor: *Development of a new active personal dosimeter for use in space radiation environments*. In *Aerospace Conference, 2007 IEEE*, pages 1–4. IEEE, 2007.

[97] C. Grupen: *Physics of particle detection*. 2009.

[98] M C S Williams: *Particle identification using time of flight*. J. Phys. G: Nucl. Part. Phys., 39(12):123001, Dec 2012, ISSN 1361-6471.

[99] Donald H. Perkins: *Introduction to High Energy Physics (3rd Edition)*. Addison-Wesley, 1987, ISBN 0201121050.

[100] L Pinsky: *A Study of Heavy Trans-Iron Primary Cosmic Rays (Z More than or Equal to 55) with a Fast Film Cerenkov Detector*. PhD thesis, University of Rochester, 1972.

[101] Christian Lippmann: *Particle identification*. Nuclear Instruments and Methods in Physics Research Section A: Accelerators, Spectrometers, Detectors and Associated Equipment, 666:148–172, Feb 2012.

[102] Samuel Ting: *The alpha magnetic spectrometer on the international space station*. Nuclear Physics B - Proceedings Supplements, 243-244(0):12–24, 2013, ISSN 0920-5632.

[103] Frank Hartmann and Jochen Kaminski: *Advances in tracking detectors*. Annual Review of Nuclear and Particle Science, 61:197–221, 2011.

[104] Philippe Gros: *Identifying Charged Hadrons on the Relativistic Rise Using the ALICE TPC at LHC*. PhD thesis, Lund University, 2011.

[105] Peter Križan: *Advances in particle-identification concepts*. Journal of Instrumentation, 4(11):P11017, 2009.

[106] Y. Arai, T. Miyoshi, Y. Unno, T. Tsuboyama, S. Terada, Y. Ikegami, R. Ichimiya, T. Kohriki, K. Tauchi, Y. Ikemoto, Y. Fujita, T. Uchida, K. Hara, H. Miyake, M. Kochiyama, T. Sega, K. Hanagaki, M. Hirose,

J. Uchida, Y. Onuki, Y. Horii, H. Yamamoto, T. Tsuru, H. Matsumoto, S.G. Ryu, R. Takashima, A. Takeda, H. Ikeda, D. Kobayashi, T. Wada, H. Nagata, T. Hatsui, T. Kudo, A. Taketani, T. Kameshima, T. Hirono, M. Yabashi, Y. Furukawa, M. Battaglia, P. Denes, C. Vu, D. Contarato, P. Giubilato, T.S. Kim, M. Ohno, K. Fukuda, I. Kurachi, M. Okihara, N. Kuriyama, and M. Motoyoshi: *Development of {SOI} pixel process technology.* Nuclear Instruments and Methods in Physics Research Section A: Accelerators, Spectrometers, Detectors and Associated Equipment, 636(1, Supplement):S31 – S36, 2011, ISSN 0168-9002.

[107] N. Akchurin, F. Bedeschi, A. Cardini, M. Cascella, D. De Pedis, R. Ferrari, S. Fracchia, S. Franchino, M. Fraternali, G. Gaudio, and et al.: *Particle identification in the longitudinally unsegmented rd52 calorimeter.* Nuclear Instruments and Methods in Physics Research Section A: Accelerators, Spectrometers, Detectors and Associated Equipment, 735:120–129, Jan 2014.

[108] Peter Krizan: *Recent progress in particle identification methods.* Nuclear Instruments and Methods in Physics Research Section A: Accelerators, Spectrometers, Detectors and Associated Equipment, 598(1):130–137, Jan 2009.

[109] D Zhou, E Semones, M Weyland, and S Johnson: *Radiation measured with tepc and cr-39 pntds in low earth orbit.* Advances in Space Research, 40(11):1571–1574, 2007.

[110] Kerry Lee, Joel Flanders, Edward Semones, Tad Shelfer, and Fadi Riman: *Simultaneous observation of the radiation environment inside and outside the iss.* Advances in Space Research, 40(11):1558–1561, 2007.

[111] C. Zeitlin, T. Cleghorn, F. Cucinotta, P. Saganti, V. Andersen, K. Lee, L. Pinsky, W. Atwell, R. Turner, and G. Badhwar: *Overview of the martian radiation environment experiment.* Advances in Space Research, 33(12):2204–2210, Jan 2004, ISSN 0273-1177.

[112] N Stoffle, L Pinsky, M Kroupa, S Hoang, J Idarraga, C Amberboy, R Rios, J Hauss, J Keller, A Bahadori, E Semones, D Turecek, J Jakubek, Z Vykydal, and S Pospisil: *Timepix-based radiation environment monitor measurements aboard the international space station.* In approval process for publication in Nuclear Instruments and Methods A.

[113] D Turecek, L Pinsky, J Jakubek, Z Vykydal, N Stoffle, and S Pospisil: *Small dosimeter based on timepix device for international space station.* Journal of Instrumentation, 6(12):C12037, 2011.

[114] Nicholas Stoffle: *Simulation of van allen belt and galactic cosmic ray ionized particle tracks in a si timepix detector experiments and instrumentation.* In *International Cosmic Ray Conference*, volume 11, page 436, 2011.

[115] A. Ferrari, P. R. Sala, A. Fasso, and J. Ranft: *Fluka: A multi-particle transport code.* In *CERN 2005-10, INFN/TC 05/11, SLAC-R-773*, 2005.

[116] European Space Agency. `http://www.spenvis.oma.be/`.

[117] D Turecek, T Holy, J Jakubek, S Pospisil, and Z Vykydal: *Pixelman: a multi-platform data acquisition and processing software package for medipix2, timepix and medipix3 detectors.* Journal of Instrumentation, 6(01):C01046, 2011.

[118] Rene Brun and Fons Rademakers: *Root - an object oriented data analysis framework.* Nuclear Instruments and Methods in Physics Research Section A: Accelerators, Spectrometers, Detectors and Associated Equipment, 389(1-2):81–86, Apr 1997.

[119] European Organization for Nuclear Research (CERN). `http://root.cern.ch`.

[120] Maarten Ballintijn, Rene Brun, Fons Rademakers, and Gunther Roland: *The proof distributed parallel analysis framework based on root.* In *Computing in High Energy and Nuclear Physics 2003 Conference Proceeding*, 2003.

[121] David Vallado, Paul Crawford, Ricahrd Hujsak, and T.S. Kelso: *Revisiting Spacetrack Report No. 3.* American Institute of Aeronautics and Astronautics, Aug 2006, ISBN 978-1-62410-048-2.

[122] David A. Vallado: *Fundamentals of Astrodynamics and Applications, 4th ed. (Space Technology Library).* Microcosm Press, 2013, ISBN 1881883183.

[123] National Aeronautics and Space Administration (NASA). `http://spaceflight.nasa.gov/`.

[124] T.S. Kelso. `http://celestrak.com/`, 2014.

[125] S Hoang, L Pinsky, R Vilalta, and J Jakubek: *Let estimation of heavy ion particles based on a timepix-based si detector*. Journal of Physics: Conference Series, 396(2):022023, Dec 2012.

[126] R Vilalta, S Kuchibhotla, R Valerio, and L Pinsky: *Development of pattern recognition software for tracks of ionizing radiation in medipix2-based (timepix) pixel detector devices*. In *Journal of Physics: Conference Series*, volume 331, page 032052. IOP Publishing, 2011.

[127] Ricardo Vilalta, Sujeet Kuchibotla, Francisco Ocegueda-Hernandez, Song Hoang, and Larry Pinsky: *Machine learning for identification of sources of ionizing radiation during space missions*. In *International Joint Conference on Artificial Intelligence, Workshop on AI in Space: Intelligence Beyond Planet Earth*, 2011.

[128] Rafael C. Gonzalez and Richard E. Woods: *Digital Image Processing (3rd Edition)*. Prentice Hall, 2007, ISBN 013168728X.

[129] Anil K. Jain: *Fundamentals of Digital Image Processing*. Prentice Hall, 1988, ISBN 0133361659.

[130] M Campbell, V Havranek, E Heijne, T Holy, J Idarraga, J Jakubek, C Lebel, C Leroy, X Llopart, J Novotny, *et al.*: *Charge collection from proton and alpha particle tracks in silicon pixel detector devices*. In *Nuclear Science Symposium Conference Record, 2007. NSS'07. IEEE*, volume 2, pages 1047–1050. IEEE, 2007.

[131] J Bouchami, A Gutierrez, A Houdayer, J Jakubek, C Lebel, C Leroy, J Macana, J P Martin, M Platkevic, S Pospisil, and C Teyssier: *Study of the charge sharing in silicon pixel detector by means of heavy ionizing particles interacting with a medipix2 device*. Nuclear Instruments and Methods in Physics Research Section A: Accelerators, Spectrometers, Detectors and Associated Equipment, 633:S117–S120, 2011.

[132] L Opalka, C Granja, B Hartmann, J Jakubek, O Jaekel, M Martisikova, S Pospisil, and J Solc: *Linear energy transfer and track pattern recognition of secondary radiation generated in hadron therapy beam in a pmma target.* Journal of Instrumentation, 8(02):C02047, Feb 2013.

[133] Richard O. Duda and Peter E. Hart: *Use of the hough transformation to detect lines and curves in pictures.* Communications of the ACM, 15(1):11–15, Jan 1972.

[134] Leandro A.F. Fernandes and Manuel M. Oliveira: *Real-time line detection through an improved hough transform voting scheme.* Pattern Recognition, 41(1):299–314, Jan 2008.

[135] R Beaujean, J Kopp, S Burmeister, F Petersen, and G Reitz: *Dosimetry inside mir station using a silicon detector telescope (dostel).* Radiation Measurements, 35(5):433–438, Oct 2002, ISSN 1350-4487.

[136] Birgit Ritter, Karel Marsalek, Thomas Berger, Sonke Burmeister, Gunther Reitz, and Bernd Heber: *A small active dosimeter for applications in space.* Nuclear Instruments and Methods in Physics Research Section A: Accelerators, Spectrometers, Detectors and Associated Equipment, 748:61–69, Jun 2014, ISSN 0168-9002.

[137] L. Di Fino, M. Casolino, C. De Santis, M. Larosa, C. La Tessa, L. Narici, P. Picozza, and V. Zaconte: *Heavy-ion anisotropy measured by altea in the international space station.* Radiation Research, 176(3):397–406, Sep 2011.

[138] James Ziegler: *Srim software package.*

[139] J Jakubek, C Granja, O Jakel, M Martisikova, and S Pospisil: *Detection and track visualization of primary and secondary radiation in hadron therapy beams with the pixel detector Timepix*, pages 1967–1969. Institute of Electrical and Electronics Engineers, Oct 2010, ISBN 978-1-4244-9106-3.

[140] Carlos Granja, Pavel Krist, David Chvatil, Jaroslav Solc, Stanislav Pospisil, Jan Jakubek, and Lukas Opalka: *Energy loss and online directional track visualization of fast electrons with the pixel detector timepix.* Radiation Measurements, 59:245–261, Dec 2013.

[141] National Institute of Standards and Technology / SEMATECH. `http://www.itl.nist.gov/div898/handbook/`.

[142] International Atomic Energy Agency. `https://www-nds.iaea.org/relnsd/vcharthtml/VChartHTML.html`.

[143] J. Jackson: *Electromagnetic form factor corrections to collisional energy loss of pions and protons, and spin correction for muons.* Phys. Rev. D, 59(1), Nov 1998, ISSN 1089-4918.

[144] X Llopart and T Poikela: *Timepix Manual v1.9.* CERN, March 2014.

[145] Bjarne Stroustrup: *The C++ Programming Language: Special Edition (3rd Edition).* Addison-Wesley Professional, 2000, ISBN 0201700735.

[146] J.D. Sullivan: *Geometric factor and directional response of single and multi-element particle telescopes.* Nuclear Instruments and Methods, 95(1):5 – 11, 1971, ISSN 0029-554X.

[147] Terrance Onsager, Richard Grubb, Joseph Kunches, Lorne Matheson, David Speich, Ron W. Zwickl, and Herb Sauer: *Operational uses of the goes energetic particle detectors.* Society of Photographic Instrumentation Engineers Conference Proceedings: GOES-8 and Beyond, 2812:281–290, Oct 1996.

[148] M Kroupa, J Jakubek, and P Soukup: *Optimization of the spectroscopic response of the timepix detector.* Journal of Instrumentation, 7(02):C02058–C02058, Feb 2012, ISSN 1748-0221.

[149] F. Krejci M. Kroupa, J. Jakubek: *Charge collection characterization with semiconductor pixel detector timepix.* In *IEEE Nuclear Science Symposium Conference Record*, pages 259–262, 2008.

[150] D Turecek and J Jakubek: *Dependence on temperature and pixel threshold of the calibration for the timepix detector and its correction method.* Journal of Instrumentation, 8(01):C01010–C01010, Jan 2013.

[151] Robert E. Simpson: *Introductory Electronics for Scientists and Engineers.* Allyn and Bacon, Inc., 2nd edition, 1987.

Index of authors